JOHANNES GUTENBERG UNIVERSITÄT MAINZ

A combination of petrological and joint chemical-mechanical inversion approaches to unravel deep geodynamic processes

Dissertation zur Erlangung des Grades

DOKTOR DER NATURWISSENSCHAFTEN

im Promotionsfach Geowissenschaften

am Fachbereich Chemie, Pharmazie, Geographie und Geowissenschaften

der Johannes Gutenberg-Universität

Dimitrios Moutzouris

geboren in Athen, Griechenland

Mainz, 2026

Tag der mündlichen Prüfung: 11/06/2026

Thesis Summary

The present thesis demonstrates the significance of integrating petrological data with numerical models that address diffusion processes and the mechanical behavior of key petrogenetic minerals. Specifically, the metamorphic rocks found in the metamorphic sole of the Pindos ophiolite (northwestern Greece) are investigated to elucidate the geodynamic processes responsible for their formation. Metamorphic soles are key petrotectonic units within ophiolite sequences that preserve valuable information on the emplacement of ophiolitic rocks onto continental crust. To gain a deeper understanding on the formation of the Pindos metamorphic sole, the thesis is split into three main chapters (Chapters 2, 3 and 4). Following an introductory chapter, Chapter 2 presents the petrological data acquired from the metamorphic sole rocks. Multiple thermobarometric methods were employed in combination with Ar-Ar and U-Pb geochronology, alongside a detailed petrographic and compositional analysis. These data provided insights into the peak metamorphic conditions experienced by the sole rocks and offer useful constraints on their subsequent cooling and retrograde history. In Chapter 3, the data from Chapter 2 are used to perform inverse diffusion modelling. Forward diffusion models of major elements in garnet and argon in muscovite are applied to quantify key parameters, such as the cooling rate and the initial equilibration temperature, that reproduce the observed data in the Pindos metamorphic sole. The diffusion models are integrated with a Hamiltonian Monte Carlo approach to efficiently explore the parameter space. Since this approach was used in petrological inversion for the first time, Chapter 3 also includes a detailed explanation of the underlying equations and theory of Hamiltonian Monte Carlo method. Using the results of Chapters 2 and 3, Chapter 4 presents the results of a one-dimensional thermomechanical model that simulates the deformational behavior of quartz inclusions in garnet. The (forward) mechanical combined with Hamiltonian Monte Carlo is used to quantify the cooling and decompression rates as well as the initial temperature and pressure conditions responsible for the currently observed residual pressure of quartz in garnet. An important finding of the present thesis is the profound agreement between all inverse methods employed. The combined insights from these approaches indicate that a transient process was responsible for the formation of the Pindos metamorphic sole rocks. In particular, this process is interpreted to be the fast quenching of a small heat source, most probably the quenching of heat producing shear zone. This thesis emphasizes the importance of integrating conventional petrology with both chemical and mechanical modeling to gain insights into the dynamics of metamorphic processes.

Zusammenfassung der Dissertation

Die vorliegende Arbeit verdeutlicht die Bedeutung der Verknüpfung petrologischer Daten mit numerischen Modellen, die Diffusionsprozesse und das mechanische Verhalten wichtiger petrogenetischer Mineralien berücksichtigen. Konkret werden die metamorphen Gesteine der metamorphen Sohle des Pindos-Ophioliths (Nordwestgriechenland) untersucht, um die geodynamischen Prozesse aufzuklären, die für ihre Entstehung verantwortlich sind. Metamorphe Sohlen sind wichtige petrotektonische Einheiten innerhalb von Ophiolithsequenzen, die wertvolle Informationen über die Einlagerung von Ophiolithgestein in die kontinentale Kruste bewahren. Um ein tieferes Verständnis der Entstehung der metamorphen Sohle des Pindos zu erlangen, ist die Arbeit in drei Hauptkapitel unterteilt (Kapitel 2, 3 und 4). Nach einem Einführungskapitel werden in Kapitel 2 die petrologischen Daten vorgestellt, die aus den Gesteinen der metamorphen Sohle gewonnen wurden. Es wurden mehrere thermobarometrische Methoden in Kombination mit Ar-Ar- und U-Pb-Geochronologie sowie eine detaillierte petrographische und kompositorische Analyse eingesetzt. Diese Daten lieferten Einblicke in die maximalen metamorphen Bedingungen, denen die Gesteine der Sohle ausgesetzt waren, und bieten nützliche Anhaltspunkte für ihre anschließende Abkühlung und retrograde Entwicklung. In Kapitel 3 werden die Daten aus Kapitel 2 zur Durchführung einer inversen Diffusionsmodellierung verwendet. Vorwärtsdiffusionsmodelle für Hauptelemente in Granat und Argon in Muskovit werden angewendet, um Schlüsselparameter wie die Abkühlungsrate und die anfängliche Gleichgewichtstemperatur zu quantifizieren, die die beobachteten Daten im metamorphen Sockel des Pindos-Gebirges reproduzieren. Die Diffusionsmodelle werden mit einem Hamilton-Monte-Carlo-Ansatz kombiniert, um den Parameterraum effizient zu untersuchen. Da dieser Ansatz zum ersten Mal in der petrologischen Inversion verwendet wurde, enthält Kapitel 3 auch eine detaillierte Erläuterung der zugrunde liegenden Gleichungen und der Theorie der Hamilton-Monte-Carlo-Methode. Auf der Grundlage der Ergebnisse aus den Kapiteln 2 und 3 werden in Kapitel 4 die Ergebnisse eines eindimensionalen thermomechanischen Modells vorgestellt, das das Verformungsverhalten von Quarz-Einschlüssen in Granat simuliert. Die (Vorwärts-)Mechanik in Kombination mit Hamiltonian-Monte-Carlo wird verwendet, um die Abkühlungs- und Dekompressionsraten sowie die anfänglichen Temperatur- und Druckbedingungen zu quantifizieren, die für den derzeit beobachteten Restdruck von Quarz in Granat verantwortlich sind. Ein wichtiges Ergebnis der vorliegenden Arbeit ist die weitgehende Übereinstimmung zwischen allen angewandten

inversen Methoden. Die kombinierten Erkenntnisse aus diesen Ansätzen deuten darauf hin, dass ein transienter Prozess für die Entstehung der metamorphen Grundgesteine im Pindos-Gebirge verantwortlich war. Konkret wird dieser Prozess als schnelles Abkühlen einer kleinen Wärmequelle interpretiert, höchstwahrscheinlich als Abkühlen einer wärmeerzeugenden Scherzone. Diese Arbeit unterstreicht die Bedeutung der Integration konventioneller Petrologie mit chemischer und mechanischer Modellierung, um Einblicke in die Dynamik metamorpher Prozesse zu gewinnen.

Table of Contents

Chapter 1: Introduction

1.1 Motivation

Rocks represent important carriers of information, recording the combined effects of processes that operate over millions of years. These processes lead to complex Pressure-Temperature-time (P-T-t) paths. Along these paths, the constituent mineral phases of rocks undergo a large number of chemical, mineralogical, and mechanical transformations. Ultimately, rocks sampled at the Earth's surface represent the final products of this complicated history that involves the combined effects of geological and geodynamic processes. Reconstructing and understanding the evolution of such systems using exclusively their final observed state is a challenging task.

In particular, metamorphic rocks are valuable because they provide important insights into deep geodynamic processes that occur during their metamorphic cycle. This cycle begins when the protolith of a metamorphic rock (sedimentary or igneous) is subjected to progressively increasing temperatures and pressures during a prograde metamorphic path (e.g., Winter, 2014). During this path, temperatures increase and thermally-activated physical processes advance at progressively faster rates. This results in the modification or complete loss of earlier geological information formed during the prograde metamorphic stage. At the end of the prograde evolution, rocks may reach peak P-T conditions, where they could remain for a certain period of time and approach equilibrium.

Following peak conditions, metamorphic rocks may begin their retrograde evolution, during which temperatures and pressures progressively decrease (e.g., Bucher & Grapes, 2011). Under these conditions, the rates of thermally-activated processes slow down significantly, thereby promoting the preservation of "frozen" microstructures, chemical signatures and/or mineralogical features. The retrograde evolution of metamorphic rocks can therefore prevent the complete re-equilibration of the system and retain valuable information about the metamorphic and geodynamic history of the rocks.

An important, thermally-activated kinetic process that provides critical information about the retrograde metamorphic path is the diffusion of chemical species within minerals. In the

case of minerals, diffusion is responsible for the intracrystalline transport of matter (e.g., atoms) within the crystal lattice. The rate of chemical diffusion of a particular species in a mineral is described using effective diffusivity parameters (commonly referred to as diffusivities). For most minerals and their corresponding diffusive species, diffusivities strongly depend on temperature and can be expressed based on an Arrhenius relationship. The Arrhenius relationship shows that diffusivities decrease rapidly with decreasing temperature and become negligibly small under low-temperature conditions (e.g., Zhang, 2010). The temperature at which diffusion effectively ceases is commonly referred to as the closure temperature (Dodson, 1973).

Once this temperature is reached, intracrystalline diffusion becomes negligible. This leads to the observation of compositional profiles within minerals that are effectively "frozen", preserving chemical zonation that formed during cooling. These preserved diffusion profiles can be analyzed and compared with numerical diffusion modeling results to understand the rock's thermal history. In particular, such models can be used to constrain parameters such as cooling rates (Burg & Moulas, 2022; Lasaga, 1983; Lasaga et al., 1977) or timescales (e.g., Ague & Baxter, 2007) .

Another thermally activated process that may provide critical information about the retrograde evolution of metamorphic rocks is the viscous creep of mineral hosts enclosing mineral inclusions (Dabrowski et al., 2015). Such host-inclusion systems may develop stress differences due to differences in their thermoelastic properties, such as the thermal expansivity and bulk modulus (e.g., Rosenfeld & Chase, 1961). During cooling and decompression, the host and inclusion respond differently to changing P-T conditions and a difference in pressure also develops between them. However, at increased temperatures, the mineral host may behave in a viscous deformational manner. In the case of minerals, viscous behavior refers to rate-dependent plasticity (creep). In turn, the viscous behavior of the mineral host may lead to the relaxation of the pressure generated in the inclusion (e.g., Zhong et al., 2020). The extent to which this relaxation occurs depends strongly on factors such as temperature, time and the rheological properties of the host mineral. Numerical modeling of viscous relaxation in host-inclusion systems can therefore be used to evaluate whether the originally generated inclusion pressure has been modified. This also allows the exploration of the model parameters and P-T-t paths that could be responsible for producing the (residual) pressures currently observed in mineral inclusions (Zhong et al., 2018, 2020).

The aim of the present thesis is to integrate inverse diffusion modeling and inverse mechanical host-inclusion modeling with primary petrological data to understand the evolution of metamorphic rocks from the Pindos metamorphic sole (northwestern Greece). The diffusion modeling focuses on the diffusion of major elements in garnet and argon diffusion in muscovite, while the mechanical modeling investigates the quartz-in-garnet mechanical system. By combining these approaches with petrological data such as thermobarometric estimates, geochronological measurements and mineral textures, this study seeks to identify the sets of model parameters and P-T-t paths capable of reproducing the chemical and mechanical characteristics of the investigated rocks (Figure 1.1). The integration of these independent approaches provides quantitative constraints on the metamorphic evolution of the rocks and help identify the geodynamic processes responsible for their formation.

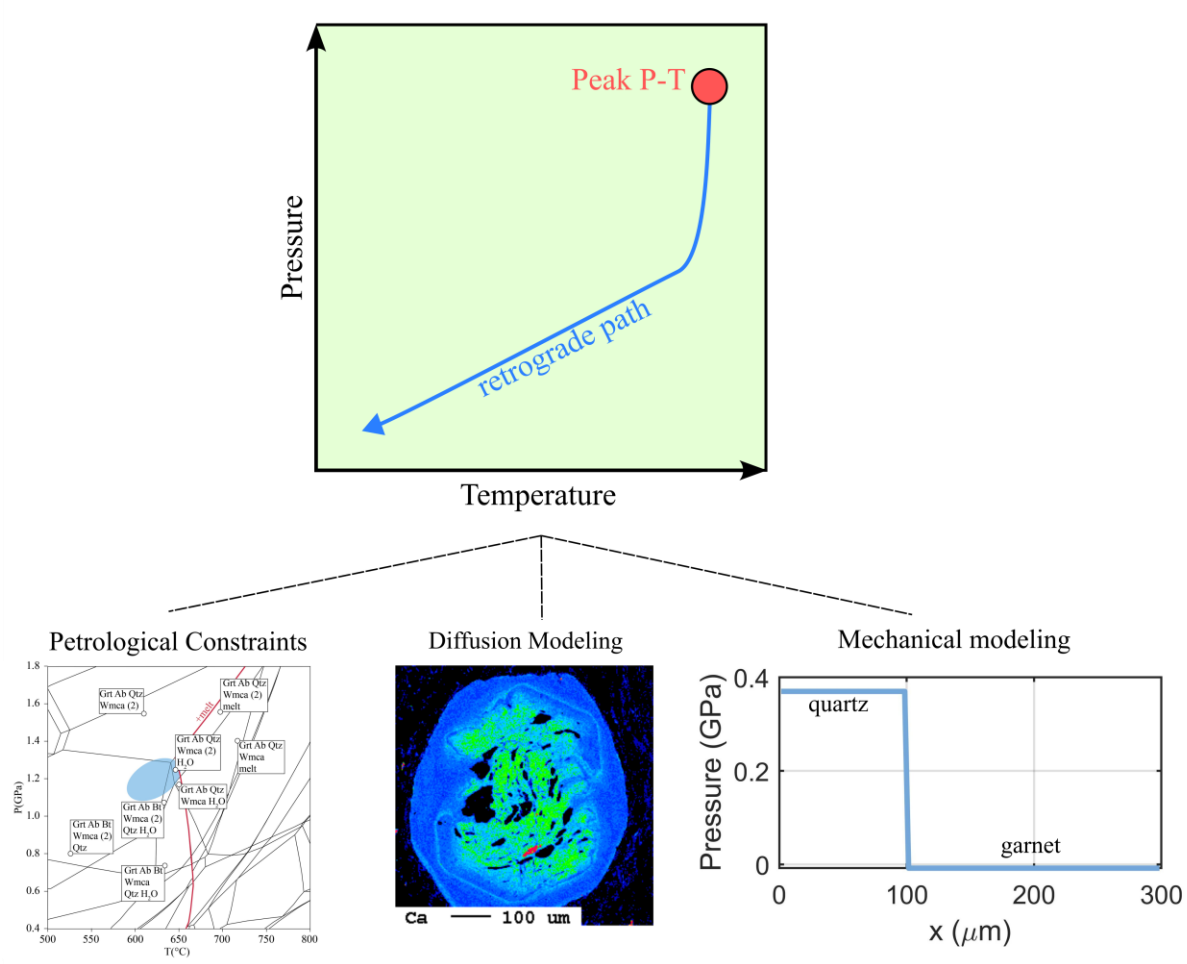

Figure 1.1: Schematic diagram illustrating the main objective of the thesis. The goal is to integrate petrological constraints (geothermobarometry, petrography, kinematic indicators and geochronology) with diffusion and mechanical modeling in order to determine which P-T-t paths can best reproduce the natural data currently observed in the rocks of the Pindos

metamorphic sole. These P-T-t paths can provide important insights into the geodynamic processes involved in the formation of the metamorphic sole rocks.

1.2 Outline of the thesis

The thesis is mainly divided into the following three different chapters:

Chapter 2: Emplacement of the Pindos ophiolite, NW Greece: P-T-t kinematic constraints from the metamorphic sole

This chapter presents the primary petrological data obtained from a mafic amphibolite and a garnet-mica schist from the Pindos metamorphic sole. A petrographic investigation is first conducted to characterize the microstructures and identify the kinematic indicators of the studied rocks. Subsequently, phase equilibria modeling and conventional thermobarometry (Fe-Mg exchange thermometry between garnet and biotite as well as the paragonite-muscovite solvus thermometer) are applied to constrain the near-peak P-T conditions. In addition, quartz-in-garnet barometry is applied to estimate the entrapment conditions of quartz inclusions in garnet. New $^{40}Ar/^{39}Ar$ geochronological data are also presented for muscovite from the garnet-mica schist and amphibole from the amphibolite. Furthermore, U-Pb geochronological data for garnet are reported. The combination of these petrological and geochronological datasets allows the cooling rates experienced by the rocks to be bracketed within a specific range.

Chapter 3: Hamiltonian Monte Carlo applied to inverse petrological problems

This chapter applies a Hamiltonian Monte Carlo inversion approach in combination with diffusion modeling. Diffusion modeling is performed by simulating major-element diffusion in garnet and argon diffusion in muscovite. Specifically, the two numerical models aim to reproduce the compositional profiles observed in garnet as well as the measured $^{40}Ar/^{39}Ar$ age of muscovite. The integration of Hamiltonian Monte Carlo with diffusion modeling allows key parameters (initial equilibration temperature, initial cooling rate and effective grain size of muscovite) to be quantified along with their associated uncertainties. The results of the inversion suggest that the metamorphic sole rocks must have cooled rapidly from a temperature of ~630 °C. This leads to the conclusion that a transient process, such as shear heating, must have played a key role in the formation of the investigated rocks. The results of chapter 3 agree in an independent manner with the petrological findings of chapter 2.

Chapter 4: High cooling rates in metamorphic soles revealed by mechanical inversion of viscoelastic quartz-in-garnet modeling

In this chapter, a one-dimensional thermomechanical model that simulates the viscous relaxation of pressures of quartz inclusions hosted within garnet is presented. The forward model is coupled with Hamiltonian Monte Carlo to constrain key model parameters. These invertible parameters are the initial cooling and decompression rates as well as the initial temperature and pressure conditions. The results of the inversion indicate that high cooling rates are responsible for keeping the quartz-in-garnet system within the elastic deformational regime, thereby inhibiting the viscous relaxation of inclusion pressures. The results of mechanical modeling in this chapter independently agree with the findings of chapters 2 and 3. This confirms the existence of a transient process responsible for the formation of the metamorphic sole. The combined results of chapters 2,3 and 4 are aiming to show the importance of combining diffusion and mechanical modeling along with petrological data to understand the metamorphic evolution of rocks.

1.3 References

Ague, J. J., & Baxter, E. F. (2007). Brief thermal pulses during mountain building recorded by Sr diffusion in apatite and multicomponent diffusion in garnet. *Earth and Planetary Science Letters*, *261*(3–4), 500–516. https://doi.org/10.1016/j.epsl.2007.07.017

Betancourt, M. (2018). *A Conceptual Introduction to Hamiltonian Monte Carlo* (arXiv:1701.02434). arXiv. https://doi.org/10.48550/arXiv.1701.02434

Bower, A. F. (2010). *Applied mechanics of solids*. CRC Press.

Bucher, K., & Grapes, R. (2011). *Petrogenesis of Metamorphic Rocks*. Springer Berlin Heidelberg. https://doi.org/10.1007/978-3-540-74169-5

Burg, J.-P., & Moulas, E. (2022). Cooling-rate constraints from metapelites across two inverted metamorphic sequences of the Alpine-Himalayan belt; evidence for viscous heating. *Journal of Structural Geology*, *156*, 104536. https://doi.org/10.1016/j.jsg.2022.104536

Dabrowski, M., Powell, R., & Podladchikov, Y. (2015). Viscous relaxation of grain-scale pressure variations. *Journal of Metamorphic Geology*, *33*(8), 859–868. https://doi.org/10.1111/jmg.12142

Dodson, M. H. (1973). Closure temperature in cooling geochronological and petrological systems. *Contributions to Mineralogy and Petrology*, *40*(3), 259–274. https://doi.org/10.1007/BF00373790

Dragoni, M., & Magnanensi, C. (1989). Displacement and stress produced by a pressurized, spherical magma chamber, surrounded by a viscoelastic shell. *Physics of the Earth and Planetary Interiors*, *56*(3–4), 316–328. https://doi.org/10.1016/0031-9201(89)90166-0

Duretz, T., Agard, P., Yamato, P., Ducassou, C., Burov, E. B., & Gerya, T. V. (2016). Thermo-mechanical modeling of the obduction process based on the Oman Ophiolite case. *Gondwana Research*, *32*, 1–10. https://doi.org/10.1016/j.gr.2015.02.002

Fjelde, T. E., Xu, K., Widmann, D., Tarek, M., Pfiffer, C., Trapp, M., Axen, S. D., Sun, X., Hauru, M., Yong, P., Tebbutt, W., Ghahramani, Z., & Ge, H. (2025). Turing.jl: A general-purpose probabilistic programming language. *ACM Transactions on Probabilistic Machine Learning*. https://doi.org/10.1145/3711897

Garber, J. M., Rioux, M., Smye, A. J., Cruz-Uribe, A. M., Baker, P. L., Vervoort, J. D., Searle, M. P., & Feineman, M. D. (2025). Shear heating during rapid subduction initiation beneath the Samail Ophiolite. *Nature Geoscience*, *18*, 653–660. https://doi.org/10.1038/s41561-025-01711-6

Hacker, B. R., Mosenfelder, J. L., & Gnos, E. (1996). Rapid emplacement of the Oman ophiolite: Thermal and geochronologic constraints. *Tectonics*, *15*(6), 1230–1247. https://doi.org/10.1029/96TC01973

Hill, R. (1950). *The Mathematical Theory of Plasticity*. (Original work published Oxford University Press)

Ibragimov, I., Kiss, D., & Moulas, E. (2024). A thermo-mechanical model of the thermal evolution and incorporation of metamorphic soles in Tethyan ophiolites: A case study from Oman. *Austrian Journal of Earth Sciences*, *117*(1), 13–24. https://doi.org/10.17738/ajes.2024.0002

Lasaga, A. C. (1983). Geospeedometry: An Extension of Geothermometry. In S. K. Saxena (Ed.), *Kinetics and Equilibrium in Mineral Reactions* (Vol. 3, pp. 81–114). Springer New York. https://doi.org/10.1007/978-1-4612-5587-1_3

Lasaga, A. C., Richardson, S. M., & Holland, H. D. (1977). The Mathematics of Cation Diffusion and Exchange Between Silicate Minerals During Retrograde Metamorphism. In S. K. Saxena, S. Bhattacharji, H. Annersten, & O. Stephansson (Eds.), *Energetics of Geological Processes* (pp. 353–388). Springer Berlin Heidelberg. https://doi.org/10.1007/978-3-642-86574-9_15

Luisier, C., Tajčmanová, L., Yamato, P., & Duretz, T. (2023). Garnet microstructures suggest ultra-fast decompression of ultrahigh-pressure rocks. *Nature Communications*, *14*(1), 6012. https://doi.org/10.1038/s41467-023-41310-w

Moulas, E., Kostopoulos, D., Podladchikov, Y., Chatzitheodoridis, E., Schenker, F. L., Zingerman, K. M., Pomonis, P., & Tajčmanová, L. (2020). Calculating pressure with elastic geobarometry: A comparison of different elastic solutions with application to a calc-silicate gneiss from the Rhodope Metamorphic Province. *Lithos*, *378–379*, 105803. https://doi.org/10.1016/j.lithos.2020.105803

Moutzouris, D., Moulas, E., Kostopoulos, D., Pomonis, P., Beranoaguirre, A., Chatzitheodoridis, E., & Gerdes, A. (2025). Emplacement of the Pindos ophiolite,

NW Greece: P-T-t-kinematic constraints from the metamorphic sole. *Lithos*, *516–517*(108285). https://doi.org/10.1016/j.lithos.2025.108285

Moutzouris, D., Stroh, A., Schorn, S., & Moulas, E. (2026). Hamiltonian Monte Carlo applied to inverse petrological problems. *EarthArXiv*. https://doi.org/10.31223/X58V0H

Neal, R. M. (1996). *Bayesian Learning for Neural Networks*. Springer New York. https://doi.org/10.1007/978-1-4612-0745-0

Neal, R. M. (2011). *MCMC using Hamiltonian dynamics*. https://doi.org/10.1201/b10905

Rosenfeld, J. L., & Chase, A. B. (1961). *Pressure and Temperature of crystallization from elastic effects around sold inclusions in minerals? 259*, 519–541.

Tagliaferri, A., Moulas, E., Schmalholz, S. M., & Schenker, F. L. (2025). Fast and Spatially Heterogeneous Cooling Rates at Amphibolite-Facies Conditions in the Lepontine Alps (Switzerland). *Geochemistry, Geophysics, Geosystems*, *26*(11), e2025GC012410. https://doi.org/10.1029/2025GC012410

Wang, Z., & Ji, S. (1999). Deformation of silicate garnets: Brittle-ductile transition and its geological implications (Pt. 525-541). *The Canadian Mineralogist*, *37*.

Winter, J. D. (2014). *Principles of igneous and metamorphic petrology* (2. ed., Pearson new internat. ed). Pearson Education.

Xu, K., Ge, H., Tebbutt, W., Tarek, M., Trapp, M., & Ghahramani, Z. (2020). AdvancedHMC.jl: A robust, modular and efficient implementation of advanced HMC algorithms. *2nd Symposium on Advances in Approximate Bayesian Inference, Proceedings of Machine Learning Research*, *118*, 1–10.

Zhang, Y. (2010). Diffusion in Minerals and Melts: Theoretical Background. *Reviews in Mineralogy and Geochemistry*, *72*(1), 5–59. https://doi.org/10.2138/rmg.2010.72.2

Zhong, X., Moulas, E., & Tajčmanová, L. (2018). Tiny timekeepers witnessing high-rate exhumation processes. *Scientific Reports*, *8*(1), 2234. https://doi.org/10.1038/s41598-018-20291-7

Zhong, X., Moulas, E., & Tajčmanová, L. (2020). Post-entrapment modification of residual inclusion pressure and its implications for Raman elastic thermobarometry. *Solid Earth*, *11*(1), 223–240. https://doi.org/10.5194/se-11-223-2020

Chapter 2: Emplacement of the Pindos ophiolite, NW Greece: P-T-t-kinematic constraints from the metamorphic sole

This chapter has already been published:

Moutzouris D., Moulas E., Kostopoulos D., Pomonis P., Beranoaguirre A., Chatzitheodoridis E., Gerdes A. (2025). Emplacement of the Pindos ophiolite, NW Greece: P-T-t-kinematic constraints from the metamorphic sole. Lithos, 516-517, 108285, https://doi.org/10.1016/j.lithos.2025.108285

Author contribution

The author of this dissertation prepared the original manuscript and performed the calculations involving phase-equilibria modeling, geothermometry and elastic barometry. In addition, the author conducted the Raman analyses, processed and evaluated the data and interpreted the results. Finally, the author of the dissertation contributed in the development of the research ideas, prepared the figures as well as conducted the literature review.

Abstract

Metamorphic soles are key petrotectonic units that offer valuable insights into the processes governing ophiolite emplacement on continental margins (obduction). In this work, we have investigated the metamorphic sole of the Pindos ophiolite in northwestern Greece. In the studied locality, the sole is sandwiched between mantle peridotites and pillow lavas of N-MORB affinity. Our study focuses on two lithologies from the metamorphic sole: a garnet-mica schist (metapelite) and a mafic amphibolite. Kinematic indicators from the garnet-mica schists are consistent with top-to-the-NE shearing of the Pindos ophiolite on the Pelagonian zone. Petrographic and textural evidence, geothermometry results (Fe-Mg garnet-biotite exchange and paragonite-muscovite solvus thermometry), and phase-equilibria modelling bracket the upper-limit of metamorphism at amphibolite-facies conditions (630±20°C and 1.1±0.2GPa). Moreover, Quartz-in-Garnet (QuiG) barometry yields a pressure of ~1.2GPa for 630°C demonstrating the equilibration of garnet inclusions at high-pressure conditions. New $^{40}Ar/^{39}Ar$ dating results from syn-kinematic muscovite from the metapelite and amphibole from the amphibolite indicate an apparent minimum age of 164.16±0.37Ma and a consistent age plateau at 165.5±0.73Ma respectively. Notably, the amphibole exhibits no evidence of argon loss. The muscovite age, by contrast, should be considered a minimum apparent age due to the potential influence of argon diffusion. Finally, U-Pb geochronology of garnet was dominated by inclusions and did not result in a meaningful age. The measured ages imply cooling rates for the Pindos metamorphic sole ranging from 60 to 625°C/Ma.

2.1 Introduction

The obduction of ophiolites onto continental crust and the formation of metamorphic soles at the base of ophiolite sequences have been subjects of ongoing research for many years. Obduction is recognized as a complex thermomechanical phenomenon requiring the emplacement of large and dense segments of oceanic lithosphere onto continental crust (e.g., Dewey, 1976). Numerous theories have been proposed since, with most theories invoking an intra-oceanic subduction system as the emplacement mechanism of ophiolitic sequences onto continental margins (Hacker et al., 1996; Robertson, 2004). Others attribute the initiation of intra-oceanic subduction and later emplacement of an ophiolite to the collapse of a mid-ocean ridge (e.g., Boudier et al., 1985).

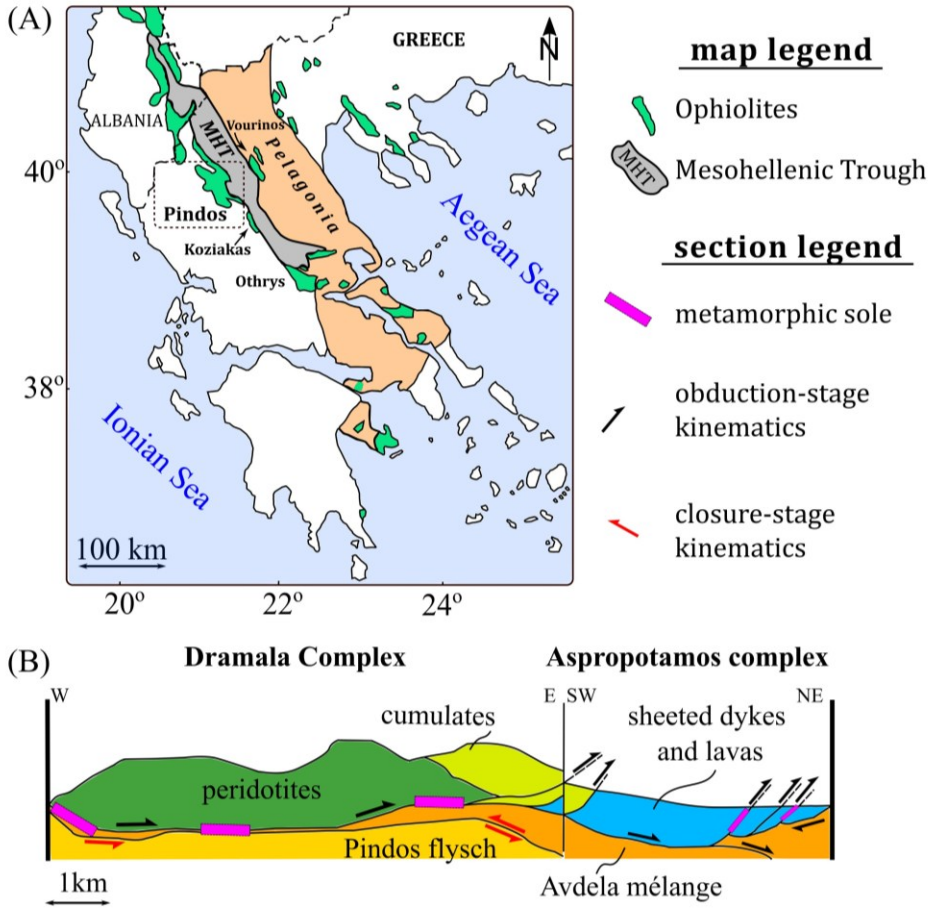

Figure 2.1: Regional geology of the Pindos ophiolite. (A) Distribution of the main ophiolitic complexes in mainland Greece and Albania. Data compilation from Gartzos et al. (2009), Robertson et al. (1991), Smith et al. (1979), Smith (1993) and Smith and Spray (1984). The Pindos ophiolite is highlighted in the dashed quadrangle. (B) Simplified geological section for the Pindos ophiolite. The section has been simplified and modified after Rassios and Moores (2006) and Sergeev et al. (2014).

Regardless of the geodynamic setting, the obduction of an ophiolite sequence on the continental margin is commonly documented by the presence of high-grade metamorphic rocks, also referred to as metamorphic soles, that are characterized by mixed (oceanic and continental) affinities (e.g., Agard et al., 2016 and references therein). Metamorphic soles represent slivers of metamorphic rocks found beneath the basal mantle peridotites of ophiolitic complexes. They exhibit a range of metamorphic grades, spanning from greenschist- to amphibolite- and granulite-facies conditions. Notably, these rocks display an inverse metamorphic gradient. The metamorphic grade can reach granulite-facies conditions close to the contact with the overlying peridotites (e.g., Myhill, 2011). The formation of metamorphic soles has in general been associated with an intra-oceanic thrusting system (e.g., Williams and Smyth, 1973) but the mechanics and the timescales of this process are generally poorly constrained.

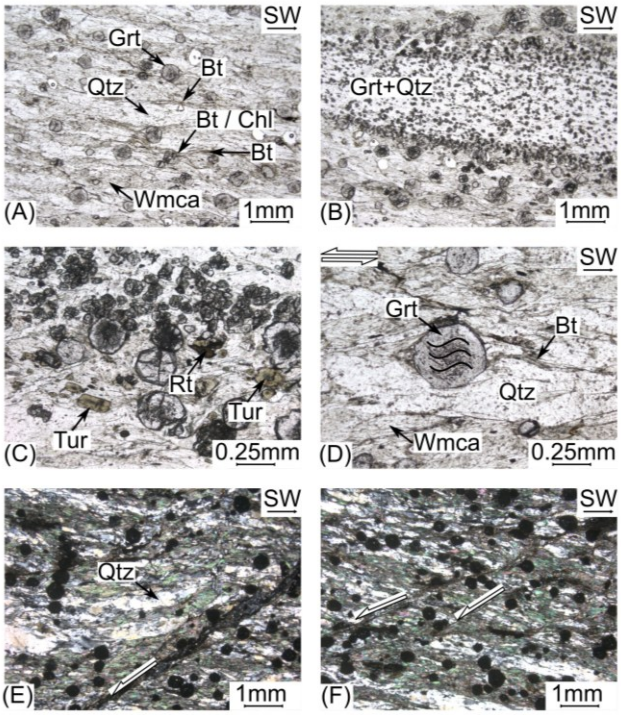

Figure 2.2: Photomicrographs of the garnet-mica schist from the Pindos sole displaying the most important textures observed. Mineral abbreviations after Siivola and Schmid (2007). (A) White mica (undifferentiated) and garnet porphyroblasts in the rock's matrix. (B) Millimetric band composed entirely of minute garnet and quartz. (C) Detail from (B) focusing on the contact between the thin quartz-garnet band and the matrix. (D) Syn-kinematic garnet porphyroblast showing apparent top-to-the-NE rotation. (E) Asymmetric quartz ribbons and S-

C shear bands indicating top-to-the-NE shearing (crossed polars). (F) S-C shear bands indicating top-to-the-NE shearing (crossed polars).

To gain a deeper understanding of the pressure (*P*), temperature (*T*) and time (*t*) constraints of ophiolite obduction, we examined the Pindos metamorphic sole in northwestern Greece (Figure 2.1A). Our study focused on the metamorphic conditions experienced by a metapelitic lithology within the sole. We provide thermobarometric and phase equilibria evidence of syn-kinematic recrystallization at upper amphibolite-facies metamorphism. Kinematic indicators from the sole metapelites point to a top-to-the NE sense of shearing. We obtained new $^{40}Ar/^{39}Ar$ apparent ages for metamorphic magnesio-hornblende from a sole amphibolite and syn-kinematic muscovite from the sole metapelite indicating that the metamorphic sole formed in middle Jurassic times. Moreover, we attempted to date garnet using U-Pb geochronology, but the presence of multiple zircon inclusions prevented us from obtaining a reliable growth age. The close correlation of our $^{40}Ar/^{39}Ar$ ages with the crystallization age of ophiolitic gabbros from Pindos (Liati et al., 2004) indicates tectono-metamorphic processes occurring within a specific time frame. Finally, the cooling ages of muscovite and amphibole suggest that the peak metamorphic conditions were followed by rapid cooling, indicative of fast transient processes during ophiolite emplacement.

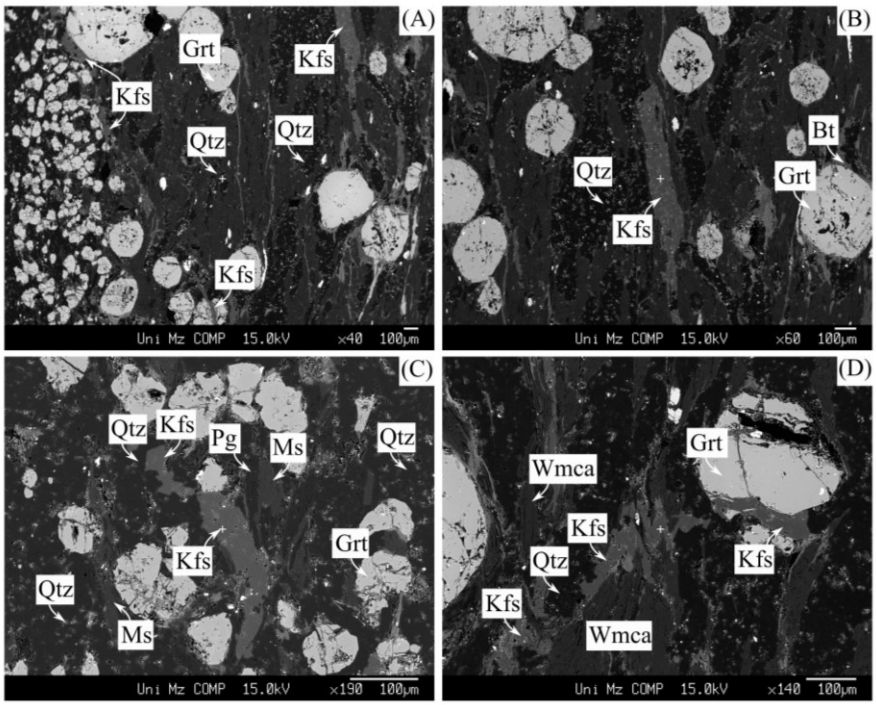

Figure 2.3: Back-Scattered Electron images of the main textures observed. (A) The contact between the rock matrix (left) and the thin, quartz-rich band (right). (B) K-feldspar observed

in a region rich in quartz and garnet. (C) Garnet porphyroclasts in a matrix of white mica (muscovite and paragonite) and quartz. Note the large K-feldspar lath in the center of the image. (D) K-feldspar occurring both at the rims of a white mica lath (undifferentiated) and in garnet cracks.

2.2 Regional geology

Upper Palaeozoic plate reconstructions (e.g., Stampfli et al., 2013) show the northward subduction of the Palaeotethys oceanic tract beneath Laurasia (350–280Ma), the southernmost margin of which was composed, among other blocks, of Adria, the Hellenides and Anatolia. Late Carboniferous magmatism in the Greek area is related to granitoid emplacement between 320 and 280Ma (Anders et al., 2007 and references therein) and formation of the Pelagonian cordillera. This is the backbone of Greece stretching from the border with Albania in the northwest to the Cycladic archipelago in the southeast (Figure 2.1A). Subsequent roll-back of the Palaeotethyan slab triggered the collapse of most of the European Variscan orogen. In the Triassic, extension in the upper plate led to the opening of oceanic marginal basins, younging southwards (Scythian to Anisian in the Meliata and Küre basins, Ladinian in the Maliac basin and Carnian in the Pindos basin; Stampfli et al., 2013). In the Pindos mountains of Greece, Upper Triassic E- and N-MORB-type lavas record the opening of the Pindos Ocean (Kostopoulos, 1989) to the west of Pelagonia (Figure 2.1A).

The Pindos ophiolite, is Jurassic in age (ca. 171Ma) based on SHRIMP U-Pb zircon crystallization ages of gabbros (Liati et al., 2004). It comprises two individual suites, one showing mid-ocean ridge, island-arc tholeiitic and boninitic affinities, the other being purely boninitic (Kostopoulos, 1989). These two suites have been interpreted as having been generated at a ridge-trench-transform intersection and a subduction forearc respectively (Kostopoulos, 1989). The Pindos ophiolite is separated from the Vourinos ophiolite to the east by the submarine siliciclastic deposits of the Mesohellenic Trough, a large, elongate (300x30x4.5km) orogenic basin trending NW-SE, from northern Albania to central Greece, that operated from the Upper Eocene (ca. 45Ma) to the Middle Miocene (ca. 15Ma; Ferrière et al., 2013) (Figure 2.1A). The two massifs are likely connected as part of a large mafic-ultramafic oceanic slab beneath the Mesohellenic Trough as evidenced by the presence of a massive positive magnetic anomaly corresponding to an ultramafic “keel” deep beneath the sedimentary strata (Rassios et al., 2009; Rassios and Dilek, 2009).

Metamorphic-sole rocks include metasediments and metabasites that occur as thin (less than 200m), sheet-like bodies structurally below serpentinised mantle peridotite (Figure 2.1B; after Rassios and Moores, 2006). According to Kemp and McCaig (1984) and Kostopoulos (1989 and references therein), the lower part of the sole comprises greenschist-facies metabasites, calcareous schists, graphitic schists, marbles, micaceous quartzites and garnet-mica schists while the upper part predominantly contains banded amphibole schists, epidote-amphibolite, and garnet amphibolite. These rocks are thought to represent a metamorphic aureole formed during the initial "displacement" of the ophiolite in the oceanic regime (Jones and Robertson, 1991; Spray, 1984). Hornblende separates from the amphibolites have yielded respective $^{40}Ar/^{39}Ar$ ages of 169Ma (Spray et al., 1984).

2.3 Samples and Methods

The present study focuses on the metamorphic conditions of a metapelite sample from the metamorphic sole of the Pindos ophiolite (Liagouna locality: 39°59'18.6", 21°11'14.8" discussed in Kostopoulos, 1989). Additionally, an amphibolite sample was investigated from the same locality. Both metapelitic and amphibolitic samples were taken approximately 100m away from the contact with the peridotites. Ten (10) thin sections from the same metapelitic sample and three (3) thin section from the amphibolite were thoroughly examined by means of transmitted-light microscopy (plane- and cross-polarized light), Electron Probe Micro Analysis (EPMA) and Scanning Electron Microscopy (SEM). All metapelitic thin sections showed identical features. Particular care was taken to collect orientated samples in the field and four of the studied thin sections were carefully cut parallel to the lineation and perpendicular to the foliation to provide details on the kinematics of ductile structures. S-C shear bands, fabric asymmetry and spiral inclusions in garnet were used as kinematic indicators. EPMA analyses were conducted at the Institute of Geosciences, Johannes Gutenberg University, Mainz, Germany. Further details on the equipment used and operating conditions can be found in Burg and Moulas (2022; their supplementary material). The amphibolite was measured at the Institute of Geosciences of the Goethe University of Frankfurt with a JEOL 8530F Plus Hyperprobe that comprises 5 wavelength-dispersive spectrometers. An accelerating voltage of 15.0 kV and a beam current of 20 nA were used. Synthetic and natural standards were utilized for the calibration of the machine. The beam diameter was set to either 1 or 2 μm. The peak measurement time was set to 20.0 seconds and the PRZ ARMSTRONG correction was applied.

$^{40}Ar/^{39}Ar$ geochronological analyses on mineral separates were carried out for the metapelite and amphibolite lithologies of the metamorphic sole. Specifically, a magnesio-hornblende

separate from the amphibolite and a syn-kinematic muscovite from the metapelite were investigated. The measurements were carried out at Oregon State University using an incremental, bulk-laser heating technique. To derive representative mineral ages, we relied on consistent apparent age measurements observed across incremental heating steps. The released ^{39}Ar was monitored and we focused on data points where age values remained stable (age plateau) over increasing cumulative amounts of ^{39}Ar. A detailed description of the analytical procedure is provided in the supplementary material, and all measurement data are documented in the accompanying supplementary spreadsheet.

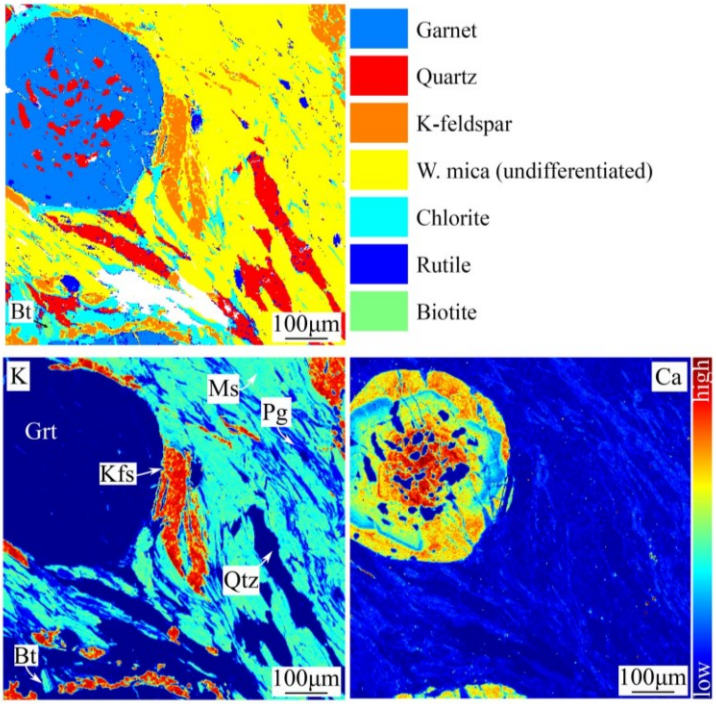

Figure 2.4: (Top) Mineral map constructed using individual elemental distributions. (Bottom) K and Ca distribution maps.

Uranium-lead (U-Pb) dating was conducted at the Frankfurt Isotope and Element Research Center (FIERCE) at the Goethe University of Frankfurt (Germany) using a Thermo-Scientific Neptune Plus Multi-Collector Laser Ablation Inductively–Coupled Plasma–Mass Spectrometer (MC LA-ICP-MS). In situ measurements were acquired using a RESOlution 193nm ArF Excimer laser. More details on the analytical techniques and acquired measurements can be found in the supplementary material and provided spreadsheet.

To constrain the pressure and temperature (*P-T*) conditions of the metapelite, we performed phase-equilibria modelling using the PERPLE_X software package (Connolly, 2009). An effective bulk composition (EBC) for the metapelite was used in which only the outer 5% of

garnet was considered. Exact details on the determination of the EBC can be found in the supplementary material. The total bulk composition of the metapelite was also used for comparison (Table S. 2.1). We carried out two different series of calculations. In the first one, we have utilized the KNCFMASH (K_2O-Na_2O-CaO-FeO-MgO-Al_2O_3-SiO_2-H_2O) model system and the thermodynamic dataset of Holland and Powell (1998, with updates) as given in PERPLE_X. In this system, we have simplified the bulk composition by leaving out TiO_2 and MnO because of the limited number of experiments performed to calibrate the respective solid solution models. The second set of calculations was performed in the KNCFMASH + Mn (K_2O-Na_2O-CaO-FeO-MgO-Al_2O_3-SiO_2-H_2O-MnO) model system using the more recent thermodynamic database of Holland and Powell (2011) as in Green et al. (2016) (hp62ver). In this instance, MnO was included because the corresponding solid-solution models for garnet, biotite and chlorite were calibrated by considering Mn. Details on the solid solution models and the relevant H_2O equations of state used in each case can be found in the supplementary material.

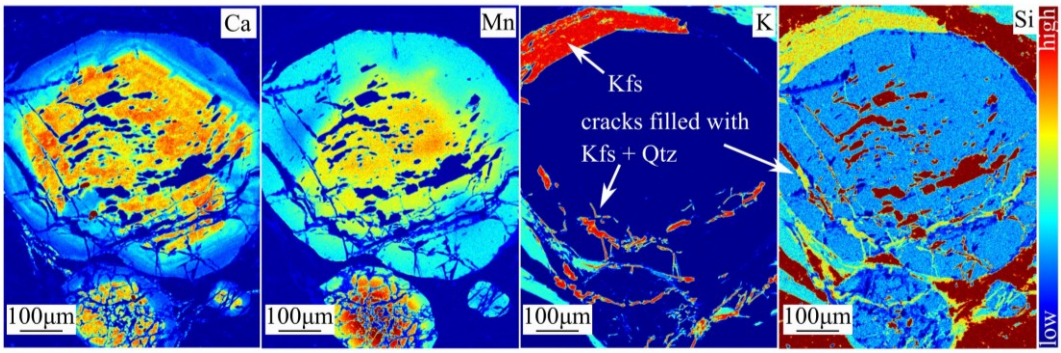

Figure 2.5: Ca, Mn, K, and Si distribution maps of a large garnet porphyroblast. Note the cracks filled with K-feldspar and quartz.

In both cases, we have produced isochemical, pressure-temperature phase-diagram sections (*P*-*T* sections) either in water-saturated conditions or with a fixed amount of water. Moreover, isobaric temperature-composition (*T*-*X*) sections were modelled. These were supplemented by conventional geothermometry using adjacent garnet-biotite (Hodges and Spear, 1982; Kaneko and Miyano, 2004; Kleemann and Reinhardt, 1994), muscovite-paragonite compositional pairs (Blencoe et al., 1994; Coggon and Holland, 2002), adjacent garnet-muscovite pairs (Wu and Zhao, 2006) and garnet-phengite (Green and Hellman, 1982).

Finally, we applied elastic barometry where we used Raman spectroscopic analyses on quartz inclusions from metapelite garnets. The quartz spectra were obtained at the National Technical

University of Athens (Greece), utilizing a Renishaw Ramascope RM1000 Raman spectrometer coupled with a Leica DM LM optical microscope. A natural, strain-free quartz crystal was employed as a reference standard to capture the reference 206 and 464 cm^{-1} peaks of quartz. A total number of 35 quartz inclusions in garnet were analyzed. We mostly focused on spherical quartz inclusions away from fractures or other inclusions to avoid geometric complexities and non-elastic contributions (for corresponding references see supplementary material). We additionally avoided cracks or features that could possibly relax stresses. The final spectra were fit with a Lorentzian curve using MATLAB® to accurately capture the shifted positions of the 206 and 464 cm^{-1} vibrational modes of quartz. Further methodological details and analytical parameters are provided in the supplementary material.

2.4 Results

2.4.1 Petrography

The metapelites (sample VK24) display a clear foliation defined by white mica (undifferentiated), quartz, and K-feldspar ribbons (Figure 2.2A); minor biotite can also be found along the foliation planes. Garnet occurs as porphyroblasts (half a mm in diameter) in the matrix (Figure 2.2). Small bands composed entirely of quartz and minute garnets (<0.1 mm in diameter) occur locally (Figure 2.2B). At the rims of these small bands, the two garnet sizes can be seen together along with rutile and tourmaline (Figure 2.2C). K-feldspar is observed both in the matrix and at the rims of the quartz-rich bands (Figure 2.3). In many cases, K-feldspar is observed crystallizing at the rims of garnet (Figure 2.4) or within cracks cutting garnet (Figure 2.3D and Figure 2.5). The K-feldspar forming inside these cracks is often found together with quartz (K and Si map in Figure 2.5). White mica is composed of muscovite-rich and paragonite-rich laths which become visible in a K map (Figure 2.4 and Figure 2.6). In one case, K-feldspar was found developing at the rim of a large, white mica lath (Figure 2.3D). Other phases found in smaller amounts in the matrix are plagioclase (albite-rich) and chlorite. The plagioclase is often concentrated in small domains together with quartz and K-feldspar (Figure 2.6) whereas chlorite replaces biotite at the rims of garnet (Figure 2.4). Titanium-bearing accessory phases are also present. Manganoan-ilmenite occurs as inclusions in garnet while rutile is widespread in the matrix (Figure 2.2C).

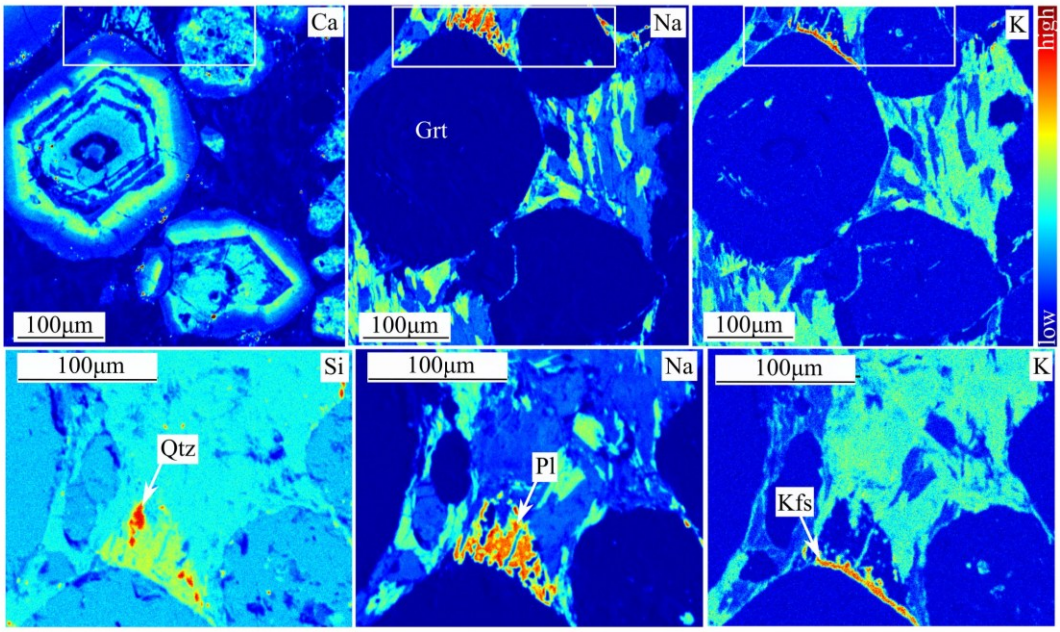

Figure 2.6: Ca, Na, K (top row) and Si, Na, K (bottom row) maps from a region rich in garnet porphyroblasts. The white rectangle marks the area with quartz-plagioclase-K-feldspar intergrowths (details in bottom row).

Kinematic indicators from quartz inclusion trails indicate the syn-kinematic growth of garnet (Figure 2.2D). In the majority of garnet porphyroblasts, the spiral-shape of quartz inclusions indicate a top-to-the NE shear of the garnet with respect to its surrounding matrix. However, some garnet porphyroblasts have been observed to have the opposite sense of shear. Nevertheless, in all of the investigated oriented thin sections, the asymmetric quartz ribbons and S-C bands in mica undoubtedly indicate a top-to-the-NE sense of shear (Figure 2.2E-F).

The amphibolite (sample VK25) is equigranular in texture and exhibits a distinct foliation defined by green amphibole. The amphibole appears primarily as idiomorphic crystals ranging from 0.3 to 0.8 mm in diameter, though occasional larger crystals exceeding 2 mm are also present (Figure S. 2.1A, B). Amphibole constitutes a dominant 65-70 vol% of the rock. Titanite was found as an inclusion in amphibole. The remaining matrix is comprised of a very fine-grained intergrowth. The intergrowth has fully replaced plagioclase and is mostly comprised of fine-grained muscovite (sericite) and possibly epidote or prehnite (Figure S. 2.1C, D; supplementary material).

2.4.2 Mineral and bulk rock chemistry

The studied metapelitic sample shows a sedimentary affinity based on a Zr/Ti vs Ni classification and plots at the low-Al field of common metapelites in an AFM diagram

(projected from muscovite and corrected for paragonite) (Figure S. 2.2; supplementary material). Representative mineral analyses are given in Table 2.1. In general, most minerals show a uniform composition except for garnet porphyroblasts that show a prominent zonation in Ca (Figure 2.4Figure 2.6). Matrix garnet falls in the range: $Prp_{13\text{-}22}Alm_{72\text{-}78}Grs_{0.02\text{-}0.08}Sps_{0.02\text{-}0.06}$. Their grossular and spessartine components decrease and X_{Mg} (i.e., $Mg/[Mg+Fe]$; molar ratios) increases from core to rim. A representative X_{Mg} value at the garnet rim is 0.2±0.02. The smaller garnets of the quartz-rich band (e.g., Figure 2.2B) are richer in MnO and characterized by the composition: $Prp_{16\text{-}17}Alm_{57\text{-}58}Grs_{0.11\text{-}0.13}Sps_{0.14}$. The few ilmenite inclusions in garnet are manganoan containing ca. 27% pyrophanitic component $(Fe_{0.73}Mn_{0.27})TiO_3$.

Biotite shows a uniform composition with X_{Mg} stretching between 0.57 and 0.60. Chlorite replacing biotite shows X_{Mg} values from 0.47 to 0.53 with an average of 0.51. White mica has a variable X_{Mg} content depending on whether it is muscovite- or paragonite-rich. Muscovite-rich white mica has an average X_{Mg} of 0.61 whereas paragonite-rich white mica has an X_{Mg} between 0.25 and 0.56 with an average of 0.41. The plagioclase found in association with K-feldspar and quartz (Figure 2.6) is sodic with X_{Ab} (i.e., $Na/[Na+Ca]$; molar) ranging from 0.82 to 0.94. K-feldspar maintains the same composition across all textures, with a $K/[K+Na+Ca]$ molar ratio ranging from 0.97 to 0.99.

The representative chemical composition of amphibole from the amphibolite is also shown in Table 2.1. We used the Excel spreadsheet of Locock (2014), which follows the latest nomenclature for the amphibole supergroup (Hawthorne et al., 2012), to calculate the chemical formula of amphibole. Assuming total iron is ferrous, the amphibole can be classified as a magnesio-hornblende. Including ferric iron, the nomenclature predicts a $Fe^{+3}/\Sigma Fe$ ratio of ~0.088 and the classification of the amphibole is not affected. The composition of amphibole is uniform from grain to grain but also from core to rim. The ranges of Mg, Fe and Ca are 3.32-3.56, 0.58-0.72 and 1.91-1.98 a.p.f.u., respectively. The intergrowth that replaces plagioclase comprises two mineral phases. The most abundant phase (~85 vol.%) is a fine-grained muscovite (sericite) which has a K/(K+Na) ratio of 0.98. The remaining intergrowth consists of a fine-grained hydrous phase primarily composed of Si, Ca, and Al. This phase was highly susceptible to beam damage which prevented accurate measurements and resulted in unsatisfactory oxide totals. However, this phase could be identified as either epidote or prehnite.

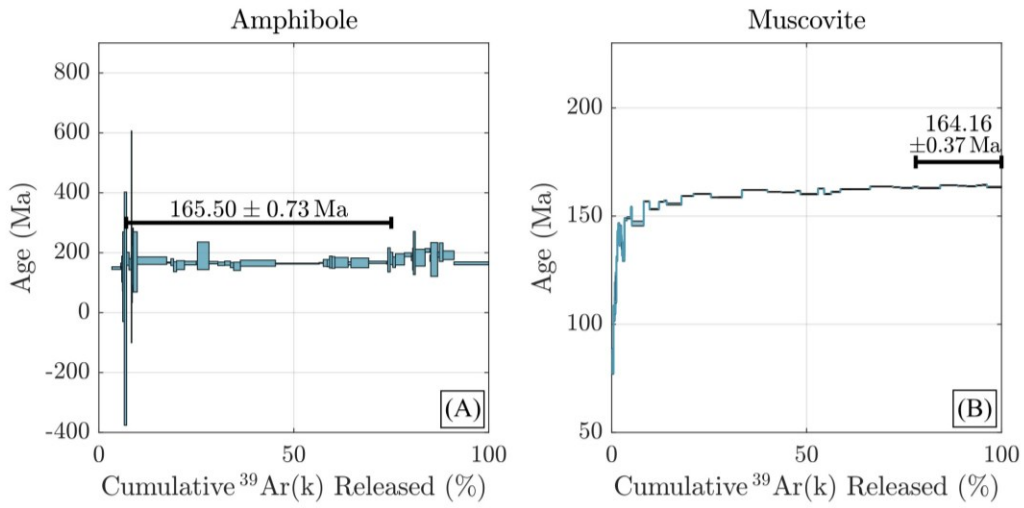

Figure 2.7: Ar-Ar age spectrum plots for amphibole (A) and syn-kinematic muscovite (B) separates from the Pindos ophiolitic sole. Amphibole shows a well-defined age plateau at 165.5±0.73 Ma (2σ). Muscovite exhibits Ar loss but shows an age plateau of 164.16±0.16 Ma (2σ). See main text for more details.

2.4.3 Ar-Ar geochronology

The results of the $^{40}Ar/^{39}Ar$ geochronology are presented in Figure 2.7. Apparent ages are plotted against the cumulative ^{39}Ar released per heating step (age spectrum plot). Final ages were determined by identifying age plateaus. For the amphibole, several initial measurements showed large 2σ errors. However, a distinct and well-defined age plateau yields a Jurassic age of 165.5±0.73 Ma (2σ). The preservation of the age-plateau indicates that there was no loss of Ar and that amphibole was unaffected by diffusion or secondary processes. Conversely, the syn-kinematic muscovite is defined by insignificant analytical errors. However, initial heating steps have shown notable amounts of Ar loss. Progressive incremental heating led to a rapid increase of the apparent age as shown from the age plateau defined by the last heating steps. This pattern could be related to volume diffusion of Ar (e.g., Wijbrans and McDougall, 1988) or alteration processes. During the final incremental heating steps (from ~78 % of ^{39}Ar released), a minimum age plateau was observed, defining an age of 164.16±0.37 Ma (2σ). Notably, the radiogenic Ar compositions at the rim of muscovite during the initial steps yielded a Cretaceous age of approximately 78 Ma (Figure 2.7B).

2.4.4 U-Pb geochronology

The results of U-Pb geochronology of garnets from the metapelite of the Pindos metamorphic sole are presented in a Tera-Wasserburg plot as seen in Figure 2.8. The analytical results are also given in detail in the supplementary material. Generally, U, Th, and Pb content show a

large variability, with concentrations up to 10 µg/g of U or 159 µg/g of Th. The amount of radiogenic and common Pb is also variable. This variability allows the determination of a regression line that intersects the concordia curve at 178.5±4.8 Ma (2σ). However, upon careful examination of the time-resolved analyses, it is most likely that the elevated concentrations of U and Th are attributable to the presence of inclusions, specifically zircon and/or rutile in the case of high U and monazite in the case of high Th contents.

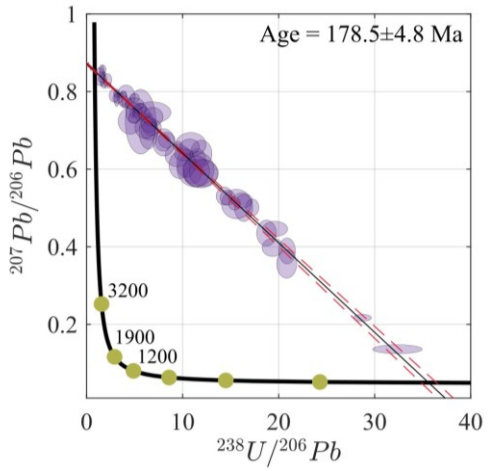

Figure 2.8: Tera-Wasserburg plot illustrating the U-Pb isochron for garnets from the studied metapelite. The regression yielded an age of 178.5 ± 4.8 Ma.

2.4.5 Phase-equilibria and thermobarometric estimations

The estimation of the peak metamorphic conditions attained by the metapelite was based on i) petrographical evidence, ii) phase-equilibria modelling and iii) mineral thermobarometry. The assemblage garnet-biotite-muscovite-paragonite-plagioclase-quartz (GBMPPQ) in metapelites is indicative of high-grade (T>600°C and P~1GPa) conditions (Tinkham et al., 2001, p. 12). Chlorite is observed to replace biotite and therefore is not considered as part of the peak-*T* assemblage. The GBMPPQ assemblage, however, does not explain the presence of large crystals of syn-kinematic K-feldspar in the rock (Figure 2.4). To investigate the stability of K-feldspar, we used isochemical phase diagrams under two different sets of conditions and using two different thermodynamic datasets (Holland and Powell, 1998; Holland and Powell, 2011). With both datasets we first examined water-saturated conditions. Subsequently, to simulate water-undersaturated conditions, we introduced a fixed amount of water (3.17 wt.%) in order to stabilize hydrous minerals while maintaining a controlled level of water undersaturation. The Effective Bulk Composition (EBC) was determined using mineral modal abundances of the rock matrix as depicted in Figure 2.4 and their compositions. For garnet,

only the outer (last 5% of garnet radius) rim composition was used whereas its core composition was not considered in the determination of the EBC (see supplementary material for details).

Regardless of the water-content and across both datasets, we found no stability field in which K-feldspar coexisted with the GBMPPQ assemblage (Figure 2.9 and Figure S. 2.3 of the supplementary material). Notably, in water-saturated conditions the coexistence of any kind of feldspar along with muscovite and paragonite is unfavorable (Figure 2.9A and Figure S. 2.3A of the supplementary material). Meanwhile, under water-undersaturated conditions, albite or albite-rich plagioclase became stable (Figure 2.9B and Figure S. 2.3B of the supplementary material). Considering this observation, we further explored the role of H_2O in the stability of feldspar. Therefore, we constructed *T-X* sections at constant pressure (1.1GPa). In these sections, H_2O (*X*) varies from 2.19 to 4.13 (wt.%). Figure 2.9C and Figure S. 2.3C illustrate that K-feldspar can become stable within a narrow range of water content, from 2.19 to 2.4 wt.%. However, kyanite and a single white mica phase are also stable in this field alongside K-feldspar. This assemblage does not correspond to the one observed in the studied rock. K-feldspar can also be present along with kyanite at temperatures exceeding 775 °C. Evidently, the equilibrium approach followed here is not enough to explain the presence of K-feldspar. Therefore, different scenarios for the formation of K-feldspar have been considered (see discussion).

Table 2.1: Representative mineral compositions (wt.%). Amph12 is a representative magnesio-hornblende from the amphibolite. Mineral abbreviations after Siivola and Schmid (2007). Norm [O] indicates the number of oxygen atoms used in the recalculation of the atoms per formula unit (a.p.f.u.).

Comment	E12	L2_91	E1	E3	E7	E8	E10	L19_134	L59_174	Can17	Can16	S4_D02	An8	S3_D15	Amph12	Ser1
Abbr.	**Kfs**	**Kfs**	**Pl**	**Pl**	**Wmca**	**Wmca**	**Grt**	**Grt**	**Grt**	**Grt**	**Bt**	**Bt**	**Chl**	**Chl**	**Hbl**	**Ser**
SiO_2	62.53	64.82	65.92	64.41	46.41	46.36	38.21	37.96	38.14	38.52	36.60	36.00	29.12	29.82	47.24	45.98
TiO_2	0.02	0.01	0.04	0.02	0.27	0.53	0.17	0.12	0.02	0.03	1.32	0.84	0.10	0.07	0.23	0.01
Al_2O_3	17.94	18.25	20.49	21.67	38.05	35.48	21.09	21.40	22.04	21.42	18.86	20.00	18.93	18.00	12.19	36.01
FeO	2.28	0.55	0.52	0.36	0.74	0.95	30.67	31.10	33.81	33.51	16.85	15.95	24.61	23.65	5.43	0.19
MgO	1.31	0.03	0.08	0.02	0.37	0.81	4.04	2.49	4.28	4.93	12.88	13.35	14.39	16.19	16.62	0.65
MnO	0.09	0.05	0.06	0.05	0.04	0.03	3.58	5.65	0.97	0.65	0.14	0.08	0.51	0.52	0.08	0.00
CaO	0.03	0.00	1.18	2.66	0.26	0.06	3.41	3.18	2.22	2.51	0.16	0.02	0.16	0.19	12.67	0.27
Na_2O	0.16	0.17	10.98	10.33	5.59	2.51	0.00	0.01	0.10	0.00	0.37	0.38	0.05	0.01	1.59	0.17
K_2O	14.89	16.11	0.70	0.20	2.55	7.29	0.00	0.00	0.02	0.01	7.19	7.97	0.30	0.15	0.06	11.15
Cr_2O_3	0.02	0.00	0.03	0.00	0.06	0.03	0.05	0.06	0.04	0.04	0.07	0.00	0.00	0.09	0.12	0.00
Total	99.27	99.99	100.00	99.73	94.35	94.04	101.23	101.96	101.64	101.62	94.45	94.60	88.18	88.68	96.23	94.43
Norm [O]	**8.00**	**8.00**	**8.00**	**8.00**	**11.00**	**11.00**	**12.00**	**12.00**	**12.00**	**12.00**	**11.00**	**11.00**	**14.00**	**14.00**	**24***	**11.00**
a.p.f.u.																
Si	2.93	3.00	2.91	2.85	3.02	3.08	3.01	3.00	2.99	3.01	2.74	2.69	3.03	3.06	6.74	3.07
Ti	0.00	0.00	0.00	0.00	0.01	0.03	0.01	0.01	0.00	0.00	0.07	0.05	0.01	0.01	0.02	0.00
Al	0.99	1.00	1.07	1.13	2.92	2.78	1.96	1.99	2.03	1.97	1.66	1.76	2.32	2.18	2.05	2.84
Fe	0.09	0.02	0.02	0.01	0.04	0.05	2.02	2.05	2.21	2.19	1.05	1.00	2.14	2.03	0.65	0.01
Mg	0.09	0.00	0.01	0.00	0.04	0.08	0.47	0.29	0.50	0.57	1.44	1.49	2.23	2.48	3.54	0.06
Mn	0.00	0.00	0.00	0.00	0.00	0.00	0.24	0.38	0.06	0.04	0.01	0.01	0.05	0.04	0.01	0.00
Ca	0.00	0.00	0.06	0.13	0.02	0.00	0.29	0.27	0.19	0.21	0.01	0.00	0.02	0.02	1.94	0.02
Na	0.01	0.02	0.94	0.89	0.71	0.32	0.00	0.00	0.01	0.00	0.05	0.05	0.01	0.00	0.41	0.02
K	0.89	0.95	0.04	0.01	0.21	0.62	0.00	0.00	0.00	0.00	0.69	0.76	0.04	0.02	0.01	0.95
Cr	0.00	0.00	0.00	0.00	0.00	0.00	0.00	0.00	0.00	0.00	0.00	0.00	0.00	0.01	0.01	0.00
Total	**5.02**	**4.99**	**5.04**	**5.03**	**6.97**	**6.97**	**8.00**	**8.00**	**8.00**	**8.00**	**7.73**	**7.79**	**9.83**	**9.85**	**15.38**	**6.97**
Ca/(Ca+Na)			0.06	0.12												
K/(K+Na)					0.23	0.66										0.98
Mg/(Mg+Fe)							0.19	0.12	0.18	0.21	0.58	0.60	0.51	0.55		

*24(O, OH, F, Cl) with (OH, F, Cl) = 2 a.p.f.u. after Hawthorne et al. (2012)

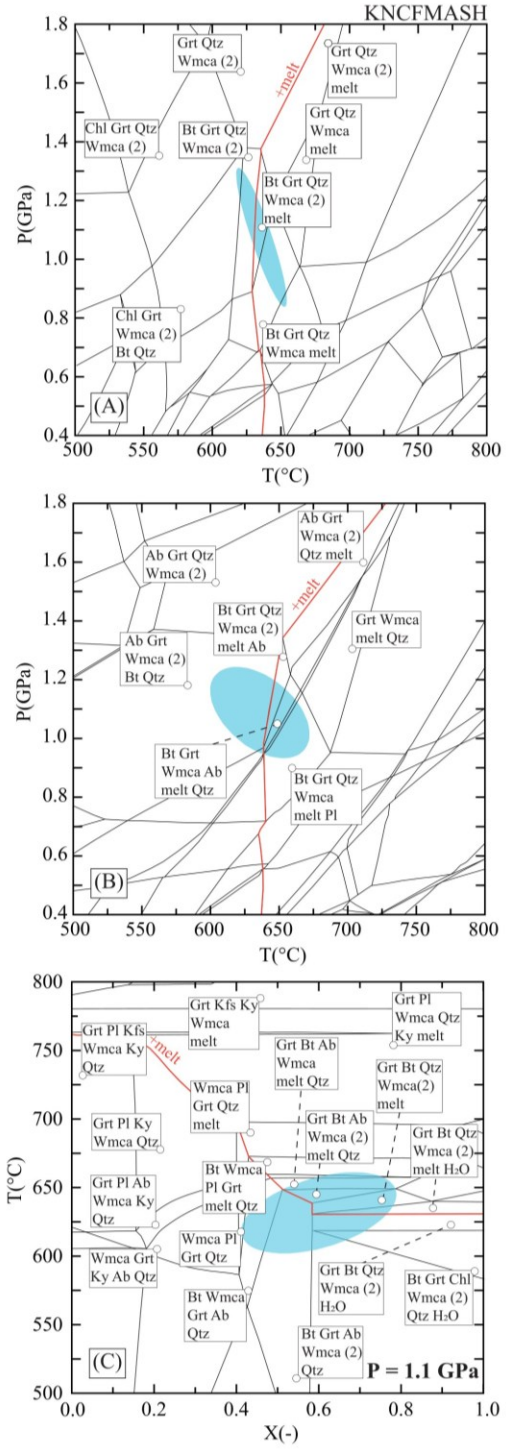

Figure 2.9: Phase-diagram *P-T* and *X-T* sections of the investigated metapelitic sample. Red line is the solidus. The blue ellipse (2σ) delineates the area in which the observed mineral compositions are best reproduced and were constructed with a Monte Carlo approach. (A) H_2O-saturated *P-T* section, (B) H_2O-undersaturated *P-T* section, (C) Variable H_2O, *X-T* section (at P:1.1GPa). The bulk compositions used to produce these diagrams are given in the supplementary material. Mineral abbreviations follow Siivola and Schmid (2007).

The isochemical *P-T* sections were also used to delineate the range of the *P-T* conditions of equilibrium that are indicated by the mineral chemistry of the coexisting phases. In the case of H_2O-saturated conditions and the dataset of Holland and Powell (1998) (Figure 2.9A), the observed GBMPPQ assemblage and the compositions of the coexisting minerals indicate 636±10 °C and 1.07±0.1 GPa as average *P-T* conditions (see Figure S. 2.4 of the supplementary material for the compositional isopleths). At these conditions, a small volume fraction of melt (<8%) is predicted. For H_2O-saturated conditions we additionally tested the total bulk composition and we obtained similar conditions but not a satisfactory fit of compositional isopleths (Figure S. 2.5 of the supplementary material). For the case of H_2O-undersaturated conditions (H_2O: 3.17 wt.%), the observed GBMPPQ assemblage and the compositions of coexisting biotite, garnet and muscovite point to 634°C ± 18 °C and 1.09 ± 0.07 GPa (Figure 2.9B). These results are in accordance with the water-saturated case. The predicted amount of melt in this case is less than 2% (by volume; Figure S. 2.4B). Finally, the results for the *T-X* section show the best fit (both in mineral assemblages and mineral compositions) at about X:0.60 ± 0.09 (i.e., H_2O: 3.35 wt.%), T:631±13 °C and at 1.1 GPa (Figure S. 2.3 of the supplementary material for details).

The results using the thermodynamic dataset Holland and Powell (2011) show a ~45 °C shift of the solidus toward higher temperatures (Figure S. 2.3 of the supplementary material). Additionally, biotite is no more stable beyond the solidus. Therefore, the calculated average *P-T* conditions can only lie below the solidus. The compositional isopleths representing the observed compositions of garnet, biotite, and muscovite do not cross-cut each other as closely as they do with the dataset of Holland and Powell (1998) (Figure S. 2.6 of the supplementary material). Although the fit is not optimal, the derived average *P-T* conditions are very similar. For water-saturated conditions the best fit is obtained at 621°C±15 °C and 1.25±0.05 GPa (Figure S. 2.6 of the supplementary material). For a fixed amount of water (H_2O: 3.17 wt.%) the best-fit temperature is 621°C±15 °C and the best-fit pressure is 1.19±0.05 GPa. In the *T-X* section, we calculated a temperature of 617°C ± 15°C and approximately 3.37 wt.% H_2O at a constant pressure of 1.1 GPa.

The error (2σ) ellipse in all cases was calculated using the compositions of the coexisting garnet, white mica (muscovite-rich) and biotite. We used the average X_{Mg} rim values of coexisting minerals and calculated a misfit (or error) function of the form:

$$\Omega = \left(X_{Mg}^{Grt} - Y_{Mg}^{Grt}\right)^2 + \left(X_{Mg}^{Bt} - Y_{Mg}^{Bt}\right)^2 + \left(X_{Mg}^{WMca} - Y_{Mg}^{WMca}\right)^2$$

where Ω is the misfit, X_{Mg} is the measured value of $Mg/(Mg + Fe)$ in the respective mineral, and Y_{Mg} is the modelled value as it is given by the routine "werami" in PERPLE_X. A good fit in the mineral compositions is where Ω is minimized in *P–T* space (i.e., when observed and modelled mineral compositions coincide; see also Hunziker et al., 2017 and Nerone et al., 2025). For the case of crossing isopleths, this approach is equivalent to finding the points of intersection of three respective compositional isopleths $\left(X_{Mg}^{Grt}, X_{Mg}^{Bt}, X_{Mg}^{WMca}\right)$. At the intersection points, $\Omega = 0$. The exact intersection points can be observed in Figure S. 2.4, Figure S. 2.5 and Figure S. 2.6 of the supplementary material.

To gain insight on the relative error of the estimated *P–T* conditions we performed a Monte Carlo analysis by perturbing the mean X_{Mg} by 1% in a random manner following a normal distribution of errors (as in Moulas et al., 2020). The perturbation of the respective X_{Mg} values was repeated 2,000 times. This perturbation agrees very well with the measured X_{Mg} ranges in all three minerals. Thus, for each combination of randomly perturbed $X_{Mg}^{Grt}, X_{Mg}^{Bt}$ and X_{Mg}^{WMca} values, the minimum point of the misfit function (Ω) was found in *P–T* space. The optimal conditions were derived by taking the average values of the best-fit points and using them to calculate their mean values and covariance.

To constrain the *P-T* conditions even further, we performed conventional thermobarometry. Figure 2.10 shows the results of garnet-biotite thermometry applied to porphyroblastic garnet rims and adjacent matrix biotite crystals. Assuming a pressure of about 1.1 GPa (see ensuing paragraph), the temperatures obtained are 619±9°C (1σ), 632±8°C (1σ) and 646±16°C (1σ) for the calibrations of Kleemann and Reinhardt (1994), Kaneko and Miyano (2004) and Hodges and Spear (1984) respectively. Using additional calibrations did not alter the results, therefore we will not consider other formulations any further.

Numerical mica-solvus thermometry (Blencoe et al., 1994; their eq. 11) for twelve coexisting muscovite-paragonite pairs (Figure 2.4; K map) yielded a temperature of 654±33°C (1σ) (Figure 2.11). The muscovite grains of these pairs are characterized by $Si_{a.p.f.u.}$ and X_{Ms} values of 3.09±0.03 and 0.7±0.03 respectively and give a temperature of 640±15°C when plotted on the muscovite limb of the two-mica solvus calculated for $Si_{a.p.f.u.} = 3.1$ at 1 GPa using the Coggon and Holland (2002) thermodynamic approach.

We additionally used the empirical garnet-muscovite, Fe-Mg exchange thermometer of Wu and Zhao (2006) and the garnet-phengite, Fe-Mg exchange thermometer of Green and Hellman (1982) (Figure S. 2.7). The garnet-muscovite thermometer is an empirical formulation based entirely on natural data (Wu and Zhao, 2006). However, the *P-T* range of its applicability falls within our previously mentioned estimations. For a fixed pressure of 1.1 GPa and assuming all iron in muscovite is ferrous, we obtained an average temperature of 602±7.8°C (1σ). The garnet-phengite thermometer has been originally calibrated based on phengite-rich mica and also at high temperatures (>800°C) and pressures (>20kbar). By extrapolation we obtained a temperature of 674±27°C (1σ) at 1.1 GPa. Although the use of this thermometer under these conditions and bulk rock composition should be inappropriate due to its calibration range, it nonetheless provides temperature estimates that align well with previous calculations. This suggests that, despite the limitations of extrapolation, the results remain consistent within the context of this study.

The results from all thermobarometric methods employed consistently indicate that the peak conditions are in the order of 630±20°C at 1.1±0.2GPa. These conditions are in accord with the onset of wet melting of relevant lithologies, constrained experimentally to lie at about ~630°C at such pressures (see review by Weinberg and Hasalová, 2015). Thus, all pieces of thermobarometric and textural evidence suggest that the temperature was of the order of 630°C.

2.4.6 Quartz in garnet elastic barometry

Apart from the classical thermobarometric methods discussed above, we also performed Quartz-in-Garnet (QuiG) elastic barometry. This method is based on the preserved residual pressures of quartz inclusions in garnet and can be used to obtain the apparent entrapment conditions. To calculate the residual pressure of quartz enclosed by garnet in our sample, we followed the method of Angel et al. (2019), also described in detail by Moulas et al. (2020). Briefly, this method utilizes the phonon-mode Grüneisen tensor in combination with the measured shifts of quartz vibrational modes to determine the strain components:

$$-\frac{\Delta\omega^m}{\omega_0^m} = \gamma_1^m(\varepsilon_1 + \varepsilon_2) + \gamma_3^m\varepsilon_3$$

where $\Delta\omega^m$ is the wavenumber difference of the vibration mode m of quartz, ω_0^m is the reference quartz wavenumber of vibrational mode m, γ_i^m are the components i of the Grüneisen tensor and ε_i are the components of the strain tensor (in Voigt notation). The value of $\Delta\omega^m$ can be calculated by subtracting the measured Raman shifts of the 206 and 464 cm^{-1} vibrational

modes of quartz from the reference values. The determination of the elastic strain components enables the calculation of the stress components with the use of the elasticity (stiffness) matrix of quartz (Appendix B in Moulas et al., 2020). Subsequently, pressure can be calculated as $P = -\frac{1}{3}(\sigma_1 + \sigma_2 + \sigma_3)$.

To avoid relaxed quartz inclusions, the maximum residual pressure of quartz in garnet was subsequently used to construct an isomeke. An isomeke represents a line in *P-T* space along which quartz and garnet coexist without developing a pressure difference (Angel et al., 2015). The choice of the maximum residual pressure for the construction of the isomeke aims to avoid inclusions that experienced relaxation due to fracturing or near-surface effects (Enami et al., 2007). We followed two different approaches to calculate the isomeke. In the first approach, we assume linear elasticity, constant thermoelastic properties and isotropy in the host-inclusion system as in Moulas et al. (2020). In the second approach, we utilized a non-linear solution of the inclusion-in-host problem that assumes the finite strain effects of the volumetric deformation but approximates the shear deformation using a small-strain assumption (Moulas et al., 2023). In this non-linear method, entrapment conditions can be determined once the volumes of quartz and garnet at initial and final *P-T* conditions are known. Therefore, relevant Equations of State (EoS) are required. An analytical description of the entire procedure, the Equations of State used as well as the parameters and moduli utilized for the elastic barometry in this paper are provided in the supplementary material.

The data presented in Figure 2.12A highlight the existence of numerous quartz inclusions retaining residual pressures above 0.2 GPa. The highest calculated pressure was 0.387 GPa. This maximum pressure value was subsequently used to construct the isomeke plots of Figure 2.12B. For an assumed temperature of 500 °C, the linear isomeke predicts an entrapment pressure of 1.08±0.01 GPa (1σ). Using a temperature of 630°C—in line with thermobarometric estimations—the mean entrapment pressure increases to 1.20±0.01 GPa (1σ). For the case of the non-linear isomeke the results are comparable. A pressure of 1.12±0.02 GPa (1σ) for 500 °C and 1.29±0.02 GPa (1σ) for 630 °C were calculated. Considering the potential sources of error amongst the different methods employed, the QuiG barometry results are in agreement with our previously derived *P-T* conditions.

2.5 Discussion

2.5.1 Determination of peak metamorphic conditions

The evident consistency between petrographic observations and thermobarometric and phase equilibria calculations strongly suggests that the studied metapelitic sample from the Pindos metamorphic sole underwent upper amphibolite-facies conditions. The estimated temperature is 630±20°C while the estimated pressure is 1.1±0.2GPa. These findings contrast with earlier studies (Jones et al., 1992 and references therein) that proposed greenschist-facies conditions for metapelites in the region. However, our results align closely with those reported for amphibolite-facies mafic lithologies in the Pindos sole (Jones and Robertson, 1991; Kemp and McCaig, 1984; Myhill, 2011). They also agree with similar lithologies in Albanian ophiolites (Dimo-Lahitte et al., 2001) and the Koziakas ophiolite to the south (Pomonis et al., 2002). Worth-mentioning here is the *P–T* determination of Myhill (2011, p. 87) for a garnet-bearing pyroxenite boudin present within a quartzofeldspathic shear-zone melt within mafic amphibolite from the very same locality in the Pindos sole. This anhydrous assemblage yields an optimal *P–T* estimate of 650°C and 1±0.1GPa for a water activity of 0.1, in excellent agreement with our determination.

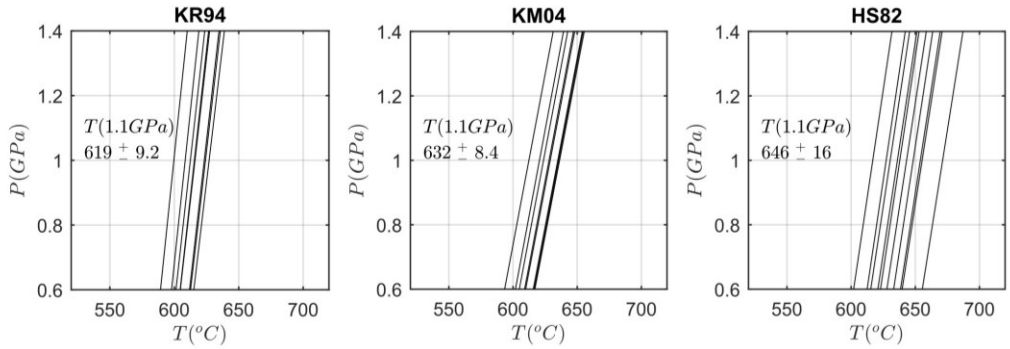

Figure 2.10: Geothermometry results for garnet-biotite pairs using the formulations of Kleeman and Reinhardt (1994; KR94), Kaneko and Miyano (2004; KM04) and Hodges and Spear (1982; HS82). Temperatures were estimated assuming a pressure of 1.1 GPa. The error indicated is the standard deviation based on the different pairs measured.

As mentioned earlier, the studied sole metapelite is characterized by the presence of large K-feldspar ribbons within the matrix, as well as in localized zones and fractures associated with garnet. Our equilibrium thermodynamic calculations could not produce any field that includes K-feldspar along with the observed mineral assemblage. According to Clemens (1984, Figure 2), K-feldspar can form at relatively high temperatures (~680°C) and very low pressures

(<1kbar) or above 700°C at higher pressures. These findings were also supported by subsequent experimental studies (e.g., Carrington and Watt, 1995). However, such conditions indicate the onset of granulite-facies metamorphism and do not match our inferred *P-T* estimates.

Clemens (1984) also showed that K-feldspar could result from muscovite dehydration at 600–650 °C under relatively low pressures (2.6–4.6 kbar). Interestingly, K-feldspar in our sample was observed to be associated with muscovite (e.g., Figure 2.3D). On another occasion, Fukuda et al. (2012) demonstrated that secondary K-feldspar can precipitate from K-rich fluids, but this process produces a fine-grained texture and requires pre-existing K-feldspar porphyroclasts. Based on the previous discussion we offer two possible explanations. The large K-feldspars could represent (a) out-of-equilibrium, dehydration products after muscovite in a later stage of the evolution of the rock, (b) remnants of a high-temperature assemblage. The presence of K-feldspar within veins in garnets, or its coexistence with plagioclase and quartz in localized regions surrounding garnets likely represents the existence of a haplogranitic melt. Our phase-equilibria models support this interpretation, predicting small degrees of partial melting under the conditions of interest (Figure 2.9). Based on PERPLE_X, the melt composition at the conditions of interest spans from haplogranitic to granodioritic, with 60 wt.% SiO_2, 13 wt.% Al_2O_3, 7 wt.% Na_2O, and 19 wt.% H_2O on average.

2.5.2 Elastic barometry and garnet growth

In recent years, the QuiG barometer has served as a reliable tool for determining entrapment conditions based on the phonon-mode Grüneisen tensor. The accuracy of the QuiG barometer has also been demonstrated experimentally (Bonazzi et al., 2019). The application to the studied metapelitic sample indicated pressures between 1.1 and 1.3 GPa at temperatures ranging from 500 to 630°C. These results align well with the rest of our thermobarometric estimates. The calculated pressures correspond to the possible entrapment conditions of quartz in garnet. However, it is possible that the Grüneisen tensor approach could overestimate the residual pressure by up to 0.1GPa (Figure S. 2.9 of the supplementary material). Applying this correction would shift the isomeke lines toward lower pressures, bringing them into precise agreement with the *P–T* conditions inferred from thermobarometry. It is also noted that the inferred conditions from elastic barometry may not necessarily coincide with the chemical equilibration of the rock and could represent a distinct stage in the *P-T-t* evolution of the metapelite (Spear and Wolfe, 2020).

Zhong et al. (2020) demonstrated that the viscous relaxation of the host phase (garnet) could play a significant role in the preservation of residual pressure in quartz. At higher temperatures, the QuiG system is more prone to viscous relaxation, especially in cases where these temperatures are experienced for significant amounts of time. The process of viscous relaxation can significantly lower the pressure maintained by quartz. As a result, pressure estimates based on the isomeke concept may not reflect the original entrapment conditions, but they may rather be closer to the peak-*T* conditions. This effect has been observed, for example, in calc-silicate gneisses from the Rhodope Massif (Moulas et al., 2020). Additionally, garnet weakening and therefore pressure modification is expected in the presence of an aqueous fluid (Zhong et al., 2024). In the present work, the isomeke lines clearly indicate *P*-*T* conditions which coincide well with our peak thermobarometric and phase-equilibria estimates (1.1 to 1.3 GPa). Therefore, we expect that the effect of viscous relaxation is negligible beyond the inferred peak temperatures (T<630°C).

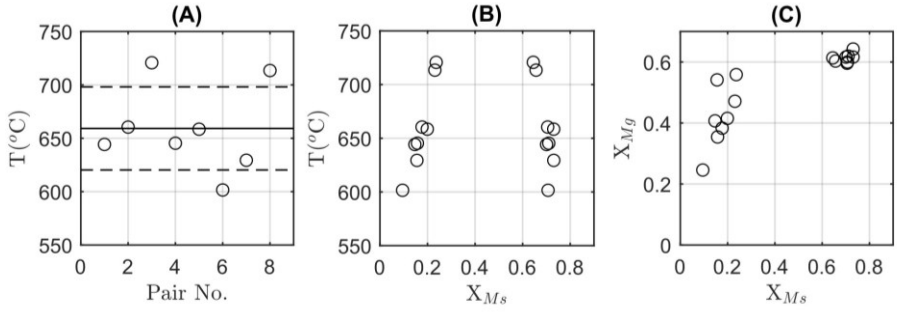

Figure 2.11: Mineral chemistry and temperature estimates for coexisting white mica (muscovite-paragonite) pairs. The temperature was estimated using the formulation of Blencoe et al., (1994). (A) Two-mica solvus temperature estimates of individual pairs. The solid line indicates the mean temperature for all pairs, and the dashed lines indicate the limits of $\pm 1\sigma$. (B) Temperature as a function of muscovite content (X_{Ms}) in K-rich and Na-rich micas. (C) X_{Mg} [Mg/(Mg+Fe) molar ratios] of coexisting white micas as a function of their muscovite content.

2.5.3 $^{40}Ar/^{39}Ar$, U-Pb ages and time constraints

$^{40}Ar/^{39}Ar$ dating is commonly discussed in the literature with respect to its closure temperature (e.g., Parlak and Delaloye, 1999; Palandzhyan et al., 2011). An $^{40}Ar/^{39}Ar$ age is usually thought to represent the "moment" where a system cooled below the closure temperature of argon for the specific mineral being analyzed (Schaen et al., 2021 and references therein). For the case of amphibole, Harrison (1982) determined Ar-closure temperatures in the range between 578 to 490°C for variable cooling rates and assuming a monotonic cooling path.

In our sample, amphibole showed a well-defined age plateau at 165.5±0.73Ma. This particular apparent age profile is a strong indication that amphibole has not been affected by diffusion or secondary alteration processes that would have led to either argon loss or gain (e.g., Jourdan, 2012 and references therein). If amphibole crystallization was immediately followed by rapid cooling, the measured $^{40}Ar/^{39}Ar$ age could reflect the actual time of formation. It is also expected that amphibole remained unaffected by any reheating events after cooling below its closure temperature (e.g., Parlak et al., 2019).

Muscovite closure temperatures proposed by Harrison et al. (2009) are largely dependent on cooling rate, grain size and pressure. For a cooling rate of 10°C/Ma and a grain size of 100µm, the closure temperature of Ar in muscovite at 10kbar is 425°C. In any case, the closure temperatures of muscovite are lower compared to those of amphibole. The investigated muscovite from the metapelite gave an apparent age of 164.16±0.37Ma but showed evidence of argon loss during the initial heating steps. Argon loss could be a result of diffusion or alteration and phase mixing processes. Since we did not observe any alteration associated with the analyzed muscovite or phase mixing with paragonite on the analyzed separate, we attribute the Ar loss to the effect of diffusion. As a consequence, this represents a partial reset of the $^{40}Ar/^{39}Ar$ age, and therefore, it is interpreted as a minimum estimate (e.g., Cassata et al., 2009).

The U-Pb analyses aimed at dating garnet growth were strongly influenced by high concentrations of U and Th. Typically, regional metamorphic garnets contain very low concentrations of U and Th (e.g., Millonig et al., 2020; Peillod et al., 2024). This suggests that our results were affected by inclusions of monazite and zircon/rutile. Walters et al. (2025) showed that such micro-inclusions can be problematic in garnet U-Pb geochronology because they may also produce well-defined regression lines. In our case, the analyses yielded a clear regression line with a lower intercept age of 178.5±4.8Ma. We consider this age unreliable because it reflects solely the inclusions. The measured age is also much older than our $^{40}Ar/^{39}Ar$ ages and may instead represent the crystallization of the inclusions. If so, these inclusions could be coeval with garnet formation. However, as Walters et al. (2025) noted, using a garnet standard to infer the age of inclusions in garnet may provide significantly inaccurate ages. For these reasons, we do not regard the U-Pb age of inclusions in garnet as robust and will exclude it from further interpretation. The accurate determination of the ages of inclusions such as monazite and zircon could provide additional insights and may be pursued in future studies.

In this study, we demonstrate a tight relationship between metamorphic sole formation (our measured $^{40}Ar/^{39}Ar$ ages) and generation of oceanic crust (gabbro U-Pb crystallization age of Liati et al. 2004) in the Pindos ophiolite. The consistent preservation of mid-Jurassic ages in the sole rocks indicates that the $^{40}Ar/^{39}Ar$ system remained unaffected by any subsequent tectono-metamorphic events or thermal resetting since the final cooling of the metamorphic sole. We notice, however, that the gabbro U-Pb age was determined by a single measurement with a high $^{207}Pb/^{206}Pb$ ratio and a large 1σ error. Therefore, it is important that the gabbros from the Pindos ophiolite are precisely redated in future work. Our new $^{40}Ar/^{39}Ar$ measurements bracket better the cooling age of magnesio-hornblende in sole amphibolites compared to previously reported data (Spray et al., 1984). Moreover, the new and accurate determinations of cooling ages for amphibole and muscovite can be used to constrain the rate of cooling from the closure temperature of amphibole (~550°C) to that of muscovite (~400°C). Considering the largest deviation in the ages obtained for the two minerals, based on their 2σ errors, then cooling from 550 down to 400°C must have occurred within 2.5Ma. These estimates are consistent with studies from the Beyşehir-Hoyran ophiolite in the Central Taurides (Parlak et al., 2019). If, on the other hand, one takes the smallest difference between the cooling ages of amphibole and muscovite then only 0.24Ma would be required for the cooling interval. The implied cooling rate estimates exceed 60°C/Ma in the most conservative scenario and reach up to 625°C/Ma. However fast the cooling of the sole rocks may have been, the cooling rate must have been fast enough to prevent the viscous relaxation of quartz inclusions in garnet and to preserve the sharp chemical zonation in garnet porphyroblasts. Further investigations are needed to quantify the extend of relaxation of both the mechanical and the chemical processes in these rocks.

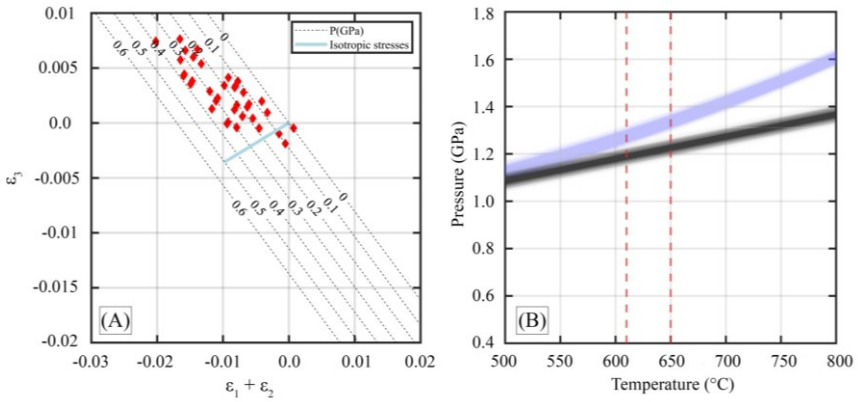

Figure 2.12: Results of quartz-in-garnet elastic barometry. (A) Elastic strain components in relation to the residual pressure of quartz (contours). The blue line represents the conditions of

isotropic stresses. The maximum measured residual pressure was 0.387 GPa. (B) Probability density for isomeke lines calculated based on the maximum residual pressure (0.387 GPa). The black density region represents the linear isomeke while the purple region represents the non-linear isomeke (see main text for further details). A Monte Carlo approach with 2000 iterations was used to generate the probability densities. The red dashed vertical lines indicate the approximate limits for the temperature estimates (630±20°C).

The cooling rates estimated for the Pindos metamorphic sole have important implications for the mechanisms active during ophiolite emplacement. Comparable rates have been calculated for the metamorphic sole of the Oman ophiolite (Hacker et al., 1996). The peak *P-T* conditions calculated in this work, together with the inferred cooling rates, are consistent with the presence of a ductile shear zone (Kiss et al., 2019). This interpretation for metamorphic soles has already been supported by several numerical studies both on the geodynamic (Duretz et al., 2016) and on the local scale (Ibragimov et al., 2024). More specifically, Ibragimov et al. (2024) reproduced the expected *T-t* path of the Oman metamorphic sole using shear-heating models, while Burg & Moulas (2022) showed that rapid cooling, similar to the one suggested for the sole rocks in our study, follows the cessation of shearing. These earlier works, along with our results, constitute strong proof that shear heating was significant (along with conductive heating) during the generation of the Pindos metamorphic sole. More recently, Garber et al. (2025) provided additional evidence for the role of shear heating in the Samail ophiolite (Oman), further strengthening this interpretation. Together with the results shown in Garber et al. (2025), our results support that shear heating may be very common during ophiolite emplacement.

2.5.4 Emplacement and kinematic indicators

According to tectonic plate reconstructions, from Anisian to early Norian times (240-220Ma), the closure of the Paleo-Tethys system initiated several back-arc oceans (Stampfli and Borel, 2002). The origin of the Pindos ophiolite in Greece has been debated, with uncertainty over whether it formed in an ocean to the east (e.g., Maffione and Van Hinsbergen, 2018) or west of the Pelagonian microcontinent (Ghikas et al., 2010 and references therein). In our studied sole rocks, the rotational character of syn-kinematic garnet porphyroblasts (e.g., Figure 2.2D) is not conclusive since different directions of shear have been deduced (although most grains show a top-to-the-NE direction). Such inconclusive data have been observed in similar rocks further north in Albania (Dimo-Lahitte et al., 2001) and can be explained by the interactions of porphyroblasts in a deforming, anisotropic rock matrix (Griera et al., 2013). By

contrast, the kinematic analysis of ductile S-C structures (Figure 2.2E-F) is consistent with shearing topping east, hence a westerly origin of the metamorphic-sole rocks. Rassios and Dilek (2009) have also demonstrated that the Pindos–Vourinos ophiolites have retained their relative orientations from the time of cessation of ductile deformation within the ophiolitic slab. Unless the ophiolites have been so severely dismembered and disarranged subsequent to their initial emplacement that any consistency in trends shown by fabrics and structures from within the metamorphic sole is unlikely to reflect original orientations, all macro- and microtectonic data taken together clearly support a top-to-the-NE sense of shear during emplacement of the Pindos and Vourinos ophiolites (Ghikas et al., 2010 and references therein).

2.6 Conclusions

Several key points emerge from the data and discussion above. Petrographic observations and thermobarometric and phase equilibria calculations for the Pindos metamorphic sole rocks, all unambiguously point to upper-amphibolite facies conditions (~630°C and 1.1GPa) for the studied garnet-bearing metapelite. The effect of viscous relaxation on the residual pressures recorded by quartz seems to be negligible. New $^{40}Ar/^{39}Ar$ ages for muscovite (164.16±0.37Ma) and magnesio-hornblende (165.5±0.73Ma) from the metamorphic sole constrain the time of emplacement of the Pindos ophiolite and constitute evidence of rapid cooling, indicative of fast, transient processes. The preservation of mid Jurassic $^{40}Ar/^{39}Ar$ ages suggests that the system has remained undisturbed by later tectono-metamorphic events. Provided that post-emplacement deformation has not reorientated the initial ductile structures, our kinematic data suggest a westerly origin of the Pindos ophiolite.

2.7 Supplementary material

2.7.1 $^{40}Ar/^{39}Ar$ dating details

After being neutron-irradiated with a TRIGA experimental reactor at the Radiation Center of the Oregon State University, the samples were subjected to incremental, bulk laser heating that led to continuous degassing. The incremental heating occurred over 57 steps for the amphibole and 53 steps for the muscovite. The extracted gases were isolated for 3 minutes and then analyzed with the ARGUS-VI-G multi-collector mass spectrometer. This type of spectrometer is optimal for samples that have possibly been affected by secondary processes. The reference standard was the FCT-NM sanidine with an age of 28.201±0.00420 Ma and an irradiation parameter (J) of 0.00317667±0.00000273 (Kuiper *et al.*, 2008). The atmospheric $^{40}Ar/^{36}Ar$ ratio was 297.4220±0.3777 while the reference atmospheric ratio was taken from Lee

et al. (2006). To calculate $^{40}Ar/^{39}Ar$ ages and associated errors, the equations of Min et al. (2000) were applied. More details can be found at: https://osu-argon.org/

2.7.2 U-Pb details

The procedure followed for the U-Pb dating in garnets is described in detail in Beranoaguirre et al. (2022). Mass bias, inter-element fractionation and instrumental drift were corrected by repeatedly measuring the soda-lime glass SRMNIST614 (Jochum *et al.*, 2011) during the analytical session. The garnet reference material from Mali (Seman *et al.*, 2017) was used as a matrix-matched standard to correct for differences in ablation behavior between garnet and NIST glass. For quality control, an in-house garnet reference material from Balochistan (TIMS age ca. ~45.5 Ma) was utilized in the measurements. Data reduction and correction were performed offline with the VBA spreadsheet developed by Gerdes and Zeh (2006, 2009). Uncertainties are reported at the 2σ level and were calculated following the recommendations outlined by Horstwood et al. (2016).

2.7.3 Phase Equilibria approach and solid solution models

In the first approach using the thermodynamic dataset of Holland and Powell (1998), the CORK equation of state was used (Holland and Powell, 1998). Additionally, the following solid-solution models were utilized: Bio(TCC) for biotite (Tajčmanová *et al.*, 2009), Mica(CHA) for white mica (Coggon and Holland, 2002), hCrd for cordierite (ideal), "feldspar" for K-feldspar and plagioclase (Newton *et al.*, 1980; Fuhrman and Lindsley, 1988), Gt(GCT) for garnet (Ganguly *et al.*, 1996), St(HP) for staurolite (parameters from THERMOCALC), Opx(HP) for orthopyroxene (Holland and Powell, 1996), melt(HP) for silicate melt (Holland and Powell, 2001; White et al., 2001), Chl(HP) for chlorite (Holland et al., 1998), Ctd(HP) for chloritoid (White *et al.*, 2000), Sp(HP) for spinel (Holland and Powell, 1998), and Omph(GHP) for clinopyroxene (Green et al., 2007).

For the second set of calculations, we employed the Pitzer and Sterner (1994) equation of state for H_2O in accordance with Holland and Powell (2003) which is the appropriate choice for the selected thermodynamic dataset of Holland and Powell (2011). The following solution models have been used: Fsp(C1) for K-feldspar and plagioclase (Holland and Powell, 2003), melt (W) for silicate melt, Gt(W) for garnet, Opx(W) for orthopyroxene, Mica(W) for white mica, Ctd(W) for chloritoid, St(W) for staurolite, Bi(W) for biotite, Omph(GHP) for clinopyroxene (Green et al., 2007) and Sp(WPC) for spinel (White *et al.*, 2002). Solution models denoted by (W) were taken from (White *et al.*, 2014).

2.7.4 Details on the calculation of mineral modes and Effective Bulk Composition (EBC)

Detailed compositional maps were obtained using the electron microprobe. For each mapped area we obtained two-dimensional arrays of the counts for MgO, K_2O, CaO, FeO and MnO using Wavelength-Dispersive Spectrometers (WDS), whereas counts for Al_2O_3, SiO_2 and Na_2O were obtained using Energy-Dispersive Spectrometry (EDS). The resulting arrays were used to investigate the distribution of mineral phases. The algorithmic investigation was performed in both an automatic and a manual manner. For the automatic identification of phases, MATLAB's ® native k-means clustering algorithm was used. This approach was correct in identifying ca 98% (in area) of the mineral phases. However, as automatic identification of phases would omit small biotite crystals that would be present, we did not consider this approach further. Therefore, a manual selection for the compositional limits was used in the clustering. The results of this manual phase identification were corroborated via quantitative point analysis.

Having determined the modal distribution of the various phases and their representative chemical compositions we were able to calculate the EBC of the mapped areas. This was done by taking the relative proportions of the areas of individual minerals and adjusting them for their respective densities. It was assumed that the area proportions of the minerals (sections in 2d) were good approximations of their volume proportions. Density values used are as follows: 4.00 for garnet, 3.00 for chlorite, 3.00 for biotite, 2.80 for white mica (undifferentiated), 2.56 for K-feldspar and 2.65 for quartz (all in gr/cm^3). In cases where zoned minerals were present (e.g., garnet porphyroblasts), only their outer rim (5% of the radius, adjusted for volume ratio) was considered in the calculation of the EBC. A different percentage for the garnet rim contribution was also considered (10%) without essentially changing the results. Therefore, only the results that utilized 5% of the outer garnet radius will be described in detail.

For the calculation of mineral modes, we considered the number of pixels (N_p) for each phase that were identified during the clustering analysis. These numbers were considered as proxies for the volume proportions of the phases. The volume proportions can then be multiplied by the respective density of each phase (ρ_p), to obtain mass proportions (M_p). Mass proportions can be adjusted by some weighting factor (w_p) as follows:

$$M_p = w_p N_p \rho_p \qquad \text{(G1)}$$

For all minerals, w_p was taken equal to 1. However, since we consider that only the outer rim of the garnet porphyroblasts is in thermodynamic equilibrium with the matrix, w_p for garnet must be significantly smaller than 1. The weighting factor for garnet is given by:

$$w_p = \left(\frac{4}{3}\pi r^3 - \frac{4}{3}\pi[(1-0.05)r]^3\right) / \left(\frac{4}{3}\pi r^3\right) = 1.00 - (0.95)^3 = 0.14 \quad \text{(G2)}$$

where number 0.05 specifies that only the outer 5% of the garnet radius contributes to the calculation of its volume. The result implies that only 14% of the garnet volume is considered in the calculations.

Using the values of N_p, ρ_p and w_p for each phase, one can calculate the mass contributions (X_p) as follows:

$$X_p = \frac{w_p N_p \rho_p}{\sum_{p=1}^{6} w_p N_p \rho_p} \quad \text{(G3)}$$

These contributions sum up to 1.0 and indicate the weight fraction of each solid phase in the calculation of the EBC. The calculated weight fractions X_p for each mineral are shown below.

Minerals	N	ρ	w	M	X
garnet	31540.00	4.00	0.14	17662.40	0.05
chlorite	13240.00	3.00	1.00	39720.00	0.12
biotite	1303.00	3.00	1.00	3909.00	0.01
white mica	77066.00	2.80	1.00	215784.80	0.63
K-feldspar	9489.00	2.56	1.00	24291.84	0.07
quartz	15146.00	2.65	1.00	40136.90	0.12
			Sum	341504.94	1.00

The calculation of the effective bulk composition (EBC) is performed by considering the oxides (in wt.%) constituting each mineral. The composition of the minerals was estimated by averaging the measured compositions in the region of interest. The following table summarizes the representative mineral compositions that were used (MnO and TiO_2 were not considered; see main text for details).

Minerals	SiO_2	Al_2O_3	FeO	MgO	Na_2O	K_2O	CaO
garnet	38.61	21.36	34.08	4.88	0.02	0.01	2.33
chlorite	28.28	21.67	33.77	4.71	0	0	0
biotite	36.60	18.86	16.85	12.88	0.37	7.19	0.16
white mica	46.71	35.36	1.05	1.03	2.27	7.49	0.03
K-feldspar	64.63	18.36	0	0.00	0.34	15.66	0.00
quartz	100.00	0.00	0.00	0.00	0.00	0.00	0.00

Finally, the total amount of each oxide (E_i) is given by summing up the values of the oxide in the respective minerals (O_p^i).

$$E_i = \sum_{p=1}^{6} X_p \, O_p^i \tag{E4}$$

The results for all oxides are then normalized to 100%. Using the approach outlined, we calculated the following effective bulk composition (EBC; in wt.%):

SiO_2	Al_2O_3	FeO	MgO	Na_2O	K_2O	CaO
54.43	29.02	6.91	1.68	1.55	6.26	0.15

The calculated EBC was taken at the limit of H_2O saturation (used in Figure 2.9A of the main text). For the H_2O-undersaturated composition (used in Figure 2.9B of the main text) we considered the following values (in wt.%):

SiO_2	Al_2O_3	FeO	MgO	Na_2O	K_2O	CaO	H_2O
52.71	28.10	6.70	1.64	1.49	6.06	0.14	3.17

For the calculations in Figure 2.9C of the main text, we considered variable H_2O content, ranging from 2.19 to 4.13 (wt. %). All other oxide ratios remained unchanged.

For the calculations using the Holland and Powell (2011) dataset, we additionally included Mn in the form of MnO:

SiO_2	Al_2O_3	FeO	MgO	Na_2O	K_2O	CaO	MnO
54.38	28.99	6.90	1.68	1.54	6.25	0.15	0.10

SiO2	Al2O3	FeO	MgO	Na2O	K2O	CaO	MnO	H2O
52.62	28.05	6.68	1.63	1.49	6.05	0.14	0.09	3.17

2.7.5 Raman spectrometry

An objective lens (100x) with a numerical aperture of 0.75 was employed whereas a He-Ne, 632.8 nm (red) laser was used. The resulting laser beam diameter was ~0.86 μm. The spectrometer slit was set to 50 μm and the diameter of the confocal hole was 400μm. Wavenumbers were measured in the range between 120 and 1200 cm^{-1}. Additionally, a grating of 1800 lines/mm was adopted. Each final spectrum was obtained by averaging five individual spectra that were acquired over 15 seconds each. The Renishaw Wire 1.3 software along with the GRAMS/32 spectroscopy software were used to control both the machine and the microscope. We obtained spectra of quartz inclusions in garnet to measure the residual pressure. Spherical quartz inclusions were primarily analyzed to avoid geometric and non-elastic effects (Campomenosi *et al.*, 2018; Mazzucchelli *et al.*, 2018; Morganti *et al.*, 2020).

2.7.6 Elastic Barometry

For the calculation of the residual pressure, the values of the Grüneisen components for quartz have been taken from the ab initio/DFT (Density Functional Theory) study of Murri et al. (2019). The components of the stiffness matrix at room conditions were taken from Wang et al. (2015).

For the calculation of the isomeke lines that represent entrapment conditions, two different approaches were followed. In the first approach, we used the equation of Zhang (1998), modified by Moulas et al. (2020). The bulk moduli of garnet end members at room conditions were sourced from Angel et al. (2022), the shear moduli from Wang and Ji (2001), and the thermal expansivities from Fei (1995). For quartz we have used the thermoelastic properties given in Angel et al. (2015). An average core composition of garnet with X_{Alm} = 0.71, X_{Prp} = 0.1950, X_{Grs} = 0.065 and X_{Sps} = 1- X_{Alm} - X_{Prp} - X_{Grs} (all molar fractions) was used. Each modulus was assumed to be a linear mixture of the moduli of the end-members (Moulas *et al.*, 2020). The size for quartz inclusion and garnet was set to 20 and 400μm, respectively, based on the average sizes of the two phases in the rock. We assumed a final temperature of 25 °C and a final external pressure of 1 bar (10^{-4} GPa). To account for analytical uncertainties, we followed a Monte Carlo approach as in Moulas et al. (2020) by perturbing the composition of garnet, the sizes of the two minerals and the residual pressure of quartz by 1% for 2000 iterations (Moulas et al., 2020).

In the second approach, we utilized the non-linear equation of Moulas et al. (2023). This approach seems to be the most accurate, yet simple, approximation of the complete finite-

strain solution of the host-inclusion problem (Levin *et al.*, 2021). For the case of garnet, we applied the EoS of Angel et al. (2022). This approach considers the Birch-Murnaghan formulation combined along with the concept of the Mie-Grüneisen-Debye thermal pressure (Liu and Li, 2006) to account for temperature-dependent volume changes. This EoS is not invertible and is primarily used to calculate pressure at specific Volume-Temperature (*V*-*T*) conditions. Therefore, the 'fzero' MATLAB® routine was used to numerically invert it, and acquire volume at *P*-*T* pairs. The values of reference bulk moduli, first and second pressure derivatives of bulk moduli, volumes, Debye temperatures and Grüneisen parameters of garnet end members were taken from Angel et al. (2022).

The volume of quartz at different *P*-*T* conditions was calculated using the EoS of Angel et al. (2017). In this EoS the linear transition from alpha- to beta-quartz is also considered. The chosen EoS is based on the bare phase concept (Carpenter et al., 1998) and the Landau theory (see Angel et al., 2017 for more details). In this model the volume of quartz is the sum of the bare phase (high-symmetry) volume and an excess volume associated with structural imperfections. Equation 2 in Angel et al. (2017) describes this relationship. The bare phase volume and temperature effects were calculated using the invertible Tait EoS and the Berman expression as in Angel et al. (2017). The properties of the alpha- to beta-quartz transition and the bare phase parameters were taken from Angel et al. (2017). Finally, the calculated volumes of quartz and garnet were tested and yielded identical results to EosFit7c (Angel *et al.*, 2014). The benchmarking for several *P*-*T* pairs is shown in Figure S. 2.8. Mingardi et al. (2025) recently demonstrated that models such as the one proposed by Angel et al. (2017) exhibit inaccuracies in determining the adiabatic bulk modulus within the stability field of β-quartz. Their findings suggest that additional factors must be considered to improve the accuracy of these models. However, the pressure-temperature conditions examined in the present study fall well within the stability field of α-quartz. The position of the isomeke line also remains entirely within this stability field.

2.7.7 Supplementary Figures

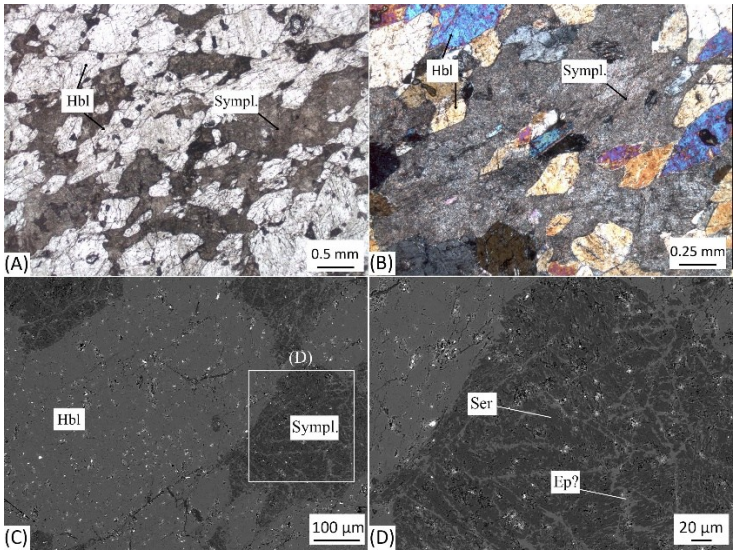

Figure S. 2.1: (A) plane polarized and (B) cross polarized light photomicrographs showing the main texture of the amphibolite. Amphibole is the dominant mineral phase in the sample, comprising 60-65% of its volume. (C) and (D) are Back-Scattered Electron images showing the intergrowth replacing plagioclase in the amphibolite. The intergrowth is made of sericite (fine-grained muscovite) and possibly epidote. Epidote could not be measured accurately due to beam damage and small grain size.

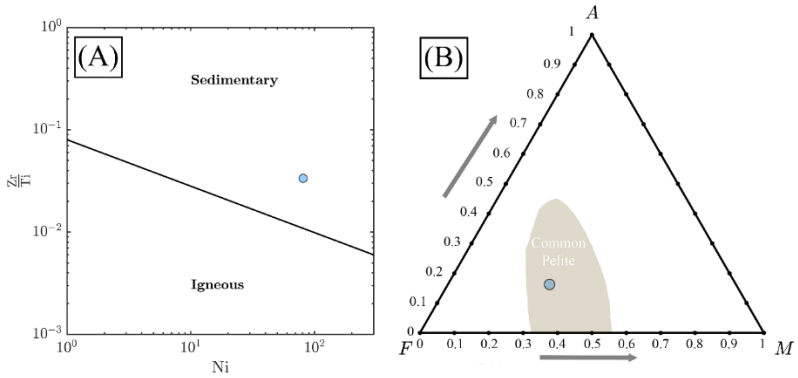

Figure S. 2.2: (A) Zr/Ti vs Ni classification diagram (Hamdja Ngoniri et al., 2020 and references therein) showing the sedimentary affinity of our studied metapelitic sample. (B) AFM ternary diagram projected from muscovite and corrected for paragonite where A = Al_2O_3 – $3K_2O$ – $3Na_2O$, F = FeO and M = MgO. Our metapelite plots at the low-Al field. The common pelite field is taken from Winter (2014).

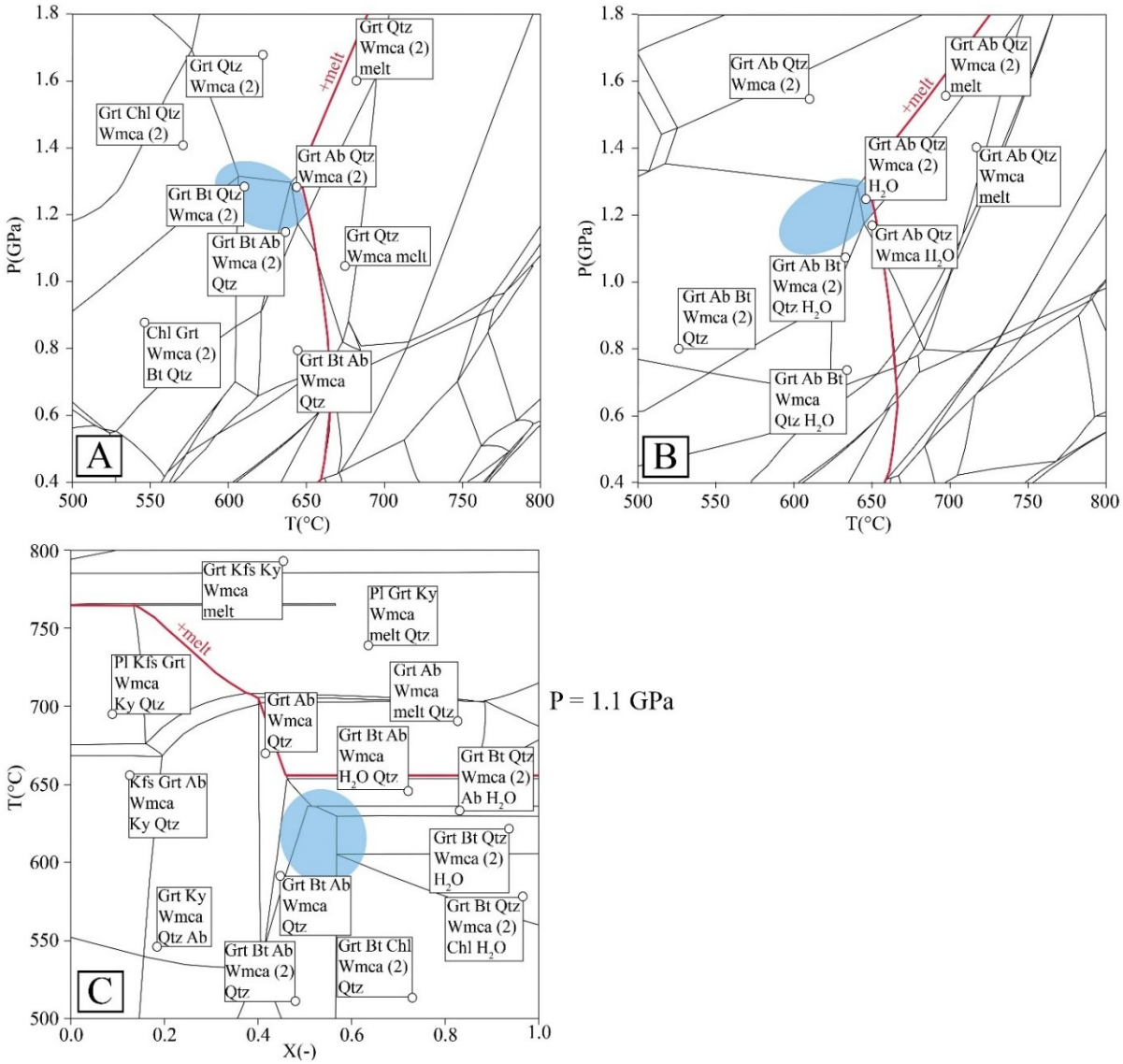

Figure S. 2.3: Isochemical *P-T* and *X-T* sections constructed with the database of Holland and Powell (2011) and the relevant solid-solution models (see main text for more details). Red line indicates the solidus. The blue ellipse (2σ) presents the area in which the observed mineral compositions and the assemblage are best reproduced. (A) H_2O-saturated conditions, (B) H_2O-undersaturated conditions, (C) variable H_2O *X-T* section at a pressure of 1.1 GPa. Mn is included in the bulk compositions. Mineral abbreviations after Siivola and Schmid (2007).

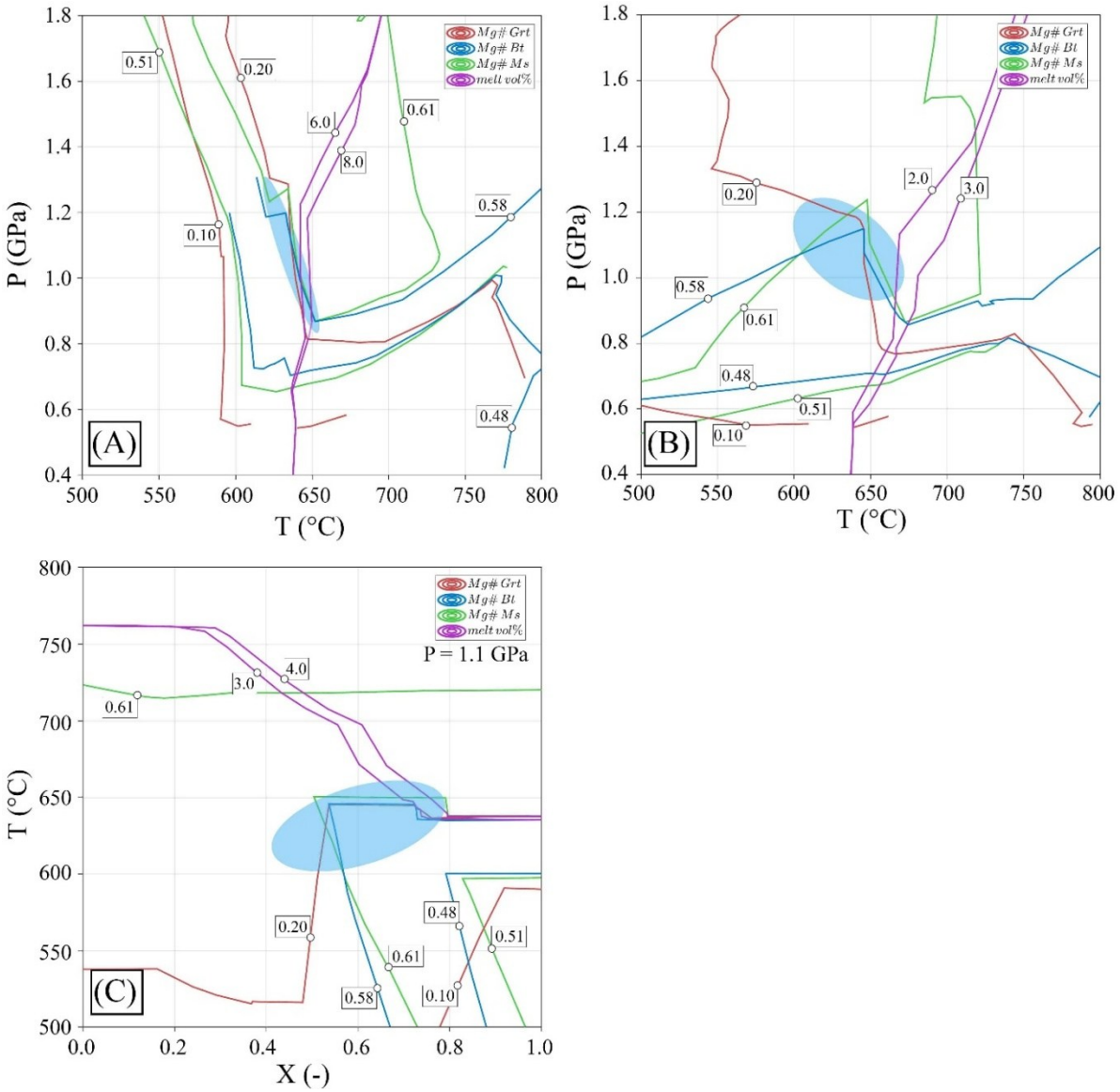

Figure S. 2.4: *P-T-X* estimates ($\pm 2\sigma$; blue ellipse) and the compositional contours used to infer the peak mineral assemblage (based on Figure 2.9 of the main text). The thermodynamic dataset of Holland and Powell (1998) was used. The ellipses were calculated using the average rim X_{Mg} of garnet (0.20), biotite (0.58), and muscovite (0.61) in a Monte Carlo approach. The magenta line represents melt content (vol%). (A) H_2O saturation: the ellipse is centered at around T:636°C and P:1.07 GPa. (B) H_2O undersaturation: the ellipse is centered at around T:634°C and P:1.09 GPa. (C) Variable water content (*T-X* section): the ellipse is centered at around T:631°C and X:0.60 (assuming P:1.1GPa).

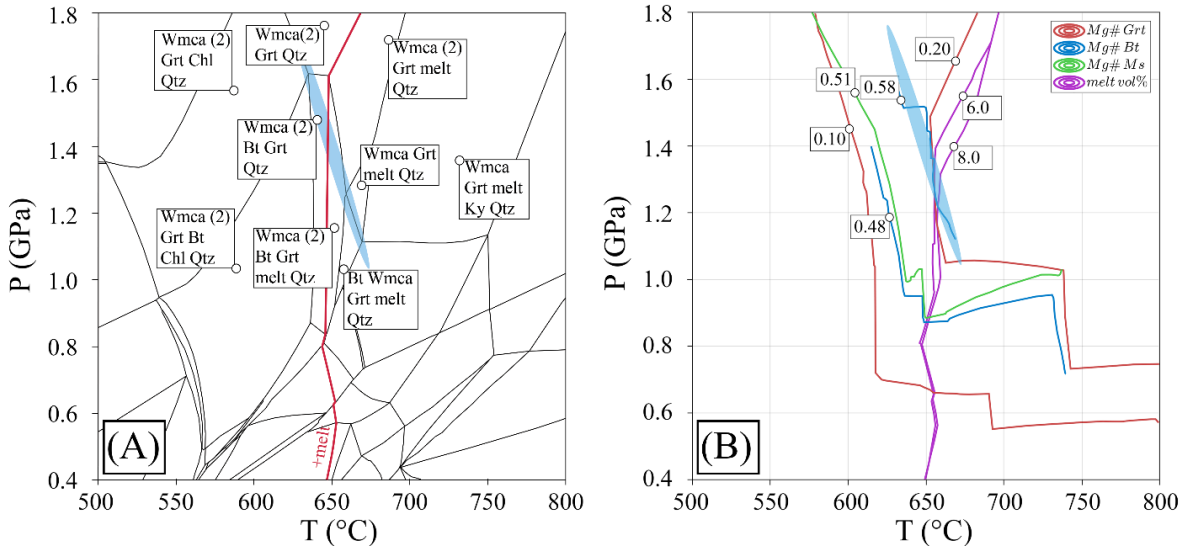

Figure S. 2.5: (A) Phase diagram *P-T* sections using the total bulk composition of the metapelite. The *P-T* estimate was calculated using the average rim X_{Mg} of garnet (0.20), biotite (0.58), and muscovite (0.61). (B) Compositional isopleths for the phase diagram in (A) and melt mode (in vol%) contours. Using the total bulk composition, we were not able to reproduce the X_{Mg} of muscovite (0.61). In particular, the X_{Mg} of muscovite increases to a maximum of 0.60 at high pressures. As a result, the fitting ellipse becomes more elongated, making it a less reliable constraint for pressure.

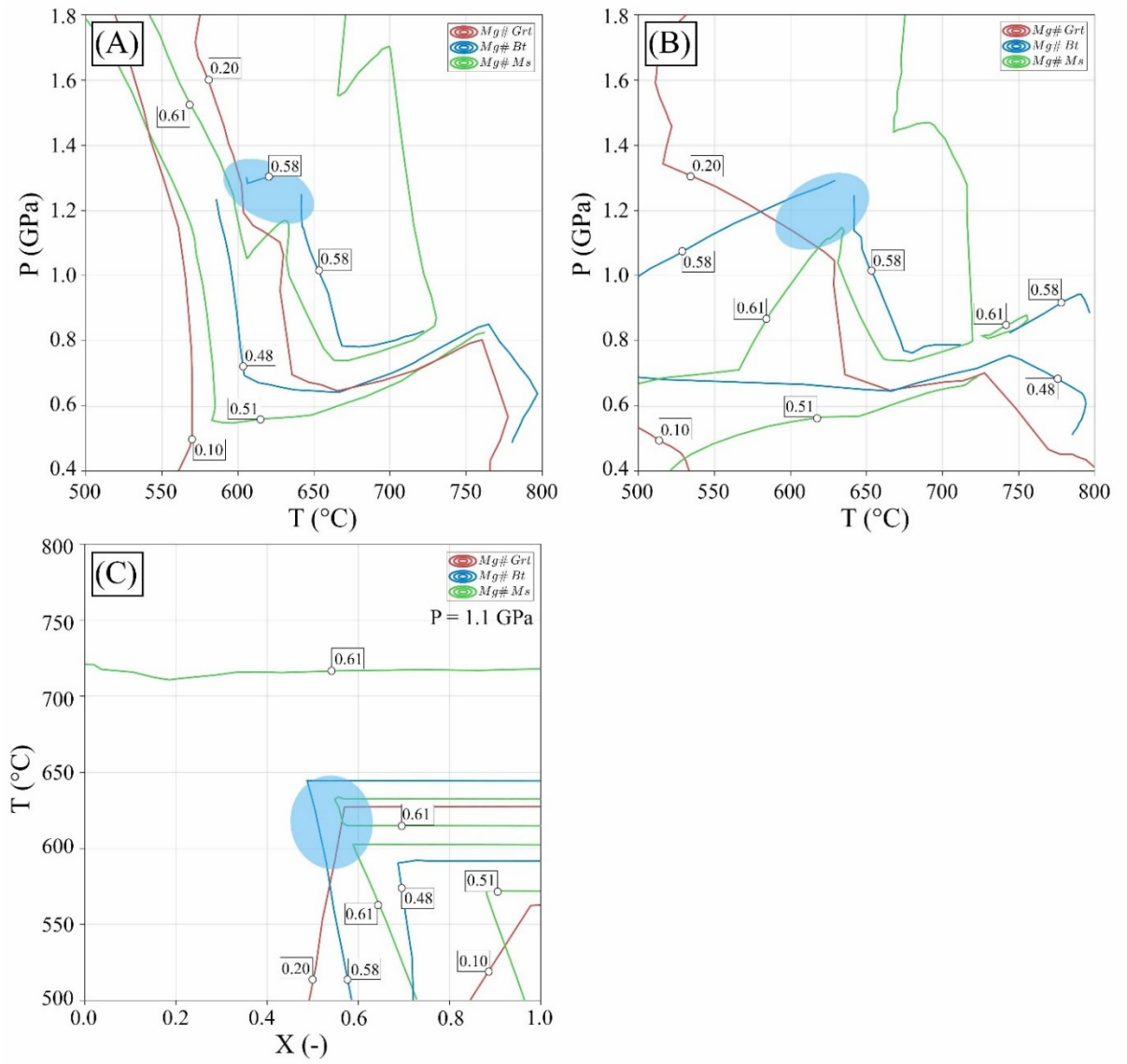

Figure S. 2.6: *P-T-X* estimates using the thermodynamic dataset of Holland and Powell (2011). The rim compositions were used as in the case of Figure S. 2.4. In this model, biotite is not stable beyond the solidus, and as a result, the inferred conditions are not in the melt-bearing field. (A) H_2O saturation: the ellipse is centered at around T:621°C and P:1.25 GPa. (B) H_2O undersaturation: the ellipse is centered at around T:621°C and P:1.19 GPa. (C) Variable water content (*T-X* section): the ellipse is centered at around T:617°C and X:0.54 (assuming P:1.1GPa).

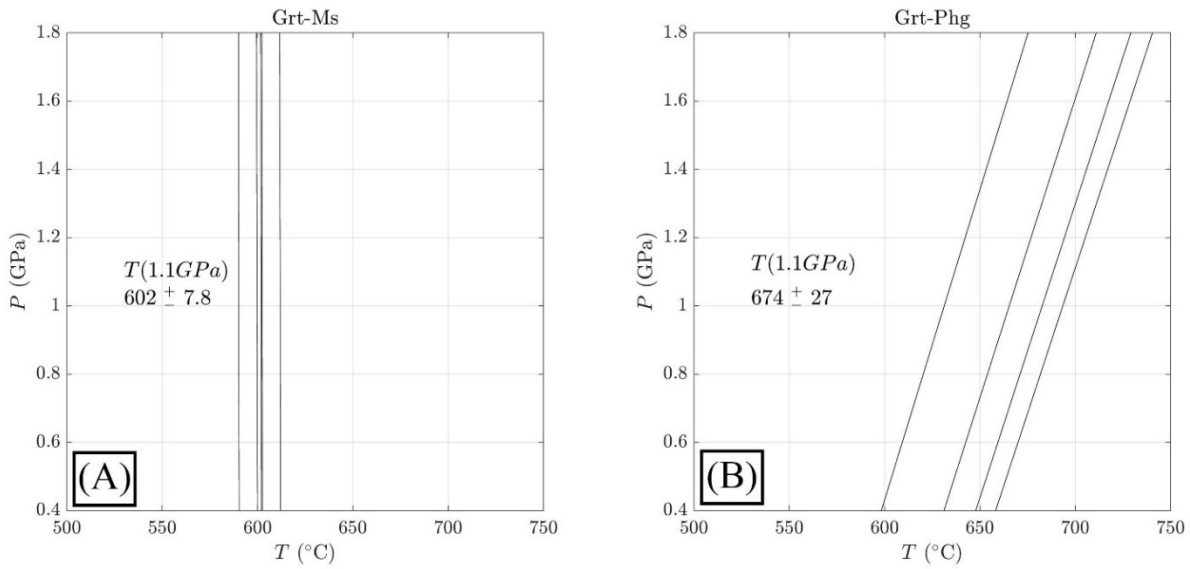

Figure S. 2.7: (A) Garnet-muscovite (Wu and Zhao, 2006) and (B) garnet-phengite (Green and Hellman, 1982) geothermometry. Both of the thermometers indicate temperatures in excess of 600°C (see main text for details).

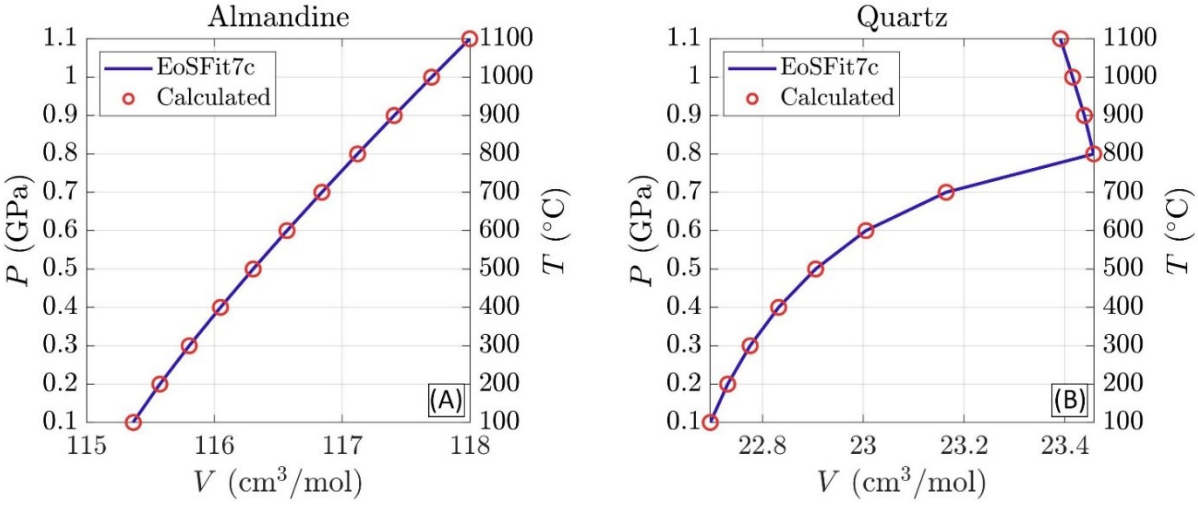

Figure S. 2.8: Benchmarking of the volumes for (A) almandine and (B) quartz calculated in this work using the Equations of State mentioned in the main text against the volumes calculated by EoSFit7c (Angel et al., 2014). The choice of P-T pairs is random. The kink in (B) corresponds to the transition from α-quartz to β-quartz.

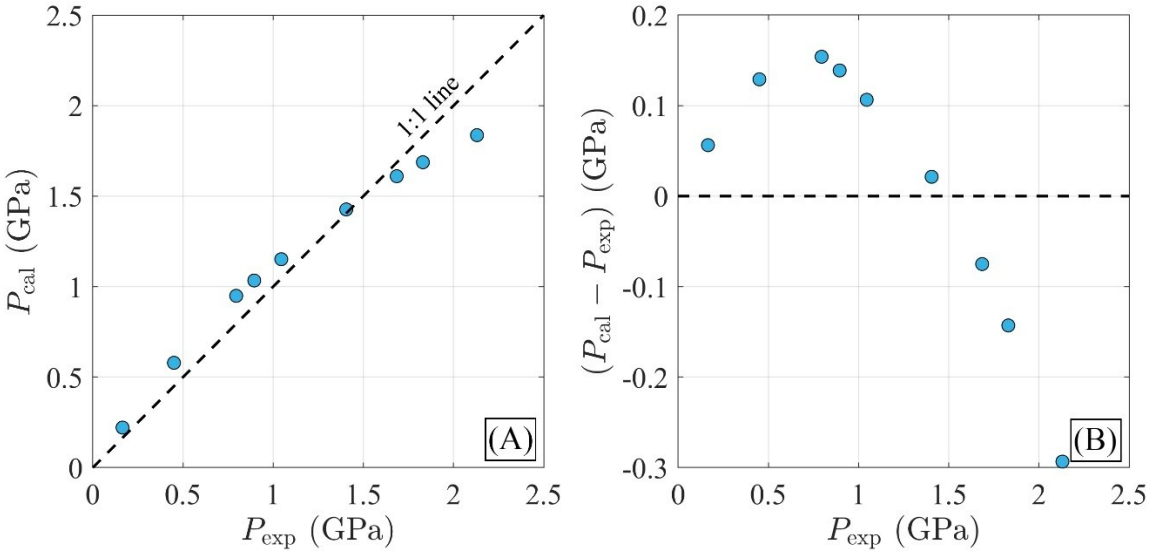

Figure S. 2.9: (A) Experimental pressure (P_{exp}) of Schmidt and Ziemann (2000) against pressure calculated for the same experiments based on the Grüneisen tensor (P_{cal}). The Grüneisen approach overestimates the pressure up to approximately 1.5GPa, but underestimates it beyond this point. (B) P_{exp} against (P_{cal} - P_{exp}) showing the deviations of pressure with the Grüneisen approach.

2.7.8 Supplementary Tables

Table S. 2.1: Total bulk rock major and trace element compositions of metapelite and amphibolite from the Pindos metamorphic sole.

Major (wt. %)	**SiO_2**	**TiO_2**	**Al_2O_3**	**FeO**	**MnO**	**MgO**	**CaO**	**Na_2O**	**K_2O**	**P_2O_5**	**Total**	**LOI**
Metapelite	62.30	0.753	19.42	7.32	0.397	2.24	0.43	1.08	3.38	0.092	97.43	2.38
Amphibolite	45.78	0.114	16.48	4.14	0.088	13.90	16.09	0.80	0.03	0.025	97.45	2.32
Trace (ppm)	**Ni**	**Cr**	**Sc**	**V**	**Ba**	**Rb**	**Sr**	**Zr**	**Y**	**Nb**	**Ga**	**Cu**
Metapelite	81	107	17	168	370	122	105	151	28	14.4	23	89
Amphibolite	399	1251	24	97	0	0	70	2	3	0	8	51
Trace (ppm)	**Zn**	**Pb**	**La**	**Ce**	**Th**	**Nd**	**U**					
Metapelite	87	34	37	89	12	32	1					
Amphibolite	26	0	0	0	0	0	0					

2.8 Data availability

The U-Pb, Ar-Ar and Raman datasets associated with this chapter are available in the corresponding publication in *Lithos* (https://doi.org/10.1016/j.lithos.2025.108285).

2.9 Acknowledgements

This work is dedicated to the memory of Anna Kantza, an awesome friend and field companion in the Pindos Mountains and the late Dr. Annie Rassios who always was an

inspiring figure and contributed greatly to the understanding of ophiolite belts in Greece and Albania.

2.10 Funding

The authors would like to acknowledge the German Research Foundation (DFG; project number 512790090) for support related to fieldwork and analytical expenses.

2.11 References

Agard, P., Yamato, P., Soret, M., Prigent, C., Guillot, S., Plunder, A., Dubacq, B., Chauvet, A., Monié, P., 2016. Plate interface rheological switches during subduction infancy: Control on slab penetration and metamorphic sole formation. Earth and Planetary Science Letters 451, 208–220.

Anders, B., Reischmann, T., Kostopoulos, D., 2007. Zircon geochronology of basement rocks from the Pelagonian Zone, Greece: Constraints on the pre-Alpine evolution of the westernmost Internal Hellenides. International Journal of Earth Sciences 96, 639–661.

Angel, R. J., Murri, M., Mihailova, B., Alvaro, M., 2019. Stress, strain and Raman shifts. Zeitschrift Für Kristallographie - Crystalline Materials 234, 129–140.

Angel, R. J., Nimis, P., Mazzucchelli, M. L., Alvaro, M., Nestola, F., 2015. How large are departures from lithostatic pressure? Constraints from host–inclusion elasticity. Journal of Metamorphic Geology 33, 801–813.

Blencoe, J. G., Guidotti, C. V., Sassi, F. P., 1994. The paragonite-muscovite solvus: II. Numerical geothermometers for natural, quasibinary paragonite-muscovite pairs. Geochimica et Cosmochimica Acta 58, 2277–2288.

Bonazzi, M., Tumiati, S., Thomas, J. B., Angel, R. J., Alvaro, M., 2019. Assessment of the reliability of elastic geobarometry with quartz inclusions. Lithos 350–351, 105201.

Boudier, F., Bouchez, J. L., Nicolas, A., Cannat, M., Ceuleneer, G., Misseri, M., Montigny, R., 1985. Kinematics of oceanic thrusting in the Oman ophiolite: Model of plate convergence. Earth and Planetary Science Letters 75, 215–222.

Burg, J.-P., Moulas, E., 2022. Cooling-rate constraints from metapelites across two inverted metamorphic sequences of the Alpine-Himalayan belt; evidence for viscous heating. Journal of Structural Geology 156, 104536.

Carrington, D. P., Watt, G. R., 1995. A geochemical and experimental study of the role of K-feldspar during water-undersaturated melting of metapelites. Chemical Geology 122, 59–76.

Cassata, W. S., Renne, P. R., Shuster, D. L., 2009. Argon diffusion in plagioclase and implications for thermochronometry: A case study from the Bushveld Complex, South Africa. Geochimica et Cosmochimica Acta 73, 6600–6612.

Clemens, J. D., 1984. Water contents of silicic to intermediate magmas. Lithos 17, 273–287.

Coggon, R., Holland, T.J.B., 2002. Mixing properties of phengitic micas and revised garnet-phengite thermobarometers. Journal of Metamorphic Geology 20, 683-696.

Connolly, J. A. D., 2009. The geodynamic equation of state: What and how. Geochemistry, Geophysics, Geosystems 10, Q10014.

Dewey, J. F., 1976. Ophiolite obduction. Tectonophysics 31, 93–120.

Dimo-Lahitte, A., Monié, P., Vergély, P., 2001. Metamorphic soles from the Albanian ophiolites: Petrology, 40Ar/39Ar geochronology, and geodynamic evolution. Tectonics 20, 78–96.

Duretz, T., Agard, P., Yamato, P., Ducassou, C., Burov, E. B., Gerya, T. V., 2016. Gondwana Research 32, 1–10.

Enami, M., Nishiyama, T., Mouri, T., 2007. Laser Raman microspectrometry of metamorphic quartz: A simple method for comparison of metamorphic pressures. American Mineralogist 92, 1303–1315.

Ferrière, J., Chanier, F., Reynaud, J.-Y., Pavlopoulos, A., Ditbanjong, P., Coutand, I., 2013. Evolution of the Mesohellenic Basin (Greece): A synthesis. Journal of the Virtual Explorer 45, 1–51.

Fukuda, J., Okudaira, T., Satsukawa, T., Michibayashi, K., 2012. Solution–precipitation of K-feldspar in deformed granitoids and its relationship to the distribution of water. Tectonophysics 532–535, 175–185.

Garber, J. M., Rioux, M., Smye, A. J., Cruz-Uribe, A. M., Baker, P. L., Vervoort, J. D., Searle, M. P., Feineman, M. D., 2025. Shear heating during rapid subduction initiation beneah the Samail Ophiolite. Nature Geoscience 18, 653-660.

Gartzos, E., Dietrich, V. J., Migiros, G., Serelis, K., Lymperopoulou, T., 2009. The origin of amphibolites from metamorphic soles beneath the ultramafic ophiolites in Evia and Lesvos (Greece) and their geotectonic implication. Lithos 108, 224–242.

Ghikas, C., Dilek, Y., Rassios, A. E., 2010. Structure and tectonics of subophiolitic mélanges in the western Hellenides (Greece): Implications for ophiolite emplacement tectonics. International Geology Review 52, 423–453.

Green, E. C. R., White, R. W., Diener, J. F. A., Powell, R., Holland, T. J. B., Palin, R. M., 2016. Activity–composition relations for the calculation of partial melting equilibria in metabasic rocks. Journal of Metamorphic Geology 34, 845–869.

Green, T. H., Hellman, P. L., 1982. Fe-Mg partitioning between coexisting garnet and phengite te at high pressure, and comments on a garnet-phengite geothermometer. Lithos 15, 253–266.

Griera, A., Llorens, M.-G., Gomez-Rivas, E., Bons, P. D., Jessell, M. W., Evans, L. A., Lebensohn, R., 2013. Numerical modelling of porphyroclast and porphyroblast rotation in anisotropic rocks. Deformation, Pophyroblasts and Mountain Building: A Special Issue in Honor of the Career Contributions of T.H. Bell 587, 4–29.

Hacker, B. R., Mosenfelder, J. L., Gnos, E., 1996. Rapid emplacement of the Oman ophiolite: Thermal and geochronologic constraints. Tectonics 15, 1230–1247.

Harrison, T. M., 1982. Diffusion of 40Ar in hornblende. Contributions to Mineralogy and Petrology 78, 324–331.

Harrison, T. M., Célérier, J., Aikman, A. B., Hermann, J., Heizler, M. T., 2009. Diffusion of 40Ar in muscovite. Geochimica et Cosmochimica Acta 73, 1039–1051.

Hawthorne, F. C., Oberti, R., Harlow, G. E., Maresch, W. V., Martin, R. F., Schumacher, J. C., Welch, M. D., 2012. Nomenclature of the amphibole supergroup. American Mineralogist 97, 2031–2048.

Hodges, K. V., Spear, F. S., 1982. Geothermometry, geobarometry and the Al2SiO5 triple point at Mt. Moosilauke, New Hampshire. American Mineralogist 67, 1118–1134.

Holland, T. J. B., Powell, R., 1998. An internally consistent thermodynamic data set for phases of petrological interest. Journal of Metamorphic Geology 16, 309–343.

Holland, T. J. B., Powell, R., 2011. An improved and extended internally consistent thermodynamic dataset for phases of petrological interest, involving a new equation of state for solids. Journal of Metamorphic Geology 29, 333–383.

Hunziker, D., Burg, J. -P., Moulas, E., Reusser, E., Omrani, J., 2017. Formation and preservation of fresh lawsonite: Geothermobarometry of the North Makran Blueschists, southeast Iran. Journal of Metamorphic Geology 35, 871–895.

Ibragimov, I., Kiss, D., Moulas, E., 2024. A thermo-mechanical model of the thermal evolution and incorporation of metamorphic soles in Tethyan ophiolites: a case study from Oman. Austrian Journal of Earth Sciences 117, 13-24.

Jones, G., De Wever, P., Robertson, A.H.F., 1992. Significance of radiolarian age data to the Mesozoic tectonic and sedimentary evolution of the northern Pindos Mountains, Greece. Geological Magazine 129, 385–400.

Jones, G., Robertson, A.H.F., 1991. Tectono-stratigraphy and evolution of the Mesozoic Pindos ophiolite and related units, northwestern Greece. Journal of the Geological Society 148, 267.

Jourdan, F., 2012. The $^{40}Ar/^{39}Ar$ dating technique applied to planetary sciences and terrestrial impacts. Australian Journal of Earth Sciences 59, 199–224.

Kaneko, Y., Miyano, T., 2004. Recalibration of mutually consistent garnet–biotite and garnet–cordierite geothermometers. Lithos 73, 255–269.

Kemp, A. E. S., McCaig, A. M., 1984. Origins and significance of rocks in an imbricate thrust zone beneath the Pindos ophiolite, northwestern Greece. Geological Society, London, Special Publications 17, 569–580.

Kiss, D., Podladchikov, Y., Duretz, T., Schmalholz, S. M., 2019. Spontaneous generation of ductile shear zones by thermal softening: Localization criterion, 1D to 3D modelling and application to the lithosphere. Earth and Planetary Science Letters 519, 284-296.

Kleemann, U., Reinhardt, J., 1994. Garnet-biotite thermometry revisited: The effect of AlVI and Ti in biotite. European Journal of Mineralogy 6, 925–942.

Kostopoulos, D. K., 1989. Geochemistry, Petrogenesis and Tectonic Setting of the Pindos ophiolite, NW Greece. Newcastle upon Tyne.

Liati, A., Gebauer, D., Fanning, C. M., 2004. The age of ophiolitic rocks of the Hellenides (Vourinos, Pindos, Crete): First U–Pb ion microprobe (SHRIMP) zircon ages. Chemical Geology 207, 171–188.

Locock, A. J., 2014. An Excel spreadsheet to classify chemical analyses of amphiboles following the IMA 2012 recommendations. Computers and Geosciences 62, 1–11.

Maffione, M., Van Hinsbergen, D. J. J., 2018. Reconstructing Plate Boundaries in the Jurassic Neo-Tethys From the East and West Vardar Ophiolites (Greece and Serbia). Tectonics 37, 858–887.

Millonig, L. J., Albert, R., Gerdes, A., Avigad, D., Dietsch, C., 2020. Exploring laser ablation U–Pb dating of regional metamorphic garnet – The Straits Schist, Connecticut, USA. Earth and Planetary Science Letters 552, 116589.

Moulas, E., Kostopoulos, D., Podladchikov, Y., Chatzitheodoridis, E., Schenker, F. L., Zingerman, K. M., Pomonis, P., Tajčmanová, L., 2020. Calculating pressure with elastic geobarometry: A comparison of different elastic solutions with application to a

calc-silicate gneiss from the Rhodope Metamorphic Province. Lithos 378–379, 105803.

Moulas, E., Podladchikov, Y., Zingerman, K., Vershinin, A., Levin, V., 2023. Large-strain Elastic and Elasto-Plastic Formulations for Host-Inclusion Systems and Their Applications in Thermobarometry and Geodynamics. American Journal of Science 323, 2.

Myhill, R., 2011. Constraints on the evolution of the Mesohellenic Ophiolite from subophiolitic metamorphic rocks. Geological Society of America Special Papers 480, 75–94.

Nerone, S., Lanari, P., Dominguez, H., Forshaw, J.B., Groppo, C., Rolfo, F., 2025. IntersecT: a Python script for quantitative isopleth thermobarometry of equilibrium and disequilibrium systems. Computers and Geosciences 202, 105949.

Palandzhyan, S. A., Layer, P. W., Patton, W. W., Khanchuk, A. I., 2011. Geodynamic interpretation of the 40Ar/39Ar dating of ophiolitic and arc-related mafics and metamafics of the northern part of the Anadyr-Koryak region. Geotectonics, 45, 481–495.

Parlak, O., Delaloye, M., 1999. Precise 40Ar/39Ar ages from the metamorphic sole of the Mersin ophiolite (southern Turkey). Tectonophysics 301, 145–158.

Parlak, O., Dunkl, I., Karaoğlan, F., Kusky, T. M., Zhang, C., Wang, L., Koepke, J., Billor, Z., Hames, W. E., Şimşek, E., Şimşek, G., Şimşek, T., Öztürk, S. E., 2019. Rapid cooling history of a Neotethyan ophiolite: Evidence for contemporaneous subduction initiation and metamorphic sole formation. Geological Society of America Bulletin 131, 2011–2038.

Peillod, A., Patten, C. G. C., Drüppel, K., Beranoaguirre, A., Zeh, A., Gudelius, D., Hector, S., Majka, J., Kleine-Marshall, B. I., Karlson, A., Gerdes, A., Kolb, J., 2024. Disruption of a high-pressure unit during exhumation: Example of the Cycladic Blueschist unit (Thera, Ios and Naxos islands, Greece). Journal of Metamorphic Geology 42, 225–255.

Pomonis, P., Tsikouras, B., Hatzipanagiotou, K., 2002. Origin, evolution and radiometric dating of subophiolitic metamorphic rocks from the Koziakas ophiolite (W. Thessaly, Greece). Neues Jahrbuch Für Mineralogie, Abhandlungen 177, 255–276.

Rassios, A., Dilek, Y., 2009. Rotational deformation in the Jurassic Mesohellenic ophiolites, Greece, and its tectonic significance. Lithos 108, 207–223.

Rassios, A., Smith, A. G., Kostopoulos, D. K., 2009. Ophiolites 2008 guidebook: Link between the Mesohellenic Ophiolites and Pelagonian Margin. Journal of the Virtual Explorer 34.

Rassios, A., Moores, E. M., 2006. Heterogeneous mantle complex, crustal processes, and obduction kinematics in a unified Pindos-Vourinos ophiolitic slab (northern Greece). Geological Society, London, Special Publications 260, 237–266.

Robertson, A., 2004. Development of concepts concerning the genesis and emplacement of Tethyan ophiolites in the Eastern Mediterranean and Oman regions. Earth-Science Reviews 66, 331–387.

Robertson, A. H. F., Clift, P. D., Degnan, P. J., Jones, G., 1991. Palaeogeographic and palaeotectonic evolution of the Eastern Mediterranean Neotethys. Palaeogeography, Palaeoclimatology, Palaeoecology 87, 289–343.

Schaen, A. J., Jicha, B. R., Hodges, K. V., Vermeesch, P., Stelten, M. E., Mercer, C. M., Phillips, D., Rivera, T. A., Jourdan, F., Matchan, E. L., Hemming, S. R., Morgan, L. E., Kelley, S. P., Cassata, W. S., Heizler, M. T., Vasconcelos, P. M., Benowitz, J. A., Koppers, A. A. P., Mark, D. F., Singer, B. S., 2021. Interpreting and reporting 40Ar/39Ar geochronologic data. Geological Society of America Bulletin, 133, 461–487.

Sergeev, D. S., Dijkstra, A. H., Meisel, T., Brügmann, G., Sergeev, S. A., 2014. Traces of ancient mafic layers in the Tethys oceanic mantle. Earth and Planetary Science Letters 389, 155–166.

Siivola, J., Schmid, R., 2007. Recommendations by the IUGS Subcommission on the Systematics of Metamorphic Rocks: List of mineral abbreviations.

Smith, A. G., 1993. Tectonic significance of the Hellenic-Dinaric ophiolites. Geological Society, London, Special Publications 76, 213–243.

Smith, A. G., Spray, J. G., 1984. A half-ridge transform model for the Hellenic-Dinaric ophiolites. Geological Society, London, Special Publications 17, 629–644.

Smith, A. G., Woodcock, N. H., Naylor, M. A., 1979. The structural evolution of a Mesozoic continental margin, Othris Mountains, Greece. Journal of the Geological Society 136, 589–601.

Spear, F. S., Wolfe, O. M., 2020. Revaluation of “equilibrium” P-T paths from zoned garnet in light of quartz inclusion in garnet (QuiG) barometry. Lithos 372–373, 105650.

Spray, J. G., 1984. Possible causes and consequences of upper mantle decoupling and ophiolite displacement. Geological Society, London, Special Publications 13, 255.

Spray, J. G., Bébien, J., Rex, D. C., Roddick, J. C., 1984. Age constraints on the igneous and metamorphic evolution of the Hellenic-Dinaric ophiolites. Geological Society, London, Special Publications 17, 619.

Stampfli, G. M., Hochard, C., Vérard, C., Wilhem, C., von Raumer, J., 2013. The formation of Pangea. Tectonophysics 593, 1–19.

Tinkham, D. K., Zuluaga, C. A., and Stowell, H. H., 2001. Metapelite phase equilibria modeling in MnNCKFMASH: The effect of variable Al2O3 and MgO/(MgO+FeO) on mineral stability. Geological Materials Research 3, 1–42.

Walters, J.B., Garber, J.M., Beranoaguirre, A., Millonig, L., Gerdes, A., Grützner, T., Marschall, H.R., 2025. Zircon micro-inclusions as an obstacle for in situ garnet U-Pb geochronology: An example from the As Sifah eclogite locality, Oman. EGUsphere, preprint

Weinberg, R. F., Hasalová, P., 2015. Water-fluxed melting of the continental crust: A review. Lithos 212–215, 158–188.

Wijbrans, J. R., McDougall, I., 1988. Metamorphic evolution of the Attic Cycladic Metamorphic Belt on Naxos (Cyclades, Greece) utilizing $^{40}Ar/^{39}Ar$ age spectrum measurements. Journal of Metamorphic Geology 6, 571–594.

Williams, H., Smyth, W. R., 1973. Metamorphic aureoles beneath ophiolite suites and alpine peridotites; tectonic implications with west Newfoundland examples. American Journal of Science 273, 594–621.

Wu, C.-M., Zhao, G., 2006. Recalibration of the Garnet–Muscovite (GM) Geothermometer and the Garnet–Muscovite–Plagioclase–Quartz (GMPQ) Geobarometer for Metapelitic Assemblages. Journal of Petrology 47, 2357–2368.

Zhong, X., Moulas, E., Tajčmanová, L., 2020. Post-entrapment modification of residual inclusion pressure and its implications for Raman elastic thermobarometry. Solid Earth 11, 223–240.

Zhong, X., Wallis, D., Kingsbery, P., John, T., 2024. The effect of aqueous fluid on viscous relaxation of garnet and modification of inclusion pressures after entrapment. Earth and Planetary Science Letters 636, 118713.

Chapter 3: Hamiltonian Monte Carlo applied to inverse petrological problems

This chapter has been uploaded as a preprint in EarthArXiv and has been submitted to the American Journal of Science:

Moutzouris D., Stroh A., Schorn S., Moulas E. (2026). Hamiltonian Monte Carlo applied to inverse petrological problems. EarthArXiv, https://doi.org/10.31223/X58V0H.

Author contribution

The author of this dissertation prepared the original manuscript, developed the theoretical framework underlying Hamiltonian Monte Carlo, implemented the primary codes for inversion and Hamiltonian Monte Carlo, designed the figures and performed the calculations, data analysis and interpretation of the results.

Abstract

Inversion is inherent in petrology and is used to investigate both experimental and natural field data. When field observations, petrography, geochronology and geochemistry are combined with numerical models, inversion is used to quantify important parameters that provide insights into natural processes involved in the petrogenesis of rocks. Additionally, with the current advances in the field of petrology, a large number of parameters can be explored. However, an increase in the number of parameters also raises the overall computational cost. Therefore, appropriate algorithms are needed to efficiently explore such high-dimensional parameter spaces. In this contribution, we demonstrate the use of Hamiltonian Monte Carlo for inverse diffusion modeling within a petrological framework. We begin by describing the theoretical background of the approach. We show that Hamiltonian Monte Carlo is a powerful tool to explore high-dimensional parameter spaces and therefore quantify the uncertainties of key parameters in petrological forward models. By using compositional garnet data and geochronological Ar-muscovite data from the Pindos metamorphic sole as an example, we invert for the initial cooling rate, initial equilibration temperature and the effective grain size of the investigated minerals. A key finding in our work is the strong agreement between inverse garnet diffusion modeling and Ar diffusion in muscovite, even though the two approaches are entirely independent. Our joint approach shows that an initial equilibration temperature of 637.6 ± 8.3 °C and an initial cooling rate of 241.3 ± 76.5 °C/Myr is required to explain not only previous thermobarometric and geochronological data but also the major-element zonation of garnets and the $^{40}Ar/^{39}Ar$ age of muscovite from the Pindos metamorphic sole. Moreover, our inversion showed that the effective grain size of muscovite plays a negligible role in fitting the observed $^{40}Ar/^{39}Ar$ age of the mineral. The calculated cooling rates and the preservation of high equilibration temperatures, garnet zonation and residual quartz-in-garnet pressures strongly support shear heating as the primary mechanism for the formation of the Pindos metamorphic sole.

3.1 Introduction

Igneous and metamorphic rocks represent the final state of complex physical and chemical processes, recording integrated pressure–temperature–time (*P–T–t*) histories. Throughout their evolution, rocks undergo coupled textural, mineralogical, mechanical, and compositional changes that collectively encode the processes operating during their formation and subsequent modification. Since the advancement of analytical and computational techniques, the evolution of rocks can be quantified with the use of thermodynamic and numerical models. As an example, inverse diffusion models have been widely applied to reproduce the compositional profiles of minerals in a diverse range of systems, spanning from meteorites to magmatic and metamorphic rocks (e.g., Costa et al., 2020; Kent et al., 2001; Medaris et al., 1990; Olker et al., 2003). For rocks that (re)crystallize at elevated temperatures, mineral compositional profiles evolve in a time-dependent manner as a result of active intracrystalline diffusion. As temperatures decrease toward near-surface conditions, chemical diffusivities in most silicate minerals become negligibly small (e.g., Zhang, 2010). Consequently, the compositional profiles preserved in minerals effectively record the duration of high-temperature geological processes and can be used to quantify and constrain their timescales (Faryad & Chakraborty, 2005; Lasaga, 1983; Schorn et al., 2024; Schwarzenbach et al., 2021). Interpreting such profiles therefore constitutes an inverse problem, in which observed present-day compositions are used to reconstruct the underlying thermal and temporal evolution (e.g., Engl et al., 1996). Alternatively to the temporal estimates, numerical diffusion models can be used to quantify key parameters such as the effective cooling rate (e.g., Burg & Moulas, 2022; Lasaga et al., 1977; Spear, 2004). The estimated cooling rates may be used to understand the geodynamic processes involved in the evolution of a rock. Whether time spent at high temperatures or effective cooling rate is estimated, the main objective of inverse diffusion modelling is to quantify petrologically useful parameters that best reproduce the observed natural data while satisfying given constraints (e.g., estimated *P–T* conditions) and physical models.

Petrological inversion becomes more complex in the absence of well-defined constraints. For instance, in the context of diffusion modeling, if the initial peak metamorphic conditions are unknown, infinite combinations of initial temperature and cooling rate yield indistinguishable good fits to the observed compositional data. The implication of this is that as many combinations result in the identical compositional profile preserved in compositionally zoned minerals. In fact, the choice of constraining the timescale (also known as diffusion chronometry) or the cooling rate (diffusion geospeedometry) from the same compositional data

testifies to the fact that different thermal histories may yield equally satisfying results. This lack of uniqueness makes inverse diffusion-type models ill-posed by definition (e.g., Kabanikhin, 2008).

Another source of uncertainty in inversion modelling stems from the inherent susceptibility of petrological data to analytical and random errors, commonly related to measurement methodologies such as electron microprobe analysis (EPMA; e.g., Batanova et al., 2018). This means that repeated measurements will inevitably yield different observations. Therefore, a range of models may be considered as consistent (within error) with the observed data (Figure 3.1A). Consequently, the inverted parameters derived from this set of models also inherit uncertainties reflecting the variability of the data (Figure 3.1B). Various approaches exist to quantify the uncertainty of the invertible parameters, each showing distinct advantages and limitations.

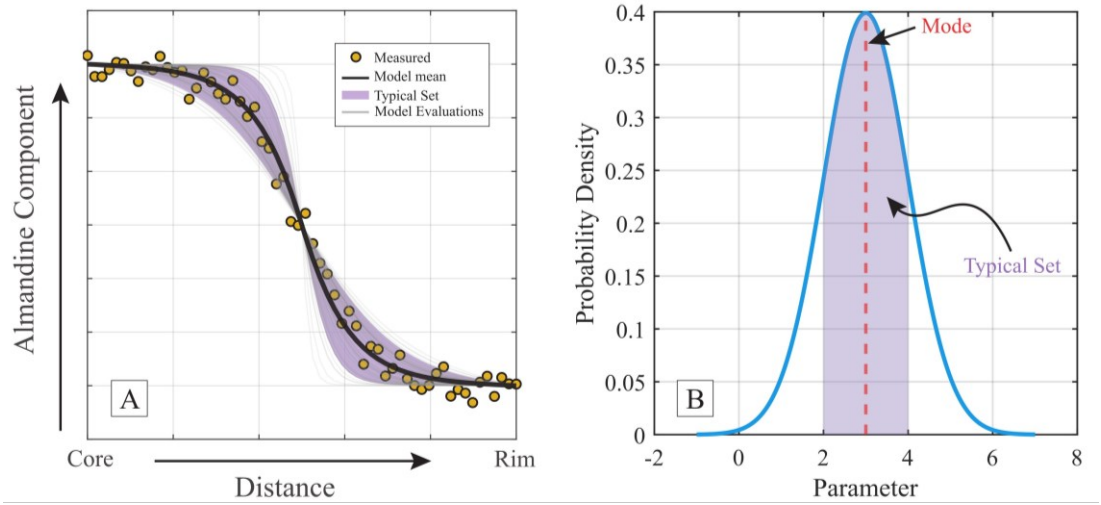

Figure 3.1: Conceptual illustration highlighting the primary goal of inverse diffusion modelling in garnet (e.g., almandine component). (A) A large number of models (grey lines) is evaluated using different values of a physical parameter (e.g., as cooling rate). Only some of these models successfully reproduce the observed compositional data within their uncertainty. The parameter values associated with these successful models form the *typical set*. That is the range of parameter values that is the most consistent with the data. (B) The parameter can be represented by a probability distribution, such as a normal (Gaussian) distribution. In this distribution, the *typical set* corresponds to the high-probability region with the highest probability of reproducing the observations. The single value with the highest probability is the *mode*. The primary objective of inversion is to identify and quantify this *typical set* of parameter values.

An important aspect of inversion is the number of parameters involved. In simple cases with one to two variable parameters, a direct search algorithm that scans the full parameter range can adequately explore the parameter space with reasonable computational cost (e.g., Burg & Moulas, 2022). As numerical models continue to develop and incorporate greater physical complexity, the number of parameters that can be explored through inversion drastically increases (e.g., Mackay-Champion & Cawood, 2025). This leads to a substantial rise in computational cost. Consequently, more advanced algorithms are required to efficiently explore high-dimensional parameter spaces and at the same time enable rigorous quantification of the associated uncertainties.

Here we apply the Hamiltonian Monte Carlo (HMC) method to inverse diffusion petrological/geochemical modeling to explore the parameter space and quantify uncertainties of critical parameters such as the cooling rate, the initial equilibration temperature and the effective mineral grain size in the case of muscovite Ar diffusion. Unlike other sampling techniques, HMC is a gradient-based method that offers significant advantages particularly in its ability to efficiently handle high-dimensional parameter spaces. To test HMC, we used petrological data from the metamorphic sole rocks of the Pindos ophiolite in northwestern Greece (Moutzouris et al., 2025). These rocks are well-suited for this method due to the relative simplicity of their P-T evolution and the consistency of results. Our previous findings show that the rocks underwent rapid cooling under relatively high temperatures (Moutzouris et al., 2025). The joint inversion presented in this paper utilizes two different forward problems of petrological interest. The first forward problem is the diffusion of major elements in garnet and the second is the diffusion of radiogenic argon in muscovite. The incorporation of the data relevant to two different petrological datasets –garnet and muscovite– suggests that both datasets can be explained if the sole rocks experienced very high values of initial (and transient) cooling rates (241.3 ± 76.5 °C/Myr). The latter results are in agreement with a geodynamic scenario that requires the fast tectonic movement of the sole rocks with contributions from shear heating (Tagliaferri et al., 2025). Our results show that the integration of multiple independent physical models in combination with petrological constraints and rigorous uncertainty quantification provides improved insights into the geodynamic processes involved.

3.2 Hamiltonian Monte Carlo

The HMC algorithm is a variant of the Markov Chain Monte Carlo (MCMC) class of algorithms. MCMC originates from the pioneering work of Metropolis et al. (1953), who used it to study equations of state of interacting molecules. HMC, initially termed Hybrid Monte

Carlo, was first introduced by Duane et al. (1987) in the context of molecular dynamics simulations. Since then, and aided by advances in computational power, HMC has been successfully applied to a wide range of statistical and physical problems (e.g., Hajian, 2007; Mehlig et al., 1992; Neal, 1996). Within the geosciences, Sen & Biswas (2017) were amongst the first to apply HMC to seismic inversion. A comparative study by Reuber (2021), along with the contributions of Fichtner & Zunino (2019) and Fichtner et al. (2021), have demonstrated the potential of HMC methods for addressing geoscientific inversion-type problems. Since then, HMC has been predominantly employed in geophysical inversion (e.g., De Lima et al., 2024; Gebraad et al., 2020; Koch et al., 2020; Y. Xu et al., 2025; Zunino et al., 2022), while petrological applications are still missing. Here we aim at addressing this shortcoming by first outlining the fundamental concepts underlying HMC, followed by a practical petrological application to the Pindos metamorphic sole (northern Greece; Moutzouris et al., 2025) showcasing the capabilities of this method. Finally, we conclude this contribution with some potential implications on the geodynamic evolution of the studied rocks.

Starting from petrologic observations, we can infer geodynamic processes once certain physical parameters, such as the peak temperature and the initial cooling rate, are constrained. These parameters define a space that must be explored to determine which parameter combinations provide adequate data fits. A satisfactory data fit means that the modeled output matches the observed data within their uncertainty. The region in the parameter space resulting in such fits is referred to as the *typical set* (Figure 3.1B and Figure 3.2A). Within the *typical set* lies the *mode*, which corresponds to the parameter values with the highest probability of generating the observed data. For example, in a one-dimensional Gaussian distribution, the *mode* is located at the peak of the probability curve (Figure 3.1B). However, a comprehensive understanding of the parameter space requires examining not only the *mode* but also its surrounding neighborhood, where probabilities remain high and most of the probability mass is concentrated. A typical petrological example of such high probabilities is the numerous combinations of cooling rates and near-peak temperatures that can be used to fit the same diffusion data (Burg & Moulas, 2022; Tagliaferri et al., 2025). With increasing number of invertible parameters, the *typical set* exploration becomes computationally challenging and efficient algorithms are required to explore it.

The HMC method is based on the concept of Hamiltonian energy from classical mechanics (e.g., Arnold, 1974) and it is used by analogy in inverse problems. In classical mechanics, the Hamiltonian energy is used to describe the evolution of a system of particles by updating their

position and momentum over time. The positions and momenta of the system's parts are also called the "canonical variables", and they define a space known as the *phase space*. Thus, the evolution of a mechanical system can be represented as a trajectory in phase space. The mechanical system under investigation could be something as simple as a harmonic oscillator such as a pendulum or a more complex mechanical configuration. One of the advantages of the Hamiltonian approach lies in the fact that the evolution of a physical system is described using a set of ordinary differential equations for position and momentum. Therefore, once a physical system evolves in time, its position and momentum mark a trajectory in phase space (Figure 3.2). If the evolution of a system is known within a certain region of the phase space, then, we have mapped out all the possible states of the mechanical system.

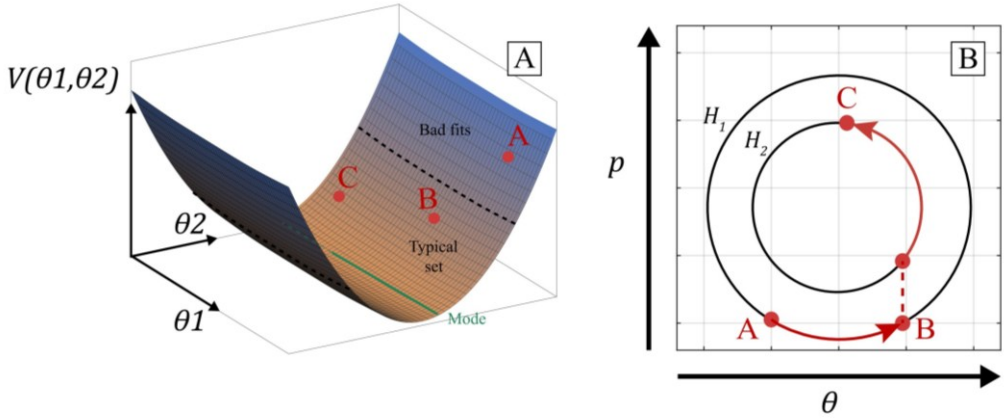

Figure 3.2: Simplified illustration showing the main concept of Hamiltonian Monte Carlo. (A) Schematic plot showing the misfit function $V(\theta_1, \theta_2)$, that in this case defines a valley for two invertible parameters θ_1 and θ_2. The slopes of the valley correspond to regions of bad fits between model and data. The valley floor represents the *mode* (best-fit region) of this two-dimensional space. The main goal of Hamiltonian Monte Carlo is to propose new samples that possibly start from the slopes but eventually explore the *typical set*. This corresponds to going from point A to points B and C (see main text for more details). (B) The exploration is achieved by updating the parameters ($\boldsymbol{\theta}$) and their corresponding momenta ($\boldsymbol{p}$) along trajectories of constant Hamiltonian energy (H_1, H_2).

In inverse models having several parameters, the challenge is to efficiently sample the parameter space that contains all possible states of the system. In this regard, by "states" we define the possible sets of parameters that provide adequate fits to our dataset. By analogy to true Hamiltonian mechanics, HMC treats model parameters as position variables (θ_1, θ_2 ...) within the *phase space*, and the misfit function –which defines the goodness-of-fit between

model and observable data– is treated as analogous to the potential energy $V(\theta_1, \theta_2 \ldots)$. As such, minima in the misfit function correspond to the optimal set of parameters – those that lead to the best fit of the input data. Artificial momenta are then introduced instead of real physical momenta that aid to the exploration of the parameter space. Note that the usage of artificial momenta does not affect the inversion results and is only introduced to optimize the computation in a self-consistent manner. For a detailed discussion of the HMC method, the reader is referred to Neal (2011) and Betancourt (2018).

In the framework of HMC, the Hamiltonian energy is defined as the sum of a potential and a kinetic energy:

$$H(\boldsymbol{\theta}, \boldsymbol{p}) = T(\boldsymbol{p}) + V(\boldsymbol{\theta}) \tag{3.1}$$

where $\boldsymbol{\theta}$ represents the vector of invertible parameters of interest, $\boldsymbol{p}$ stands for the vector of the artificial momenta, $H(\boldsymbol{\theta}, \boldsymbol{p})$ is the Hamiltonian energy, $T(\boldsymbol{p})$ is the kinetic energy as function of the momentum vector $\boldsymbol{p}$ and $V(\boldsymbol{\theta})$ is the potential energy function of the parameter vector $\boldsymbol{\theta}$. $H(\boldsymbol{\theta}, \boldsymbol{p})$ quantifies the total amount of energy of a system at given coordinates ($\boldsymbol{\theta}$) and momenta ($\boldsymbol{p}$). For an intuitive analogy, $\boldsymbol{\theta}$ can be thought as the position of a harmonic oscillator and $\boldsymbol{p}$ as its momentum. In this paper, $\boldsymbol{\theta}$ will represent the vector of invertible parameters (e.g., cooling rate and initial equilibration temperature) and $\boldsymbol{p}$ their corresponding artificial momenta. The motion of a Hamiltonian system can be calculated with the *canonical equations* defined as:

$$\frac{d\theta_i}{dt} = \frac{\partial H(\boldsymbol{\theta}, \boldsymbol{p})}{\partial p_i} \tag{3.2}$$

$$\frac{dp_i}{dt} = -\frac{\partial H(\boldsymbol{\theta}, \boldsymbol{p})}{\partial \theta_i} \tag{3.3}$$

where t represents an arbitrary/artificial time and i represents the index of each invertible parameter and its corresponding momentum. Note that each θ_i has its own unique p_i. This means that for a system of two parameters, the total problem is four-dimensional.

Equations (3.2) and (3.3) constitute a set of coupled ordinary differential equations that are used to update the parameters and momenta. The nature of these equations and their implying properties constitute the main tool that allows the algorithm to explore the *typical set* (Figure 3.2). Since we are not considering a true mechanical system but an analogous one, this exploration requires appropriate definitions of the potential and kinetic energy of the system.

The potential energy of the system may be formulated as a misfit function (e.g., Fichtner et al., 2021):

$$V(\boldsymbol{\theta}) = J = \frac{1}{2}\left(\boldsymbol{F}_{\boldsymbol{\theta}}^{\boldsymbol{mod}} - \boldsymbol{F}^{\boldsymbol{obs}}\right)^{T}\left(\boldsymbol{F}_{\boldsymbol{\theta}}^{\boldsymbol{mod}} - \boldsymbol{F}^{\boldsymbol{obs}}\right) \tag{3.4}$$

where $\boldsymbol{F}^{\boldsymbol{obs}}$ represents the observed natural data at n locations (e.g., EPMA data along a 1D mineral zoning profile), and $\boldsymbol{F}_{\boldsymbol{\theta}}^{\boldsymbol{mod}}$ represents the modeled compositions at the same locations. The scaled misfit J is non-negative as in a typical least-squares approach. A large value of J, and therefore $V(\boldsymbol{\theta})$, means that the model does not reproduce the observed data in a satisfactory way. Thus, in the framework of inversion, the smaller the "potential energy", the better the fit.

The kinetic energy, is traditionally introduced as:

$$T(\boldsymbol{p}) = \frac{1}{2}\boldsymbol{p}^{T}\boldsymbol{M}^{-1}\boldsymbol{p} \tag{3.5}$$

where $\boldsymbol{M}$ represents a symmetric and positive-definite matrix, the superscript "T" represents the transpose of vector $\boldsymbol{p}$ and the superscript "-1" denotes the inverse of matrix $\boldsymbol{M}$. This formulation is analogous to the general kinetic energy expression used in classical mechanics of 1 particle, $\frac{1}{2m}p^{2}$, where m is the mass of a particle and p is its momentum. However, more complicated formulations of kinetic energy (e.g., Riemannian approach) may also be used depending on the application and for efficiency reasons (e.g., Girolami & Calderhead, 2011). The mass matrix $\boldsymbol{M}$ could either represent a diagonal variance matrix that applies specific weights to different momenta, or a covariance matrix that also considers correlations between the different momenta. The mass matrix is commonly assumed to be equal to the unit matrix. However, $\boldsymbol{M}$ is critically used to guide efficient exploration (e.g., Fichtner et al., 2021).

With the current definitions of potential and kinetic energy, the Hamiltonian energy takes the following form:

$$H(\boldsymbol{\theta}, \boldsymbol{p}) = \frac{1}{2}\boldsymbol{p}^{T}\boldsymbol{M}^{-1}\boldsymbol{p} + J \tag{3.6}$$

and therefore, the *canonical equations* become:

$$\frac{d\theta_i}{dt} = \frac{\partial H(\boldsymbol{\theta}, \boldsymbol{p})}{\partial p_i} = [\boldsymbol{M}^{-1}\boldsymbol{p}]_i \tag{3.7}$$

$$\frac{dp_i}{dt} = -\frac{\partial H(\boldsymbol{\theta}, \boldsymbol{p})}{\partial \theta_i} = -\frac{dV(\boldsymbol{\theta})}{d\theta_i} = -\frac{dJ}{d\theta_i} \tag{3.8}$$

Equations (3.7) and (3.8) are solved numerically to update the positions (i.e., the invertible parameters) and (artificial) momenta of the system. Notice that based on equation (3.7), the parameter update is dependent on the momentum. Inversely, the momentum update is dependent on the parameters according to equation (3.8). In this way, the two variables form a feedback loop with one influencing the other.

To gain more insights into the dynamics, suppose the potential energy valley depicted in Figure 3.2A is defined by two invertible parameters θ_1 and θ_2 such as cooling rate and initial temperature. Areas that are high at the slopes of the valley correspond to high misfits and therefore bad fits between model outputs and data. The valley floor defines the best fits. The *mode* is the set of lower-most points that correspond to the minimum potential energy. Moreover, the *typical set* is the region around the *mode* that contains models that have high probability of reproducing the data.

Standard HMC algorithms begin by sampling random momenta from a Gaussian distribution $\mathcal{N}(0, \boldsymbol{M})$. That means that all momenta are drawn in a stochastic (random) way with a mean value of 0 and they can be correlated or scaled based on the mass matrix $\boldsymbol{M}$. An initial guess is also made for the invertible parameters θ_1 and θ_2. The initial draw of parameters positions the algorithm at point, such as point A of Figure 3.2A. This point has a high potential energy (i.e., a relatively bad data fit). Since it exists outside of the *typical set,* we use the *canonical equations* to propose a new acceptable sample which falls inside the *typical set.* For this, the *canonical equations* (3.7) and (3.8) are solved for several artificial time steps simulating a specific trajectory (for example from point A to point B in Figure 3.2B). This trajectory is uniquely determined by the initial guesses of momenta and parameters and the solution of the *canonical equations*. By simulating a trajectory, we make a large jump from point A to a new point B on Figure 3.2B. Crucially, along this trajectory, the Hamiltonian energy is conserved (for more details see Appendix A), while the kinetic and potential energy oscillate in magnitude so that the total energy is kept constant. This energy oscillation means that we explore different potential energy (misfit) magnitudes inside the *typical set, while being* confined within the *typical set* since the gradient of the potential energy is used.

Going from point A to point B (e.g., Figure 3.2), the gradient of potential energy of equation (3.8) is driving the initially drawn momenta in the direction of the mode. This part of HMC is similar to gradient descent. However, we do not apply gradient descent directly on the invertible parameters (θ_1, θ_2), because this would lead to a dissipative behavior and eventually

bring us directly to the *mode*. This would cause the algorithm to converge at the *mode* without being able to explore the *typical set*. In contrast, in the case of HMC, we are only updating the artificial momenta (i.e., the driving forces) according to the gradient of the potential energy, which is given by the misfit function defining the goodness-of-fit. Therefore, we are indirectly affecting the parameters with equation (3.7), which sees the contribution of the momenta. The feedback between momentum and parameters along with the conservation of Hamiltonian energy produces non-local, oscillatory movements. After reaching point B, we continue by resampling new momenta in a random manner. This marks the start of a new trajectory at a different Hamiltonian energy level which is still constrained within the *typical set*. The uncertainty in the observed data bounds the *typical set* as HMC progressively explores the parameter space. At point B, an accept/reject step is applied to ensure correct numerical implementation (see Appendix C for more details).

The solution of the *canonical equations* allows the algorithm to avoid areas of poor fit by using the gradient of the potential energy. Simultaneously, this avoids stagnation at the *mode*. To demonstrate this point, suppose that the combination of parameters reaches the mode at the misfit-valley floor. At this point, the gradient of the misfit function w.r.t. the parameters is $\frac{dJ}{d\theta_i} = 0$. The consequence of this is that the time derivative of the momenta is $\frac{dp_i}{dt} = 0$ and therefore the momentum remains constant (i.e., time invariant). However, the time derivative of the parameters is $\frac{d\theta_i}{dt} = [\boldsymbol{M}^{-1}\boldsymbol{p}]_i$ and since, in this case, the momenta are constant yet non-zero, the parameters will still be updated. In fact, the only way to converge at the mode is if the momentum $\boldsymbol{p} = 0$. However, the random sampling of momenta makes this scenario almost impossible, as desired in order to sample the typical set.

The previous parts describe the main logic of Hamiltonian Monte Carlo. However, most published algorithms that perform HMC such as *Stan* (Carpenter et al., 2017) and *AdvancedHMC.jl* (Fjelde et al., 2025; Ge et al., 2018; Xu et al., 2020), use a different but equivalent approach. These algorithms define the Hamiltonian energy in the following manner:

$$H(\boldsymbol{\theta}, \boldsymbol{p}) = \frac{1}{2}\boldsymbol{p}^T\boldsymbol{M}^{-1}\boldsymbol{p} - \log\left[\mathcal{L}\left(\boldsymbol{F}^{\boldsymbol{obs}}|\boldsymbol{\theta}\right)\Pi(\boldsymbol{\theta})\right] \tag{3.9}$$

where $\mathcal{L}\left(\boldsymbol{F}^{\boldsymbol{obs}}|\boldsymbol{\theta}\right)$ is called the *likelihood* function and $\Pi(\boldsymbol{\theta})$ is the *prior* probability of $\boldsymbol{\theta}$. The symbol "|" denotes that the *likelihood* is a conditional probability. The first term of the right-hand side is the kinetic energy $T(\boldsymbol{p})$ $(Eq. 5)$, and the second term is the potential energy $V(\boldsymbol{\theta})$.

$\Pi(\boldsymbol{\theta})$ represents *prior* heuristic knowledge of the parameters $\boldsymbol{\theta}$. For example, $\Pi(\boldsymbol{\theta})$ may be the initial temperature defined as normal distribution given as a specified mean and standard deviation (e.g., 625 ± 25 °C). This type of *prior* information can be derived from petrological data and other constraints like thermobarometry or simply be assumed and tested. Note that $\Pi(\boldsymbol{\theta})$ is a constant distribution and does not evolve during the simulation. $\mathcal{L}(\boldsymbol{F^{obs}}|\boldsymbol{\theta})$ serves an equivalent purpose to the misfit function of equation (3.4). $\mathcal{L}(\boldsymbol{F^{obs}}|\boldsymbol{\theta})$ is a function that quantifies how the modeled values deviate from the observed data for a given set of $\boldsymbol{\theta}$. In other words, it expresses how probable it is to obtain $\boldsymbol{F^{obs}}$, given the specified set of parameters $\boldsymbol{\theta}$. The multiplication of the *prior* and *likelihood* probabilities in the second term of the right-hand side of equation (3.9) defines the unnormalized *posterior* probability. This is the target probability that we are aiming to obtain (e.g., Bailer-Jones, 2017). The *posterior* probability, which is usually denoted as the conditional $\Pi(\boldsymbol{\theta}|\boldsymbol{F^{obs}})$, simply expresses how the values of the parameters are distributed based on their ability to reproduce the observed data within their respective errors. equation (3.9) is a direct equivalent of equation (3.6). This is because the small non-negative values of $\mathcal{L}(\boldsymbol{F^{obs}}|\boldsymbol{\theta})$ correspond to a bad fit between model and observed data. In this case, the potential energy is high and reflects position A in Figure 3.2A. When the likelihood is significant, it means that the chosen invertible parameters $\boldsymbol{\theta}$ are able to reproduce the observed data $\boldsymbol{F^{obs}}$, following the Bayesian formalism. For a more detailed explanation on the analogy between the misfit formulation and the Bayesian approach, the reader is referred to Appendix B. For additional insights into the HMC algorithm, the reader is referred to Appendix C.

3.3 Methods

3.3.1 *Turing.jl*, *AdvancedHMC.jl* and Automatic Differentiation

Here we used the *AdvancedHMC.jl* package (Xu et al., 2020) as it is implemented in the *Turing.jl* probabilistic library (Fjelde et al., 2025) of the Julia programming language (Bezanson et al., 2017). *AdvancedHMC.jl* follows the probabilistic Bayesian approach of equation (3.9). However, it offers many additional options to improve adaptability and efficiency for specific problems. For example, *AdvancedHMC.jl* provides different choices for the numerical implementation of the *canonical equations* but also for the formulation of the kinetic energy. For the purposes of this paper, we use the "No-U-Turn Sampler (NUTS)" algorithm proposed by Hoffman & Gelman (2014) and implemented in *AdvancedHMC.jl*. The NUTS determines automatically an optimal trajectory length for each Hamiltonian path.

We adopted the normal *leapfrog* numerical integration scheme (see Appendix C) and a Gaussian kinetic energy (eq 5) with an adaptive diagonal mass matrix (see Xu et al., 2020 for more details). Finally, the computation of the gradient of the potential energy with respect to the invertible parameters $\boldsymbol{\theta}$, is calculated with Automatic Differentiation (AD). This method allows accurate derivative computation. For a comprehensive overview of AD, see Neidinger (2010). We use the *ForwardDiff.jl* package (Revels et al., 2016) to compute derivatives within the HMC framework.

3.3.2 Forward numerical modelling

The main goal of our inversion is to fit the compositional profiles of garnets and also the $^{40}Ar/^{39}Ar$ (argon-argon) age of muscovite from the metamorphic sole schists of the Pindos ophiolite (Moutzouris et al., 2025). For this, we use two different numerical models and invert for the initial cooling rate, initial temperature and effective grain size (used only for the diffusion in muscovite). These parameters correspond to the vector $\boldsymbol{\theta}$. The numerical models used are GDIFF (Moulas, 2023) and KADMOS (Moulas & Brandon, 2022). GDIFF is a one-dimensional implicit Finite Difference (FD) numerical code designed to simulate multicomponent diffusion in garnet (see Appendix D for details). Here, it is used to reproduce the compositional profiles of garnets from the Pindos metamorphic sole and invert for the apparent cooling rate and the initial equilibration temperature. KADMOS, on the other hand, is a Finite Element (FE) diffusion code that models apparent $^{40}K/^{40}Ar$ (and their associated $^{40}Ar/^{39}Ar$) age profiles in various minerals (see Appendix E). It is used to simulate the apparent cooling age of a muscovite separated from a metapelite sampled at the same locality and to invert for initial cooling rate, initial equilibration temperature and effective grain size. Both GDIFF and KADMOS were translated in the high-level Julia programming language to ensure compatibility with the HMC method and AD packages while leveraging the computational efficiency for higher model performance. The codes were benchmarked to ensure they produce results identical to those of the original versions (Figure S. 3.1 and Figure S. 3.2).

All codes developed for this study, along with their corresponding documentation that discusses technical details and usage, are published in a permanent Zenodo repository (https://doi.org/10.5281/zenodo.18247900). These codes allow the results presented in this paper to be reproduced. Furthermore, they may also easily be adapted for other applications and inversion using HMC, GDIFF and KADMOS.

3.3.3 Analytical techniques

1D Compositional garnet profiles were acquired at the Institute of Geosciences of the Johannes Gutenberg University of Mainz (Germany) using EPMA. The analytical details regarding the equipment and operating conditions for EPMA can be found in the supplementary material of Burg & Moulas (2022). Analytical details on the measurement of the apparent age of muscovite are given in Moutzouris et al. (2025).

3.3.4 The Pindos metamorphic sole

The metamorphic sole of the Pindos ophiolite will serve as a case study for inverse modeling and the application of HMC. The Pindos ophiolite is located in northwestern Greece and is Jurassic in age (Liati et al., 2004). It is comprised of a metamorphic sole that includes sheets of metasediments and metabasites. Here, we focus on garnet-mica schists and a hornblende-plagioclase amphibolite studied and described in detail in Moutzouris et al. (2025). They showed that the garnet-bearing metapelites have equilibrated at upper-amphibolite facies conditions at 630 ± 20 °C and 1.1 ± 0.2 GPa. A muscovite separate from the sole metapelite gave an apparent $^{40}Ar/^{39}Ar$ cooling age of 164.16 ± 0.37 Myr (million years; Moutzouris et al., 2025; their fig. 7B). Over incremental heating steps muscovite showed a curved spectrum which is typical for diffusion processes (e.g., Kelley, 2002; Turner et al., 1966). Additionally, a hornblende separate from the sole amphibolites gave an apparent $^{40}Ar/^{39}Ar$ age of 165.5 ± 0.73 Myr. Hornblende showed a well-defined apparent age plateau indicating no argon loss. This served as a strong indication that the observed age corresponds to the formation age of the amphibolite (Moutzouris et al., 2025). Based on these data, Moutzouris et al. (2025) proposed that the rocks have cooled rapidly after the attainment of the equilibration conditions. However, the precise assessment of the cooling rates and their uncertainties was beyond the scope of the previous study.

3.4 Results

3.4.1 Garnet compositional profiles

Almandine-rich, porphyroblastic garnets in metapelites from the Pindos metamorphic sole exhibit strong compositional zonation. In the present study, we investigated three representative garnet porphyroblasts (Grt7, Grt14, Grt15 of Moutzouris et al., 2025), all of which display consistent zonation patterns. The garnets show a spherical geometry and they are commonly adjacent to chlorite replacing biotite (Moutzouris et al., 2025). Their radius varies from 50 to 200 μm. Figure 3.3 shows the compositional profile of Grt14, while the

profiles of the remaining two garnets are available in the supplementary material (Figure S. 3.3 and Figure S. 3.4). From core to rim, the almandine content increases progressively, followed by a gradual decrease toward the rim (Figure 3.3A). The spessartine component displays a bell-shaped zonation pattern with a slight increase in the outermost ~20 µm of the rim (Figure 3.3B). This late-stage enrichment in spessartine is typically associated with resorption processes (Kohn & Spear, 2000). The garnets show a near-linear increase in pyrope content, rising from approximately 0.13 to 0.21 (Figure 3.3C). In contrast, the grossular component exhibits a more complex behavior and sharp compositional profiles (Figure 3.3D). It is initially higher at the core (~0.055), followed by a gradual asymptotic decrease over the next ~50 µm. This is interrupted by a sharp increase to ~0.04 and a second smaller increase in the final ~10 µm toward the rim.

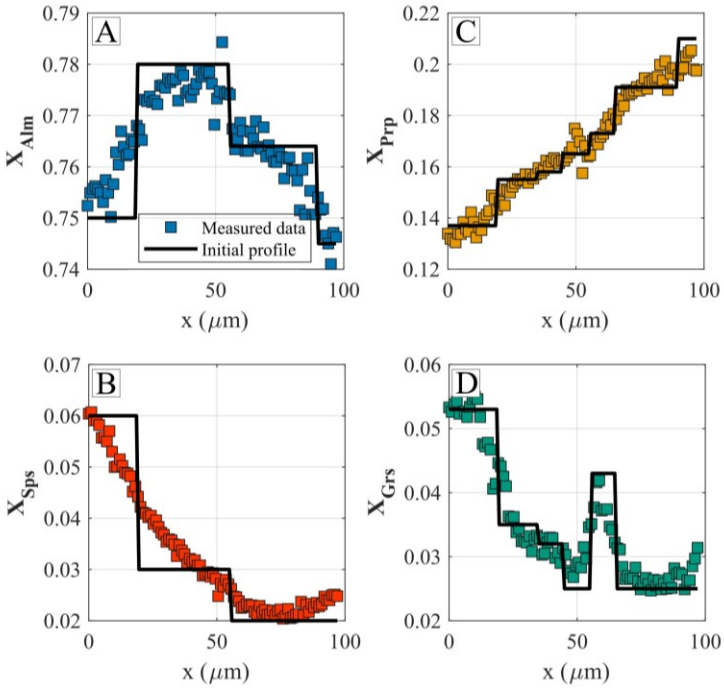

Figure 3.3: Measured compositional profiles of the almandine, pyrope, spessartine and grossular components (X_{Alm}, X_{Prp}, X_{Sps}, X_{Grs}) in Grt14 and initial conditions used for the evaluation of GDIFF models. A coordinate of 0 corresponds to the core of garnet.

3.4.2 GDIFF: Inversion with two parameters

The compositional garnet profiles from the Pindos schists were simulated using GDIFF. Step-wise initial conditions were assumed by setting the spessartine endmember of garnet as dependent component. The initial conditions for the three different modeled garnets are shown in Figure 3.3, Figure S. 3.3 and Figure S. 3.4. We assumed a Dirichlet boundary condition (i.e.,

constant concentration) for the outer rim of garnets to simulate the effect of the main matrix of the rock. Moreover, we considered a no-flux Neumann boundary condition for the core of garnets due to symmetry. The tracer diffusivity coefficients of Chakraborty & Ganguly (1992) and the diffusivity matrix formulation of Lasaga (1979) were adopted. This dataset was selected as it more accurately reproduces natural data (Cheng et al., 2020).

Our investigation focused on deducing cooling rates associated with near-peak temperature conditions. Therefore, we primarily aimed to reproduce the compositional zonation formed prior to the development of the outermost garnet rim. This approach allows us to constrain the maximum cooling rate required to preserve the chemical zonation close to peak *P-T* conditions. We assume that the rock has followed an asymptotic cooling path of the following form (e.g., Lasaga, 1983, his eq 17):

$$T = \frac{T_{max}}{\left(1 + \frac{s \cdot t}{T_{max}}\right)} \tag{3.10}$$

where T_{max} is the initial (peak) temperature, s is the initial cooling rate and t is time in million years (Myr). T_{max} and s are the primary parameters that we invert for here. The simulations are terminated at a final temperature of 300 °C, which falls well below the closure temperature of this system, below which diffusional modification becomes negligible.

Inversion was initially carried out using a direct search approach to explore the parameter space. We assumed that T_{max} varies from 500 to 700 °C and that s varies from 50 to 500 °C/Myr in accordance to the expected cooling rates of Moutzouris et al. (2025). The model pressure was set to 1.1 GPa, consistent with the estimated pressure at the thermal maximum for the Pindos sole (Moutzouris et al., 2025). Direct search considers all of the possible combinations of the two parameters in the specified range and evaluates a unique model for each combination. The two variables are discretized with a resolution of 100 grid points per parameter. Therefore, a total of 10,000 model evaluations are required to explore the parameter space. This resolution was chosen to ensure that possible low-misfit regions are adequately resolved. In addition, the direct search approach allows the identification of local minima, if present.

To quantify the goodness of fit between modeled and observed data we used a misfit function similar to equation (3.4):

$$J_{garnet} = \sum_{i=1}^{k}\sum_{j=1}^{n} w_{Alm}\left(Alm_{model}^{i,j} - Alm_{obs}^{i,j}\right)^2 + w_{Grs}\left(Grs_{model}^{i,j} - Grs_{obs}^{i,j}\right)^2 + w_{Prp}\left(Prp_{model}^{i,j} - Prp_{obs}^{i,j}\right)^2 + w_{Sps}\left(Sps_{model}^{i,j} - Sps_{obs}^{i,j}\right)^2 \quad (3.11)$$

where Alm, Grs, Prp and Sps indicate the almandine, grossular, pyrope and spessartine components of garnet in mole fraction, respectively, n is the number of spatial points (i.e., measurements) and k is the total number of garnets (in this case $k = 3$). With this misfit definition, the three different garnets (Grt7, Grt14 and Grt15) are considered together. The factor w corresponds to associated weights attributed to each individual component. Weighting factors were considered to evaluate the influence of the grossular component on the misfit calculation. The importance of this lies in the fact that, among Mg, Fe, Mn and Ca, Ca exhibits the slowest diffusion in garnet (Chakraborty & Ganguly, 1992). Also, the grossular component in the studied garnets shows the sharpest compositional gradients. A numerical spatial resolution of 100 grid points was adopted for all models. Finally, we used a numerical timestep of 0.02 Myr which ensures that the modeled profiles have an error well below 1 % associated with the temporal resolution (Figure S. 3.5).

The results of the direct search approach, assuming equal weights across all garnet endmembers, are presented in Figure 3.4, created by summing the individual misfit maps for the three modeled garnets and displays the total misfit on a logarithmic scale. In this map, each combination of initial temperature and initial cooling rate corresponds to a unique misfit value. It is apparent that initial equilibration temperatures below ~600 °C fail to reproduce the profiles of the three garnets for any cooling rate as they produce large misfits. The same holds true for initial temperatures higher than ~675 °C. However, a well-defined zone of low-misfit values is observed (blue area in Figure 3.4). This zone clusters around an initial temperature comprised between 600 and 650°C for any choice of cooling rate, which is remarkably close to the independent constraint of 630 ± 20°C inferred in Moutzouris et al. (2025). We further explored the influence of assigning a higher weighting factor to the grossular component on the misfit calculation. Assuming that the contribution of grossular to the misfit is ten times greater than that of the other components, the low-misfit zone remains virtually unchanged (Figure S. 3.6), corroborating the robustness of our approach.

We now discuss the exploration of the same parameter space between initial temperature and initial cooling rate using HMC. As with the direct search approach, we use the same asymptotic cooling path of equation (3.10) until a final temperature of 300 °C. The *prior* probability

distribution for the initial temperature was assumed to follow a Gaussian distribution of $\mathcal{N}(630,20)$, following the independent thermobarometric results of Moutzouris et al. (2025) with a mean value of 630 °C and a standard deviation of 20 °C. Since there is no available constraint on the distribution of the initial cooling rate (e.g., Gaussian), we used a uniform *prior* ranging from 50 to 500 °C/Myr. The uniform distribution assumes that all values between 50 and 500 °C/Myr have equal initial probability of reproducing the data. For the *likelihood* specification in *Turing.jl*, the observed concentrations at each spatial point are modeled as normally (Gaussian) distributed around the corresponding model predictions. The errors between different spatial points are assumed to be independent. We considered a measurement uncertainty of 0.01 (i.e., 1 %) for each spatial point and across all compositional end-members of garnet. This is equivalent to assigning the same weighting factor for all endmembers. A total number of 600 *posterior* samples were generated for the combined parameter space of the three garnets to ensure convergence. We adopted the NUTS (see section 2.1.5) which is defined by an initial "warm-up" (also known as "burn in") phase during which the step size of the algorithm and the mass matrix are adapted. Finally, a random seed of 44 was used for all models to ensure reproducibility.

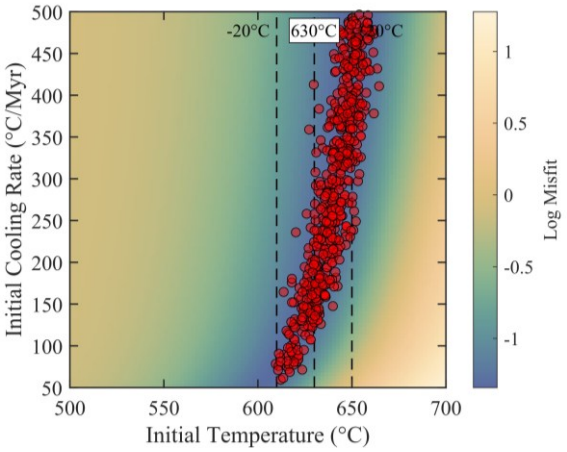

Figure 3.4: Combined misfit map generated using a direct search method integrating three different garnets (Grt7, Grt14 and Grt15). This map is presenting the goodness of fit between the modeled GDIFF output and the natural observations. Each combination of initial temperature and initial cooling rate represents a unique model evaluation and produces a unique misfit value. A low-misfit region (colored in blue) is identified. The combinations of parameters that fall inside this low-misfit zone are able to reproduce the compositional profiles of all three garnets. Interestingly, the low-misfit region coincides with independent thermobarometric estimations (630 ± 20 °C; Moutzouris et al., 2025). The red points represent

the accepted HMC samples that were independently used to explore this parameter space. Notice that fewer samples are required to explore the parameter space with HMC (see main text).

The results of the HMC simulation for the combined parameter space of the three garnets are shown in Figure 3.5. Figure 3.5A and 3.5B present accepted sample values of initial temperature and cooling rate across iterations. These plots are also referred to as *trace* plots and they show the values of each variable that have been progressively accepted. *Trace* plots can be useful to determine the convergence of the algorithm. Convergence occurs when the *trace* plot shows no large-scale trend or drift. This indicates that the samples are exploring the *posterior* distribution efficiently. The *trace* plots presented in Figure 3.5 show no systematic trends which is indicative of convergence of the algorithm.

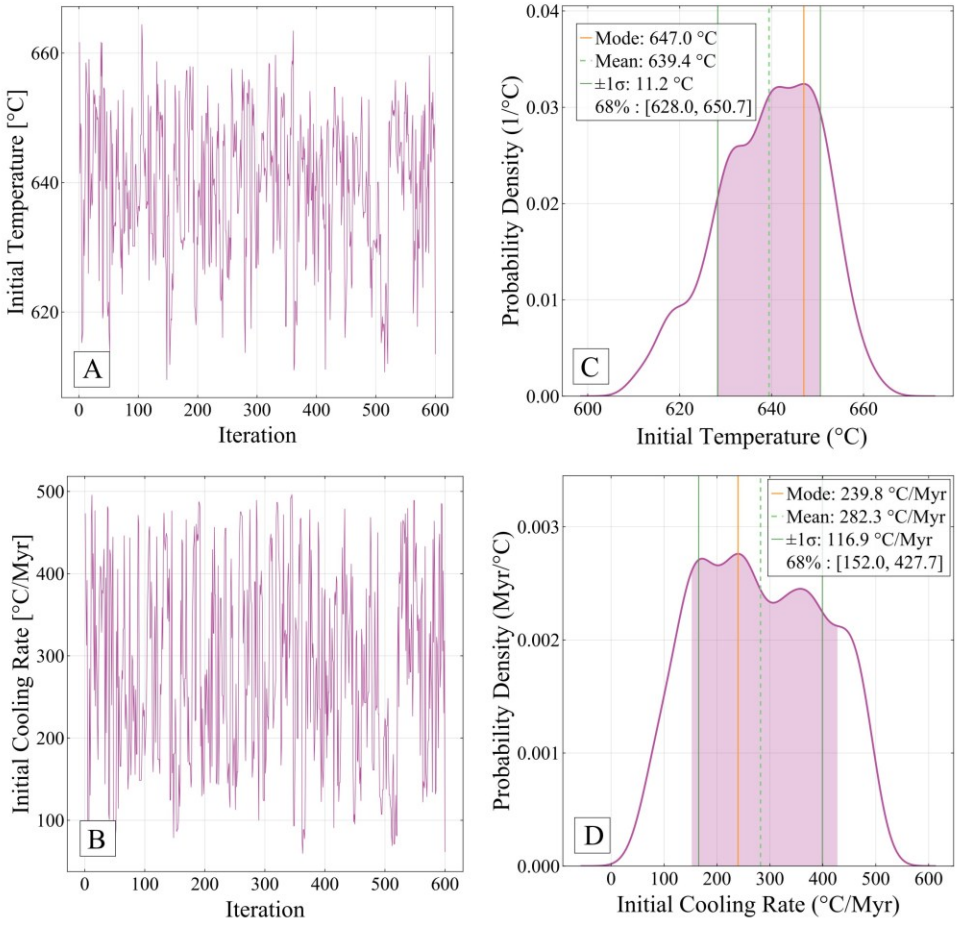

Figure 3.5: *Trace* plots (A, B) and *posterior* distributions (C, D) for initial temperature and initial cooling rate acquired using an HMC approach and GDIFF for the combined parameter space of the three investigated garnets. The *trace* plots display the parameter values accepted by the algorithm over successive iterations. The *posterior* distributions quantify the

uncertainties on the invertible parameters. The inverted initial temperature distribution is Gaussian. The initial cooling rate shows a uniform distribution with various cooling rates being able to reproduce the observed data. The mean, standard deviation, *mode* and the *typical sets* are also presented in the legends of each *posterior* plot (see also main text). The initial cooling rate has a 68 % probability of lying between 152.0 and 427.7 °C/Myr.

The accepted samples acquired with HMC can be used to infer statistics and quantify uncertainties on the invertible parameters. Figure 3.5C and 3.5D show the *posterior* probability distributions for initial temperature and cooling rate. The peaks of the *posterior* curves show the parameter values with the highest probability of reproducing the observed garnet compositions. These values represent the *modes*. The *posterior* distribution of initial temperature (Figure 3.5C) shows Gaussian characteristics. The *mode* of the initial temperature is at 647.0 °C. The mean and standard deviation of the initial temperature are 639.4 ± 11.2 °C. Figure 3.5C also indicates a 68 % probability that the initial temperature lies between 628.0 and 650.7 °C. The initial cooling rate shows a uniform behavior with negligible peaks of high probability (Figure 3.5D). This shows that a wide range of initial cooling rates reproduce the data similarly well. The mean and standard deviation of the initial cooling rate are 282.3 ± 116.9 °C/Myr. The *mode* is at 239.8 °C/Myr and 68 % of the probability mass lies between 152.0 and 427.7 °C/Myr.

Direct comparison of the *posterior* samples and distributions with the misfit maps shows that HMC can identify and focus the sampling exclusively inside the low-misfit zone (Figure 3.4). Noticeably, for the case of two parameters, the total computation time was several times higher compared to the direct search approach (Table 3.1). We considered cases with fewer samples that resulted in lower total computational time but convergence was not possible as the *posterior* of the initial cooling rate showed bimodality.

3.4.3 KADMOS: Inversion with three parameters

KADMOS was used to fit the apparent $^{40}Ar/^{39}Ar$ age of muscovite (164.16 ± 0.37 Myr, Moutzouris et al., 2025) from the Pindos metamorphic sole. As with GDIFF, a direct search approach was initially used to invert only for initial temperature and cooling rate. We assumed a spherical geometry and a muscovite grain size of 20 μm. Diffusion data were taken from Harrison et al. (2009). Pressure was again fixed at 1.1 GPa. We used a resolution of 100 elements and an adaptive grid to capture sharp concentration gradients near the muscovite rim (see Appendix E for more details). The Ar concentration at the rim of muscovite was set to

zero (i.e., Dirichlet boundary condition) to simulate argon escape. A zero-flux (i.e., Neumann) boundary condition was applied at the core of muscovite due to symmetry. We assumed an asymptotic cooling path (eq 10) and varied the initial temperature between 500 and 700 °C. The initial cooling rate ranged from 50 to 500 °C/Myr. We used a parameter grid with a resolution of 100 for each variable. In this case, the misfit is simply calculated as:

$$J_{muscovite} = \left(t_{model}^{muscovite} - t_{obs}^{muscovite}\right)^2 \quad (12)$$

where $t_{model}^{muscovite}$ is the core (maximum) age of the modeled profile in each model evaluation and $t_{obs}^{muscovite}$ is equal to 164.16 Myr. Finally, a numerical timestep of 0.27 Myr was chosen as it produces relative errors below 0.1 % (Figure S. 3.7).

Based on the findings of Moutzouris et al. (2025), we assume that the metamorphic sole metapelite from the Pindos ophiolite was metamorphosed together with the associated amphibolites. This is favored due to the spatial and geochronological relationship between the two rocks. Therefore, we assume that the age of hornblende from the amphibolite corresponds to the age of peak metamorphic conditions. As a consequence, we used a total model duration of 165.5 Myr for the KADMOS models.

The results of direct search for two parameters with KADMOS are shown in Figure 3.6. A narrow field of low misfits is identified (blue region). In this case, the low-misfit zone indicates that the models are sensitive with respect to the initial cooling rate but not as much to the initial temperature. This is the opposite behavior compared to GDIFF. If we assume, based on petrological constraints, initial temperatures of 630, 650 and 610 °C, which correspond to previous thermobarometric results (630 ± 20 °C), then the implied cooling rates are approximately 185, 205, 160 °C/Myr, respectively.

The HMC approach was implemented using the same asymptotic cooling (eq 10). We used a uniform *prior* distribution for initial cooling rate ranging from 50 to 500 °C/Myr following the same logic to the models with GDIFF. A total 100 *posterior* samples were drawn using NUTS. The measured uncertainty of the $^{40}Ar/^{39}Ar$ age of muscovite (± 0.37 Myr) was used for the evaluation of the *likelihood*.

The results of HMC using KADMOS for two parameters are presented in Figure 3.7 and more details on the HMC runs are found in Table 3.1. Based on the *trace* plots (Figure 3.7A and 3.7B) convergence has been achieved. Figure 3.7C and 3.7D show that the *posterior* distributions are well-behaved and Gaussian. The *mode* of initial temperature coincides well

with the mean value at ~630 °C. The 68 % probability region lies between ~617.6 and 647.9 °C. For the initial cooling rate, the mean value and standard deviation are 244.0 ± 87.5 °C/Myr. The *mode* lies at a value of 196.7 °C/Myr and the 68 % probability region is within 164.9 and 328.3 °C/Myr. Interestingly, Figure 3.7D indicates that cooling rates above 300 °C/Myr also show a considerable probability of reproducing the observed age of muscovite within its uncertainty. This is not immediately evident by exclusively using the misfit map produced with direct search (Figure 3.6). It is also important to notice that the observed muscovite age cannot be reproduced by cooling rate values below ~100 °C/Myr (Figure 3.7B, 3.7D and 3.6). Finally, in this case, HMC explored the parameter space in a computational time comparable to that of the direct search approach (Table 3.1).

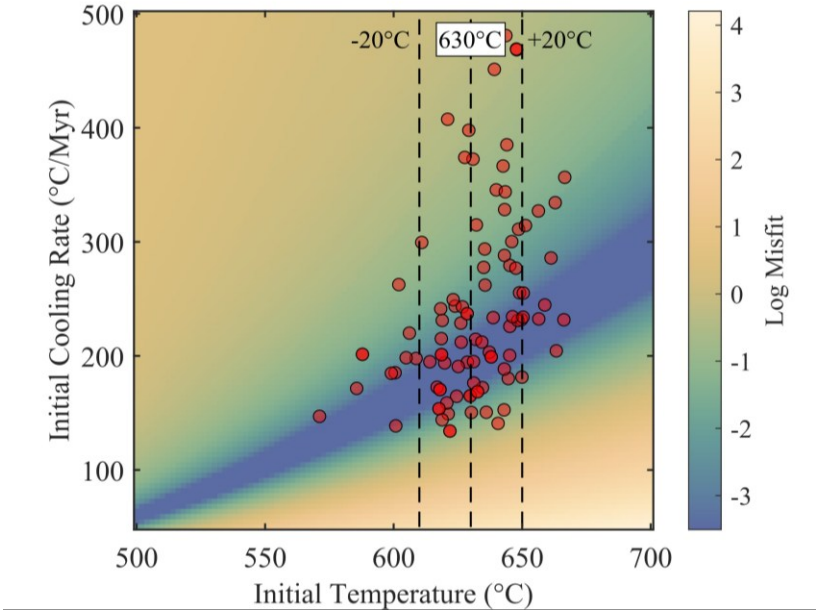

Figure 3.6: Calculated misfit map created based on a direct search approach for the ^{40}Ar-^{39}Ar age of muscovite. This map is presenting the goodness of fit between the modeled KADMOS output and the measured ^{40}Ar-^{39}Ar age of muscovite in our sample. A low-misfit region (blue colors) is identified. Assuming an initial temperature equal to ~630 °C, a cooling rate of ~180 °C/Myr is inferred. The red points represent the accepted HMC samples that were independently used to explore this parameter space based on KADMOS.

In the previous two-dimensional example, the grain size was assumed to be equal to 20 µm. However, this parameter is unknown since multiple grain sizes are measured during the acquisition of the $^{40}Ar/^{39}Ar$ age. For this reason, we tested inverting additionally for an effective grain size. This makes the inversion problem three-dimensional with initial temperature, initial cooling rate and effective grain size as parameters. A direct search approach

was initially used in which we evaluated models for all possible combinations between initial temperature, cooling rate and effective grain size. The effective grain size ranged from 5 to 70 µm. We discretized the parameters with a resolution of 100 which resulted in 1,000,000 KADMOS model evaluations and a total computation time of 44.28 hours (Table 3.1). Misfits were plotted in a three-dimensional cube (Figure S. 3.8). Figure S. 3.8 shows a well-defined low-misfit zone. The vertical shape of this low-misfit zone shows that the fit of the muscovite age does not significantly depend on the effective grain size.

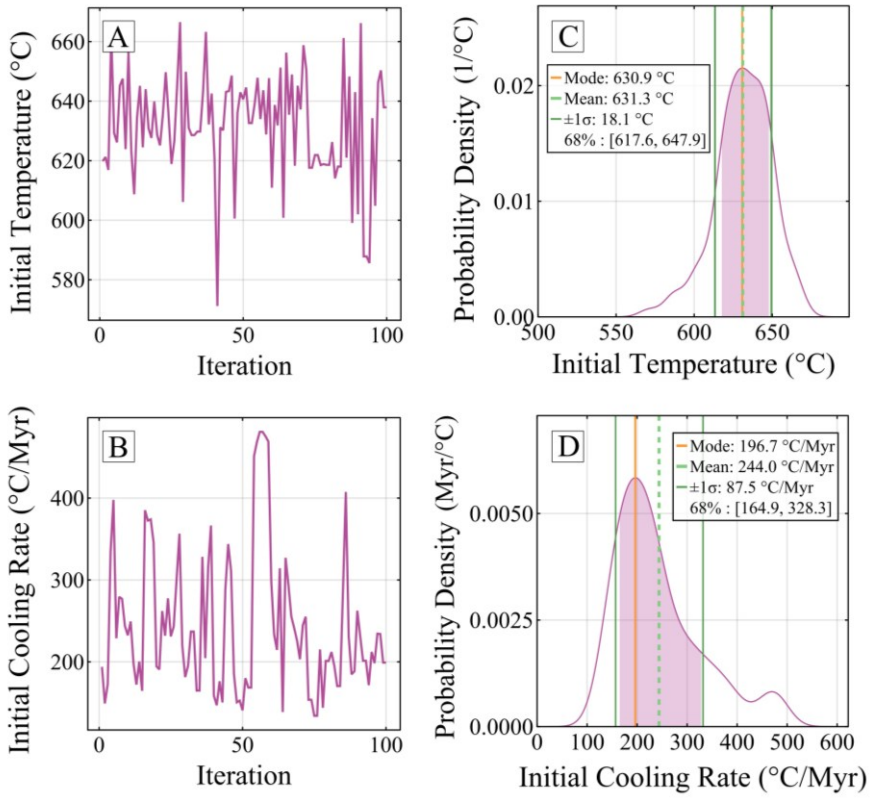

Figure 3.7: *Trace* plots (A, B) and *posterior* distributions (C, D) for initial temperature and initial cooling rate acquired using HMC and KADMOS in a two-dimensional parameter space. Both *posterior* distributions show a Gaussian behavior and efficiently sample the parameter space showing the values of initial cooling rate and temperature that are able to reproduce the muscovite age with significant probability. The initial cooling rate has a 68 % probability of lying between 164.9 and 328.3 °C/Myr with the most probable value being at 196.7 °C/Myr.

The three-dimensional parameter space was subsequently explored with HMC to check for the consistency of the inversion results. The *prior* distribution of the effective grain size was assumed uniform, ranging from 5 to 70 µm. The *priors* for initial temperature and cooling rate were kept the same as in the two-dimensional case. We have drawn a total number of 600

samples to explore the three-dimensional parameter space. For this number of samples, a total of 9,541 KADMOS model evaluations were needed and convergence was achieved in 5.8 hours of computation time (Table 3.1). The accepted samples in the three-dimensional parameter space are plotted as black points in Figure S. 3.8. The *posterior* distributions based on the accepted samples are plotted in Figure 3.8. All parameters show convergence based on their corresponding *trace* plots (fig. 8A to 8C). The initial temperature and cooling rate *posterior* distributions (Figure 3.8D and 3.8E) show identical behavior compared to the two-dimensional case (Figure 3.7). The 68 % probability region for initial temperature lies between 612.5 and 651.2 °C while the *mode* is at 633.2 °C. The 68 % probability region for the initial cooling rate is between 153.5 and 320.6 °C/Myr and the *mode* is at 197.9 °C/Myr. The effective grain size shows an almost uniform *posterior* distribution (Figure 3.8F), indicating that it is uninformative and does not contribute significantly to constraining the muscovite age. The minor degree of bimodality in the *posterior* distribution of the effective grain size may reflect the fact that a slightly larger sample size is required to fully resolve its structure.

3.4.4 Joint inversion

Sections 3.3 and 3.4 presented inversion results from two physically independent modeling systems. To identify the conditions that satisfy both systems simultaneously, the misfits from Figure 3.4 and Figure 3.6 can be combined. The two independent misfit maps were first normalized with their respective maximum values to ensure that they are dimensionless and comparable in magnitude. The normalized misfit maps were then added. The resulting combined map, shown in Figure 3.9, highlights the region where low-misfit zones from the two individual systems overlap. This optimal region can be identified between initial temperatures ranging from 610 to 650 °C and initial cooling rates from approximately 150 to 300 °C/Myr. The region represents the parameter combinations that simultaneously reproduce both garnet compositional profiles and the muscovite $^{40}Ar/^{39}Ar$ age. An absolute minimum misfit is found at an initial temperature of 631 °C and a cooling rate of 195 °C/Myr.

Using HMC, we now systematically explore this combined parameter space and assess it statistically. This was done by combining GDIFF for the three different garnets and KADMOS for the muscovite and exploring the joint *posterior* distribution of the initial temperature, cooling rate and effective grain size. In this way, HMC samples the joint likelihood surface directly, eliminating the need for separate inversions. For this analysis, we once more assumed a uniform *prior* on cooling rate ranging from 50 to 500 °C/Myr and a Gaussian prior on initial temperature of $\mathcal{N}(630,20)$. The effective grain size was assumed to have a uniform *prior*

ranging from 5 to 70 µm. A total of 400 samples were drawn, using the same uncertainty structure as in the previous sections. A random seed equal to 44 was once again used for reasons of reproducibility.

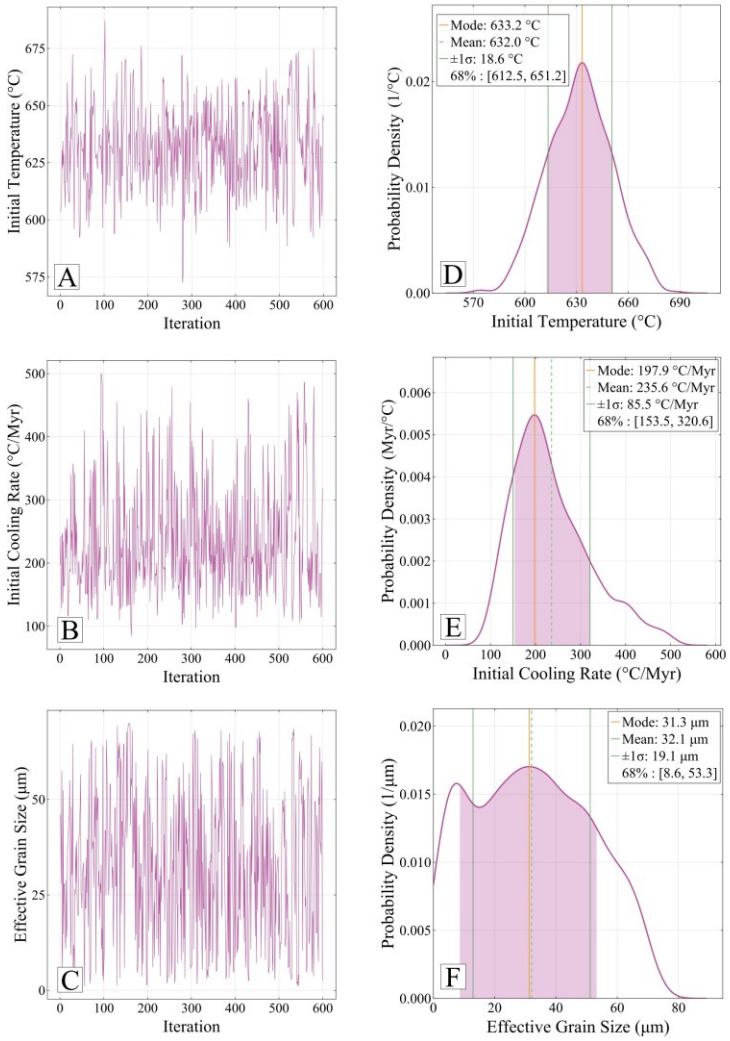

Figure 3.8: *Trace* plots (A, B, C) and *posterior* distributions (D, E, F)) for initial temperature, initial cooling rate and effective grain size acquired using HMC and KADMOS in the three-dimensional parameter space. The *posterior* distributions of initial temperature and cooling rate show the same Gaussian distribution as in the two-dimensional case (Figure 3.7). The effective grain size shows a uniform distribution, indicating that it does not affect the fit of the muscovite age significantly.

The results of the combined HMC approach are presented in Figure 3.10. Based on Figure 3.10A, 3.10B and 3.10C, the algorithm has converged. Figure 3.10D and 3.10E show that both the initial cooling rate and temperature are represented by well-behaved Gaussian *posterior* distributions. The initial temperature has a mean and standard deviation of 637.6 ± 8.3 °C. The

mode is located at 638.1 °C and 68 % of the probability mass lies between 629.0 and 645.6 °C. The initial cooling rate has a mean and standard deviation of 241.3 ± 76.5 °C/Myr. The mode is found at 189.5 °C/Myr and 68 % of the probability mass is observed between 166.0 and 314.4 °C/Myr. The effective grain size, shown in Figure 3.10F, shows a uniform *posterior* distribution with the 68 % probability region lying between 10.0 and 55.3 μm. The HMC-derived samples map the low-misfit region that satisfies both physical models (Figure 3.9). Based on the accepted initial cooling rates and initial equilibration temperatures, the resulting cooling paths are illustrated in Figure S. 3.9. Finally, Figure 3.9 and Figure 3.10 show that initial cooling rates in excess of 100 °C/Myr are needed to reproduce the investigated natural data from the Pindos metamorphic sole.

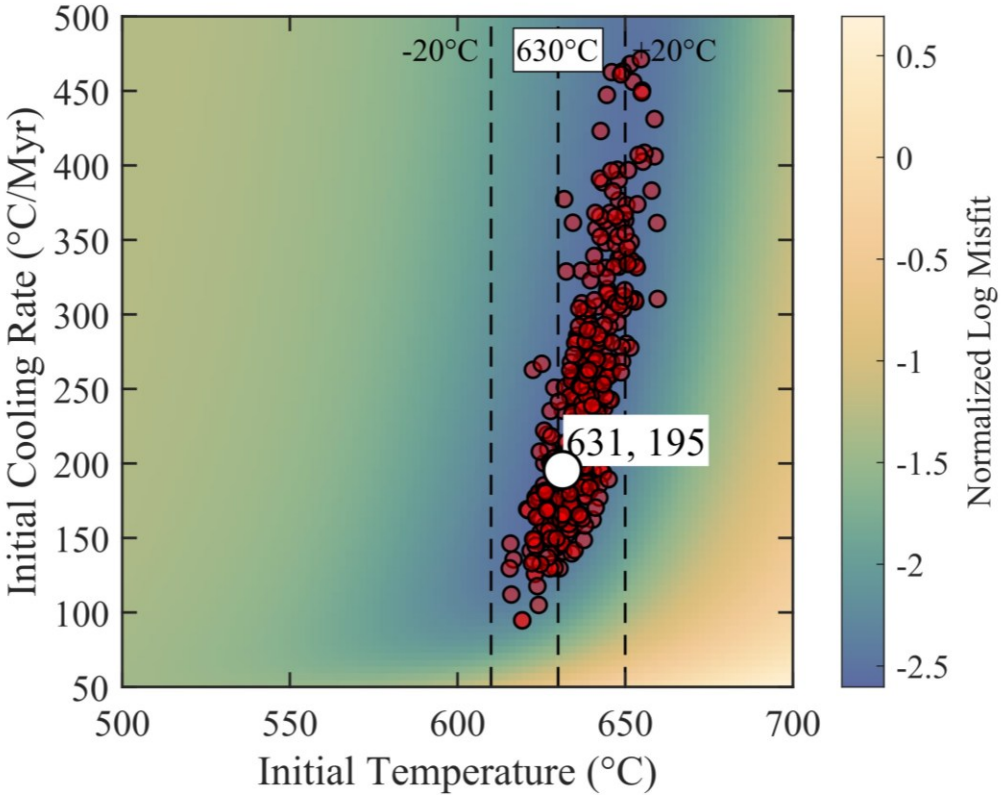

Figure 3.9: Combined misfit map showing the result after the addition of the individual misfit maps of Figure 3.4 and Figure 3.6. This misfit map is showing the combinations of initial temperature and cooling rate that are able to reproduce both garnet compositional profiles and the ^{40}Ar-^{39}Ar age of muscovite at the same time. The low-misfit region (blue color) coincides well with previous thermobarometric results (Moutzouris et al., 2025) and shows a point with absolute minimum misfit at 631 °C and 195 °C/Myr. The red points correspond to the independently obtained HMC samples during this joint inversion.

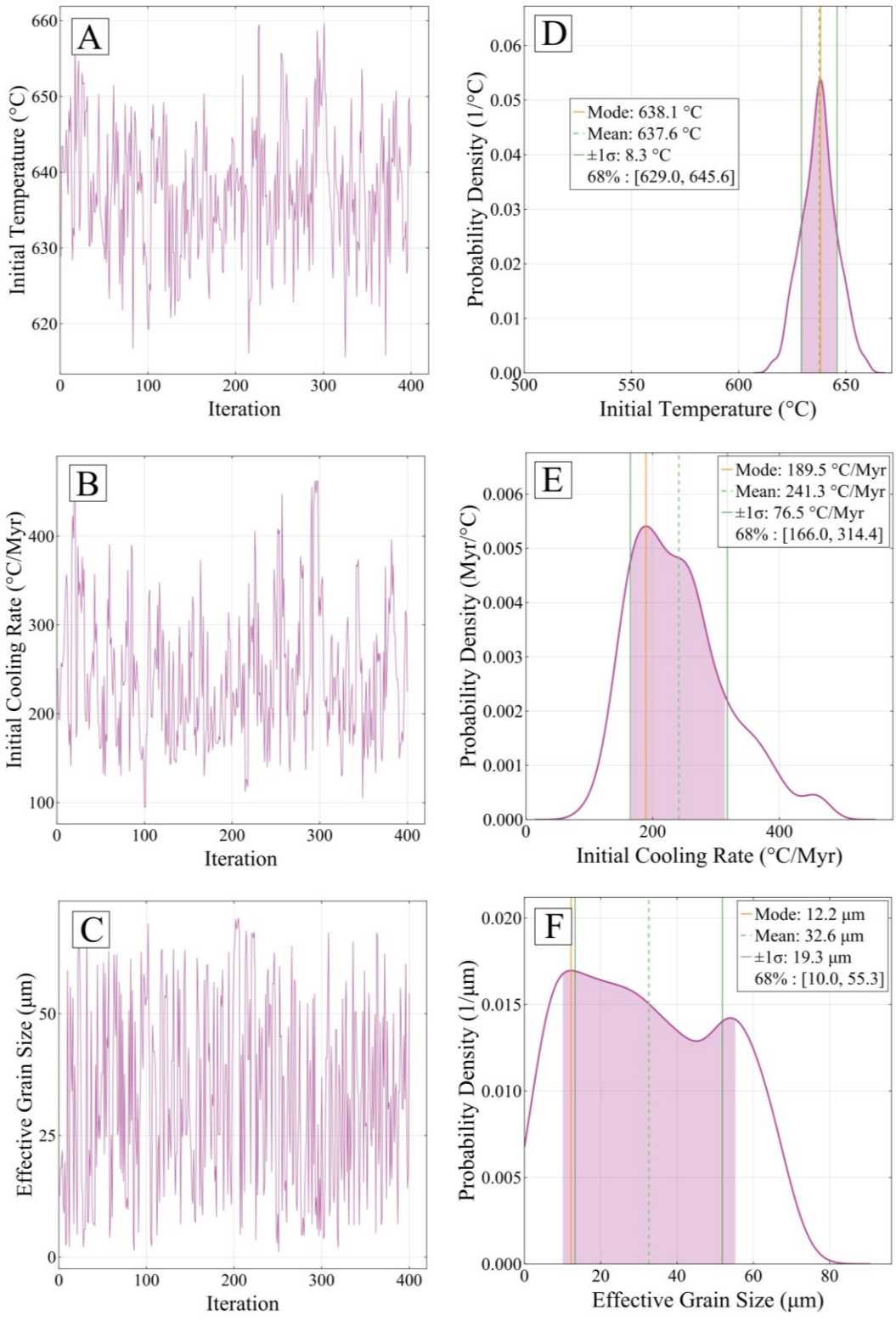

Figure 3.10: *Trace* plots (A, B) and *posterior* distributions (C, D) for initial cooling rate and temperature acquired using HMC for the joint parameter space of GDIFF and KADMOS. A cooling rate of 241.3 ± 76.5 °C/Myr is able to reproduce the entire petrological dataset for the Pindos metamorphic sole rocks.

3.5 Discussion

3.5.1 Hamiltonian Monte Carlo: a powerful tool in petrology

The vast majority of geoscientific problems require some form of inversion to extract meaningful parameters capable of explaining either experimental or natural observations. In many cases, the inversion is inherently complex because a large set of parameters must be constrained simultaneously (e.g., Baumann & Kaus, 2015). Specifically in the field of petrology, inversion is commonly needed to extract key properties from experimental data such as diffusion rates of trace and major elements in different kinds of minerals (e.g., Chakraborty & Ganguly, 1992; Cherniak et al., 2007; Müller et al., 2013). In other cases, such as the one presented here, inversion quantifies parameters that help elucidate natural processes and reveal broader geodynamic implications. Additionally, the field of petrology is experiencing rapid advancements in numerical and analytical methods which are accompanied by an increasing abundance of useful data. These developments create opportunities to explore and test more complex hypotheses based on physical models. Therefore, inversion algorithms capable of operating in increasingly high-dimensional spaces are required.

In this paper, we demonstrate how HMC is a powerful tool to perform inversion for diffusion models involving two and three invertible parameters. In all of the two-parameter test cases, HMC required substantially fewer model evaluations than a direct search approach with comparable resolution (Table 3.1). Each accepted sample in HMC is defined by heavier computations due to the need of gradient information (here performed with Automatic Differentiation). This made the HMC exploration in the two-parameter cases slower than direct search. We also notice that in cases such as GDIFF, in which the *posterior* distribution can be uniform, HMC requires many more total samples to converge towards the final uniform state. HMC can also face difficulties when the *posterior* distribution is highly curved or strongly multimodal (Betancourt, 2018). However, the uniform character of a probability distribution can already be identified with a relatively small number of samples by the presence of an extended typical set (i.e., the 68 % probability region). In cases such as KADMOS, where the *posterior* is Gaussian, HMC converges significantly faster. HMC can also be significantly faster if multiple chains are computed with parallel threading. The implementation of this capability is however left for future work.

The reduction of total model evaluations becomes significant as model complexity increases. For higher-dimensional inversions, the scaling advantage of HMC becomes pronounced. This is because the computational cost of a direct search approach grows exponentially with the number of parameters while HMC maintains efficient exploration by using gradient information to reach the *typical set* rapidly. This behavior is reflected in our three-dimensional test cases. In these experiments, sufficient exploration of the *typical set* was achieved in just 5.8 hours instead of the 44 hours needed based on direct search (KADMOS). To explore the *typical set* for three parameters using both KADMOS and GDIFF only 25.1 hours were needed. Another advantage of HMC is that it avoids drifting in random directions because of the gradient information. This is a common problem in algorithms such as the Random Walk Metropolis (Betancourt, 2018).

Table 3.1: Comparison of computation time and total number of model evaluations between the direct search approach and HMC. All computations were performed using a desktop computer with an AMD Ryzen 9 7900X 12-Core processor and 64 GB of RAM.

Numerical Model	**Considered Minerals**	**Number of parameters**	**Type of sampler**	**Computation Time (hours)**	**Model Evaluations**	**Number of HMC samples**
GDIFF	Grt7, Grt14 and Grt15	2	Direct Search	3.96	30,000	-
GDIFF	Grt7, Grt14 and Grt15	2	NUTS	20.02	8,732	600
KADMOS	Muscovite	2	Direct Search	0.23	10,000	-
KADMOS	Muscovite	2	NUTS	0.55	999	100
KADMOS	Muscovite	3	Direct Search	44.28	1,000,000	-
KADMOS	Muscovite	3	NUTS	5.78	9,541	600
KADMOS + GDIFF	Grt7, Grt14, Grt15 and Muscovite	3	NUTS	25.1	13,780	400

The ability of HMC to efficiently handle high-dimensional parameter spaces allows *posterior* distributions to be readily evaluated and visualized. Even in the two-parameter cases where HMC may be slower, it still offers important benefits. It provides a rigorous statistical basis for quantifying uncertainties. Importantly, this approach also enables the assignment of uniform *prior* distributions to poorly constrained parameters and allows their influence on the data fit

to be systematically evaluated. In our case, this is illustrated by the estimation of the effective grain size, which appears to have only a minor impact on the fit compared to the dominant control exerted by the initial cooling rate and equilibration temperature. Moreover, HMC algorithms such as the optimized NUTS are designed to eliminate the need for manual tuning. However, it must be stressed that the advantages of HMC heavily rely on the differentiability of the underlying numerical model. Despite these limitations, gradient-based inversion methods such as HMC drastically expand the range of problems that can be tackled in petrology. They enable the future integration of more complex thermomechanical or geodynamic models and open new opportunities to test scientific hypotheses. They finally allow the joint inversion and rigorous statistical quantification of different, independent physical systems in a simultaneous manner.

3.5.2 Geodynamic implications for the Pindos metamorphic sole

Our investigation reveals the importance of combining petrological data with multiple independent modeling approaches. One of the key findings in the present work is the independent agreement between the GDIFF modeling results, the $^{40}Ar/^{39}Ar$ apparent age modeling of muscovite, and previously published thermobarometric and geochronological data for the Pindos metamorphic sole (Moutzouris et al., 2025). In particular, Figure 3.4 shows that the observed garnet compositional profiles can only be reproduced if the investigated garnet-schist started cooling from ~630 °C. This temperature is in excellent agreement with the thermobarometric estimates of Moutzouris et al. (2025). Moreover, our joint inversion approach strongly suggests that an initial cooling rate of 241.3 ± 76.5 °C/Myr is able to simultaneously explain thermobarometry, the major-element zoning in garnet and the measured $^{40}Ar/^{39}Ar$ muscovite age. This result is consistent with cooling rates previously inferred from geochronological data for the Pindos metamorphic sole (Moutzouris et al., 2025). Similar agreement between garnet diffusion modeling and geochronological constrains has been documented for the Main Central Thrust in the Sikkim Himalaya (Burg & Moulas, 2022). Here, we demonstrate that integrating multiple, independently derived datasets reinforces the robustness of the inferred evolution of an investigated rock.

The calculated cooling rate of 241.3 ± 76.5 °C/Myr was acquired using an asymptotic temperature-time path. This kind of cooling path is considered reasonable for several reasons. The preservation of the sharp gradients in the slow diffusing grossular component in combination with the preservation of the fast diffusing Mg, Fe and Mn profiles is a strong indication of a short residence time at high-temperature conditions (e.g., Ague & Baxter, 2007).

An opposite scenario in which the rocks cool progressively faster towards the surface would translate into a long residence time at high-temperature conditions. This prolonged residence time would eliminate the sharp gradients of Ca and the diffusion profiles of Mg, Fe and Mn. In addition, such a scenario would lead to the relaxation of the residual pressure of quartz inclusions in garnet (Zhong et al., 2018, 2020). The chosen asymptotic path additionally agrees well with previous data from the Oman ophiolite (Hacker et al., 1996). It is further compatible with previous numerical work on metamorphic soles (Duretz et al., 2016; Ibragimov et al., 2024). These arguments along with the results presented in this work, strongly support that the attainment of peak conditions was followed by asymptotic rapid cooling with an initial cooling rate of 241.3 ± 76.5 °C/Myr.

The excessive values of inferred cooling rates, even though they are transient in character, require a physical mechanism in order to be explained. Based on our findings, two different scenarios can be considered. According to the first scenario, the metamorphic sole could be formed due to deep-burial metamorphism at depths exceeding 30 kms (Agard et al., 2016; Ambrose et al., 2021; Guilmette et al., 2018; Mulder et al., 2016; Searle & Cox, 1999; Searle et al., 2015). In this scenario, the inverted metamorphic gradients found in metamorphic soles along with the high temperatures of equilibration are explained by the existence of a hot overlying mantle wedge and due to conductive heat transport (Jamieson, 1986). The exhumation of the ophiolite, and therefore the metamorphic sole, in such a setting is usually thought to occur along the subduction interface and driven by buoyancy (e.g., Cowan et al., 2014). The second scenario postulates the significance of rapid metamorphism during incipient intra-oceanic thrusting (Duretz et al., 2016; Ibragimov et al., 2024). In this scenario, numerical modeling shows that the temperatures recorded by metamorphic soles can only be reached with the contribution of transient processes such as shear (frictional) heating and that the high-temperature conditions are a function of the shearing velocity and the thermomechanical properties of the materials involved. Additionally, in a scenario of shear heating, it has been found that the cessation of shearing is followed by rapid asymptotic cooling as shown by Burg & Moulas (2022). The metamorphic pressures of equilibration could be explained due to the localization of tectonic stresses (Brown, 2023; Moulas et al., 2013; Zuza et al., 2022). More evidence for this theory has lately been suggested for the Samail ophiolite (Garber et al., 2025; Ibragimov et al., 2024).

Finally, in addition to the aforementioned studies, new results by Tagliaferri et al. (2025) based on garnet diffusion modelling and thermokinematic models suggested that rocks directly

adjacent to a shear zone cool at approximately 200 °C/Myr once deformation ceases. This estimation is directly comparable with our results since the aforementioned authors emphasized the importance of rapid shearing and potential shear heating in producing initial cooling rates in high-grade metamorphic rocks. In light of these results, and given the consistency between our findings and previous studies, we support that the metamorphic sole of the Pindos ophiolite was strongly influenced by shear heating and formed during the initiation of intra-oceanic subduction.

3.6 Conclusions

In this work, we demonstrate that joint inversion of multiple, independent systems is essential for furthering our understanding of metamorphic processes. Our study used the Pindos metamorphic sole as an example for inversion. Garnet diffusion indicated an initial equilibration temperature of about 630 °C. This result agrees, in an independent manner, with previous thermobarometric estimates. An advantage of our approach is that when garnet diffusion is combined with diffusion modeling of Ar in muscovite, the calculation of the cooling rates and the associated uncertainties is feasible and computationally efficient. In particular, we found that a cooling rate of 241.3 ± 76.5 °C/Myr is able to reproduce the recently published data from Pindos ophiolite (Moutzouris et al. 2025). To conclude, we find that the most likely explanation for the high cooling rates at high temperatures is the cessation of shearing and the associated thermal relaxation. In the present study, we highlight the value of Hamiltonian Monte Carlo as an inversion method. We showed that Hamiltonian Monte Carlo is a powerful tool to explore the investigated parameter space and provide a rigorous statistical analysis and uncertainty assessment. We suggest Hamiltonian Monte Carlo as an additional tool for future petrological studies where many parameters need to be explored, which requires efficient algorithms where simpler direct search methods are computationally too expensive.

3.7 Supplementary material

3.7.1 Conservation of Hamiltonian energy

In time-evolving physical systems, the Hamiltonian energy can be a function of time (t), position ($\boldsymbol{\theta}(t)$), and momentum ($\boldsymbol{p}(t)$). To keep the analogy between physical systems and inverse modelling, we note that the position vector corresponds to the vector of inverted parameters (θ_i) and the momentum vector corresponds to the vector of artificial momenta (p_i). For cases where the Hamiltonian energy ($H(t, \boldsymbol{\theta}(t), \boldsymbol{p}(t))$) does not explicitly depend on time we have:

$$\frac{\partial H}{\partial t} = 0 \tag{A1}$$

Equation $(A1)$ has important consequences for the conservation of the total energy in mechanical systems. Following Arnold (1974, p. 67), we can write the general equation for the time derivative of the Hamiltonian $(H(t, \boldsymbol{\theta}(t), \boldsymbol{p}(t)))$ as follows:

$$\frac{dH}{dt} = \frac{\partial H}{\partial t} + \sum_{j=1}^{k} \left[\frac{\partial H}{\partial \theta_i} \frac{d\theta_i}{dt} + \frac{\partial H}{\partial p_i} \frac{dp_i}{dt} \right] \tag{A2}$$

For the cases where equation $(A1)$ holds, and by substituting the canonical equations (eqs 3.2 and 3.3 in the main text), equation $(A2)$ becomes:

$$\frac{dH(\boldsymbol{\theta}, \boldsymbol{p})}{dt} = \sum_{j=1}^{k} \left[-\frac{\partial H(\boldsymbol{\theta}, \boldsymbol{p})}{\partial \theta_i} \frac{\partial H(\boldsymbol{\theta}, \boldsymbol{p})}{\partial p_i} + \frac{\partial H(\boldsymbol{\theta}, \boldsymbol{p})}{\partial p_i} \frac{\partial H(\boldsymbol{\theta}, \boldsymbol{p})}{\partial \theta_i} \right] = 0 \tag{A3}$$

where we have emphasized that $H(\boldsymbol{\theta}, \boldsymbol{p})$ is not an explicit function of time even though $\boldsymbol{\theta}(t)$ and $\boldsymbol{p}(t)$ change in time. The last result shows that $H(\boldsymbol{\theta}, \boldsymbol{p})$ does not change in time and therefore, the Hamiltonian is conserved.

3.7.2 HMC with the Bayesian approach

This section provides clarifications on the concepts behind the Bayesian approach of HMC that may be useful for the reader to understand the analogies between the two different available approaches (misfit and Bayesian formulation). In methods such as HMC, the variables $\boldsymbol{\theta}$ and $\boldsymbol{p}$ are treated as independent and therefore their joint probability distribution can be expressed as (e.g., Betancourt, 2018):

$$\Pi(\boldsymbol{\theta}, \boldsymbol{p}) = \Pi'(\boldsymbol{\theta}) \Pi(\boldsymbol{p}) \tag{B1}$$

where $\Pi'(\boldsymbol{\theta})$ is the total probability of observing $\boldsymbol{\theta}$ and $\Pi(\boldsymbol{p})$ is the total probability of observing $\boldsymbol{p}$. In the literature, $\Pi'(\boldsymbol{\theta})$ is often referred to as the *target* probability. Equation $(B1)$ shows that the total probability of a system with $\boldsymbol{\theta}$ and $\boldsymbol{p}$ can be calculated if we multiply the independent probabilities of $\boldsymbol{\theta}$ and $\boldsymbol{p}$. In the statistical application of HMC, we require some formulation that connects this joint probability of the variables with the Hamiltonian energy. This is done by borrowing concepts from statistical mechanics and expressing the joint probability as:

$$\Pi(\boldsymbol{\theta}, \boldsymbol{p}) \propto \exp\left(-H(\boldsymbol{\theta}, \boldsymbol{p})\right) \tag{B2}$$

Equation $(B2)$ represents a Boltzmann distribution which shows that the total probability of a state $\Pi(\boldsymbol{\theta},\boldsymbol{p})$, that is described by $\boldsymbol{\theta}$ and $\boldsymbol{p}$, is proportional to the Hamiltonian energy. Equation $(B2)$ expresses the fact that configurations with lower (Hamiltonian) energies are more probable to occur. Replacing $H(\boldsymbol{\theta},\boldsymbol{p})$ from equation (3.1) in the main text into equation $(B2)$ results to:

$$\Pi(\boldsymbol{\theta},\boldsymbol{p}) \propto \exp\big(-H(\boldsymbol{\theta},\boldsymbol{p})\big) = \exp\big(-V(\boldsymbol{\theta})\big)\exp\big(-T(\boldsymbol{p})\big) \qquad (B3)$$

Direct comparison between equations $(B1)$ and $(B3)$ reveals the following relation:

$$\Pi'(\boldsymbol{\theta})\Pi(\boldsymbol{p}) \propto \exp\big(-V(\boldsymbol{\theta})\big)\exp\big(-T(\boldsymbol{p})\big)$$

which in turn shows that:

$$\Pi'(\boldsymbol{\theta}) \propto \exp\big(-V(\boldsymbol{\theta})\big)$$

$$\Pi(\boldsymbol{p}) \propto \exp\big(-T(\boldsymbol{p})\big) \qquad (B4)$$

Equation $(B4)$ describes the independent probability distributions of $\boldsymbol{\theta}$ and $\boldsymbol{p}$ as Boltzmann distributions. Then, in Bayesian HMC approaches, the potential energy is chosen in the following way (e.g., Neal, 2011):

$$V(\boldsymbol{\theta}) = -\log\left[\Pi(\boldsymbol{\theta}|\boldsymbol{F^{obs}})\right] \qquad (B5)$$

where $\Pi(\boldsymbol{\theta}|\boldsymbol{F^{obs}})$ is the conditional probability of observing the parameters $\boldsymbol{\theta}$ given that we know the observed data $\boldsymbol{F^{obs}}$ and log represents the natural logarithm. $\Pi(\boldsymbol{\theta}|\boldsymbol{F^{obs}})$ is also referred to as the *posterior* probability in the literature. Due to this particular choice of potential energy, we can substitute $(B5)$ in $(B4)$ in order to eliminate $V(\boldsymbol{\theta})$. The result shows that:

$$\Pi'(\boldsymbol{\theta}) \propto \Pi\big(\boldsymbol{\theta}\big|\boldsymbol{F^{obs}}\big) \qquad (B6)$$

Therefore, this exact choice of potential energy makes the *target* distribution directly related to the *posterior* distribution without explicit normalization factors.

The *posterior* probability can be further calculated with Bayes' theorem. If we neglect the effect of the marginal probability of observing $\boldsymbol{F^{obs}}$ (e.g., Bailer-Jones, 2017, p. 64), then the unnormalized posterior probability can be written in the following way:

$$\Pi\big(\boldsymbol{\theta}|\boldsymbol{F^{obs}}\big) = \mathcal{L}\big(\boldsymbol{F^{obs}}|\boldsymbol{\theta}\big)\Pi(\boldsymbol{\theta}) \qquad (B7)$$

where $\mathcal{L}(\boldsymbol{F^{obs}}|\boldsymbol{\theta})$ is the *likelihood* and $\Pi(\boldsymbol{\theta})$ is the *prior* distribution (see main text). Now it is possible to substitute equation $(B7)$ into equation $(B5)$:

$$V(\boldsymbol{\theta}) = -\log\left[\mathcal{L}(\boldsymbol{F^{obs}}|\boldsymbol{\theta})\Pi(\boldsymbol{\theta})\right] \quad (B8)$$

For kinetic energy, the same definition is used as in equation (3.5) of the main text. By substituting equation (3.5) from the main text into equation $(B4)$ we see that:

$$\Pi(\boldsymbol{p}) \propto \exp\left(-\frac{1}{2}\boldsymbol{p}^T\boldsymbol{M}^{-1}\boldsymbol{p}\right) \quad (B9)$$

Equation $(B9)$ shows that the momenta $\boldsymbol{p}$ are simply described by a Gaussian distribution. This distribution is easily sampled from and has well-known analytical derivatives which help the efficiency of the algorithm.

Finally, if the kinetic and potential energy are substituted into the Hamiltonian energy (eq 1 in the main text), we end up with the equation that most Bayesian HMC approaches use:

$$H(\boldsymbol{\theta},\boldsymbol{p}) = \frac{1}{2}\boldsymbol{p}^T\boldsymbol{M}^{-1}\boldsymbol{p} - \log\left[\mathcal{L}(\boldsymbol{F^{obs}}|\boldsymbol{\theta})\Pi(\boldsymbol{\theta})\right]$$

3.7.3 The HMC algorithm in five steps

The following section is presenting the standard HMC algorithm shown in Betancourt (2018) and Neal (2011) but offers additional clarity for readers interested in the application of HMC.

Step 1: During the initial step, a sample $\boldsymbol{\theta_{current}}$ (the invertible parameters in the main text) is drawn based on the prior distribution $\Pi(\boldsymbol{\theta})$. The prior distribution represents prior beliefs about the parameter based on existing knowledge. In the absence of such knowledge, a more diffused or non-informative prior is typically chosen to represent greater uncertainty.

Step 2: A sample for $\boldsymbol{p_{current}}$ is randomly drawn from a normal distribution $\mathcal{N}(0,\boldsymbol{M})$ where 0 denotes the mean value and $\boldsymbol{M}$ represents the variance or covariance matrix of momenta.

Step 3: Based on $\boldsymbol{\theta_{current}}$ and $\boldsymbol{p_{current}}$, the Hamiltonian dynamics are simulated by numerically solving the *canonical equations* (eqs 3.7 and 3.8 of the main text) for n_t steps and a step size of Δt. This step of the algorithm is deterministic. However, all numerical discretization methods that solve the *canonical equations* introduce some degree of error, which can result in either an artificial gain or loss of Hamiltonian energy over time (e.g., Fichtner et al., 2021; their Appendix C). Among the various explicit numerical algorithms, the

leapfrog algorithm, has been proven to be particularly effective and widely used for solving the Hamiltonian equations (Mikkola & Tanikawa, 1999; Yoshida, 1990). A key consideration in implementing the *leapfrog* method is the careful selection of n_t and Δt. These parameters must be chosen in such a way to ensure both the efficient exploration of the Hamiltonian trajectory and the stability of the numerical integration scheme (Betancourt et al., 2015; Fichtner et al., 2021; Neal, 2011). After simulating a Hamiltonian trajectory for n_t steps, the system makes a large jump using the gradient information and reaches a new state characterized by $\boldsymbol{\theta_{new}}$ and $\boldsymbol{p_{new}}$.

Step 4: The next part of the algorithm determines if the new state will be accepted or not. It is common that, after simulating a single trajectory of Hamiltonian dynamics, the numerical integration leads to a Hamiltonian value different from the initial one. As a result, the joint total probability may change not because of physical reasons but because of the numerical implementation. This can introduce bias in the sampling. Therefore, a correction mechanism is required to prevent this bias. First, the new vector of momenta is negated from $\boldsymbol{p_{new}}$ to $-\boldsymbol{p_{new}}$. Then, the Hamiltonian energy for the current step $H(\boldsymbol{\theta_{current}}, \boldsymbol{p_{current}})$ and the new step $H(\boldsymbol{\theta_{new}}, -\boldsymbol{p_{new}})$ are computed. Then the new state is accepted with probability:

$$\alpha = min(1, exp[H(\boldsymbol{\theta_{current}}, \boldsymbol{p_{current}}) - H(\boldsymbol{\theta_{new}}, -\boldsymbol{p_{new}})]) \qquad (C1)$$

Equation $(C1)$ is also referred to as the Metropolis criterion. It constitutes a simplification of the Metropolis-Hastings criterion (Hastings, 1970; Metropolis et al., 1953). If the Hamiltonian energy remains exactly conserved during numerical integration, then the exponential term of equation $(C1)$ equals 1 and the new state is accepted with probability 1 (i.e., 100%). If the numerical implementation introduces errors such that $H(\boldsymbol{\theta_{new}}, -\boldsymbol{p_{new}}) > H(\boldsymbol{\theta_{current}}, \boldsymbol{p_{current}})$, this implies a violation of energy conservation. In this case, the exponential term becomes less than 1 and the new state is accepted with probability less than 1. During this step, it is crucial to negate the momentum vector. The negation is permitted due to the reversibility of Hamiltonian dynamics but is also essential. Without it, the Metropolis acceptance criterion would always evaluate to zero and no sample updates could be accepted (see Betancourt, 2018; section 5.2).

It is also important to note that the Hamiltonian dynamics are volume-preserving (Liouville's theorem). This means that any region R in *phase space* will preserve its volume after a transformation due to Hamiltonian dynamics, which is equal to the preservation of the total probability distribution. If this was not the case, a Metropolis-Hastings criterion would be

required instead. The Metropolis-Hastings criterion considers the effect of volume transformations of the *phase space* that can effectively change the probability distributions. In a non-volume preserving scenario the determinant of the Jacobian matrix of the mapping between the current and new state would be required to track how the probability densities change due to the transformation of the *phase space* (e.g., Eidsvik & Tjelmeland, 2006).

Step 5: If the proposed state is rejected, the sampler retains the current position $\boldsymbol{\theta_{current}}$ and a new momentum is randomly drawn from the Gaussian distribution $\mathcal{N}(0, \boldsymbol{M})$. If the proposed state is accepted, the sampler proceeds from $\boldsymbol{\theta_{new}}$. During the next iteration, a new momentum $\boldsymbol{p'_{new}}$ from a normal distribution $\mathcal{N}(0, \boldsymbol{M})$ is sampled. Steps (2) through (5) are then repeated, allowing the algorithm to make large jumps in the *typical set* and efficiently explore it. The random choice of momenta in HMC corresponds to the stochastic nature of the algorithm.

The large parameter jumps, driven by the canonical equations in *Step 3*, help HMC escape local minima and reach unexplored areas of the *typical set* quickly. Furthermore, the formulation of the kinetic energy, which is inspired by physical systems, ensures conservation of Hamiltonian energy and non-dissipative behaviour towards the *mode*. Finally, stochastic (random) transitions between different Hamiltonian energy level sets enable the sampler to explore a broader range of acceptable fit magnitudes while avoiding the *mode* but also areas of bad fits.

3.7.4 GDIFF

GDIFF (Moulas, 2023) is a Finite Difference (FD) numerical code used to calculate the concentration profiles of garnet in one dimension. In multicomponent diffusion, the concentration profile of each endmember depends on the composition gradients of the other endmembers. This behavior is described by the multicomponent diffusion equation:

$$\frac{\partial C_i}{\partial t} = \frac{1}{x^{n-1}} \frac{\partial}{\partial x}\left(x^{n-1} D_{ij} \frac{\partial C_j}{\partial x} \right) \qquad (D1)$$

where x is the spatial coordinate, t is time, C is the mole fraction concentration, i and j are indices representing the independent endmembers, n is an integer that can be used to specify the geometry of the mineral and D_{ij} is the diffusivity matrix that accounts for the coupling between them. The diffusivity matrix is composition-dependent and is calculated following the approach of Lasaga (1979):

$$D_{ij} = D_i^* \delta_{ij} - \frac{D_i^* X_i}{\sum_{k=1}^{4} D_k^* X_k} (D_j^* - D_4^*) \qquad (D2)$$

where D_i^* is the tracer-diffusion coefficient of each endmember, δ_{ij} is the Kronecker delta and X_i represents the mole fractions of each endmember. Tracer diffusivity coefficients are taken from Chakraborty & Ganguly (1992) and follow an Arrhenius relationship making them temperature- and pressure-dependent.

Equation $(D1)$ is solved on a regularly spaced grid using an implicit, conservative scheme. Because diffusivities depend on composition and vary with space, Picard iterations are used to achieve numerical convergence, with a tolerance threshold of 10^{-5}. This makes the problem non-linear. The equations are discretized and written in a matrix-vector form as:

$$\boldsymbol{A}(\boldsymbol{x}^{m-1})\boldsymbol{x}^m = \boldsymbol{b} \qquad (D3)$$

In this form, $\boldsymbol{A}$ contains the coefficients of the unknowns, $\boldsymbol{x}$ is the vector of unknown concentrations, m is the Picard iteration number and $\boldsymbol{b}$ is the right-hand side vector built from the previous physical timestep. For more details refer to Moulas (2023).

3.7.5 KADMOS

KADMOS (Moulas & Brandon, 2022) is a Finite Element (FE) numerical code used to model the apparent $^{40}K/^{40}Ar$ ages and the associated $^{40}Ar/^{39}Ar$ ages of different minerals for a given *P-T-t* path. KADMOS is solving the diffusion equation with a source term to account for the production of radiogenic ^{40}Ar. The main equation that is solved is:

$$x^{n-1} \frac{\partial}{\partial t}\left(\frac{Ar}{K_0}\right) = \frac{\partial}{\partial x}\left[x^{n-1} D \frac{\partial}{\partial x}\left(\frac{Ar}{K_0}\right)\right] + x^{n-1} \lambda_{Ar} e^{-\lambda_T t} \qquad (E1)$$

where x represents the spatial coordinate, n is an integer specifying the geometry of the mineral, Ar represents the radiogenic argon produced from the decay of potassium, K_0 is the initial amount of ^{40}K, D is the diffusion coefficient that is independent of concentration, λ_{Ar} is the decay constant of ^{40}K to ^{40}Ar $(0.581 \cdot 10^{-10}\ yrs)$, λ_T is the total decay constant of ^{40}K $(5.543 \cdot 10^{-10}\ yrs)$ and t is time. The second term of the right-hand side of equation $(E1)$ corresponds to the accumulation of radiogenic argon with time while the rest of the equation is responsible for the diffusion of argon in the mineral with time. Therefore, the simulations of KADMOS start from the formation of the mineral at $t = 0$ until a total time with a *P-T-t* path that can be specified from the user.

For the discretization of equation $(E1)$ a Galerkin approach is used. Also, linear shape functions in a global coordinate scope are adopted. The discretized form of equation $(E1)$ is as follows:

$$\boldsymbol{KM}\{C_i^j\} = \boldsymbol{R} \qquad (E2)$$

where $\boldsymbol{KM}$ is the global left-hand side matrix, $\boldsymbol{R}$ is the global right-hand side vector and C_i^j represents the unknowns (degrees of freedom) at point i and time j. The global matrices are assembled by combining the local matrices that correspond to each element. KADMOS assumes that ^{40}Ar leaves at the outer boundary of a crystal. This imposes a large compositional gradient that might lead to numerical instability. To overcome this problem, KADMOS utilizes an adaptive grid that resolves large gradients in detail. For a detailed description of the numerical implementation and theory refer to Moulas & Brandon (2022).

3.7.6 Supplementary Figures

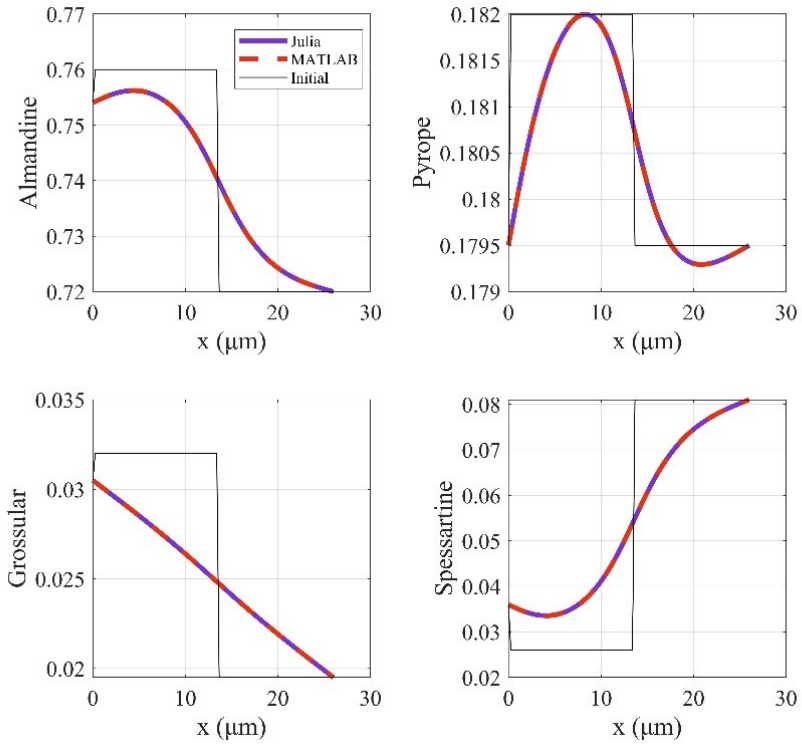

Figure S. 3.1: Compositional profiles of garnet demonstrating agreement between the MATLAB and Julia implementation of GDIFF. The same numerical and physical parameters have been used.

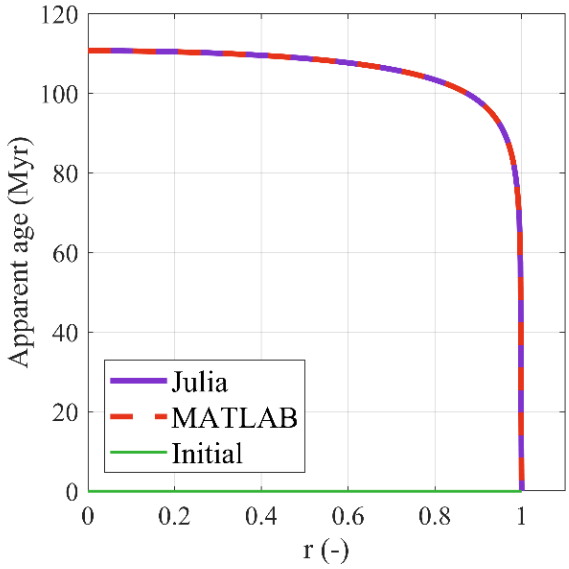

Figure S. 3.2: Apparent age profile demonstrating agreement between the MATLAB and Julia implementation of KADMOS. The same numerical and physical parameters have been used.

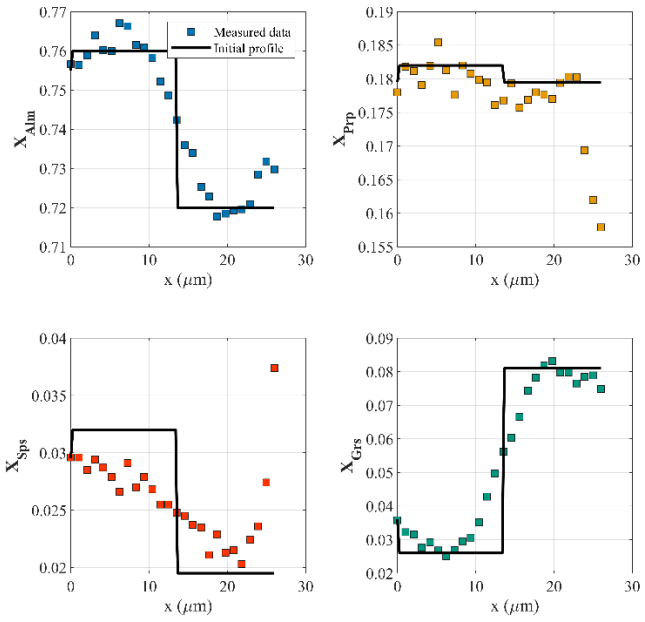

Figure S. 3.3: Measured compositional profiles of Grt7 (squares) and initial conditions (black lines) used for the evaluation of GDIFF models.

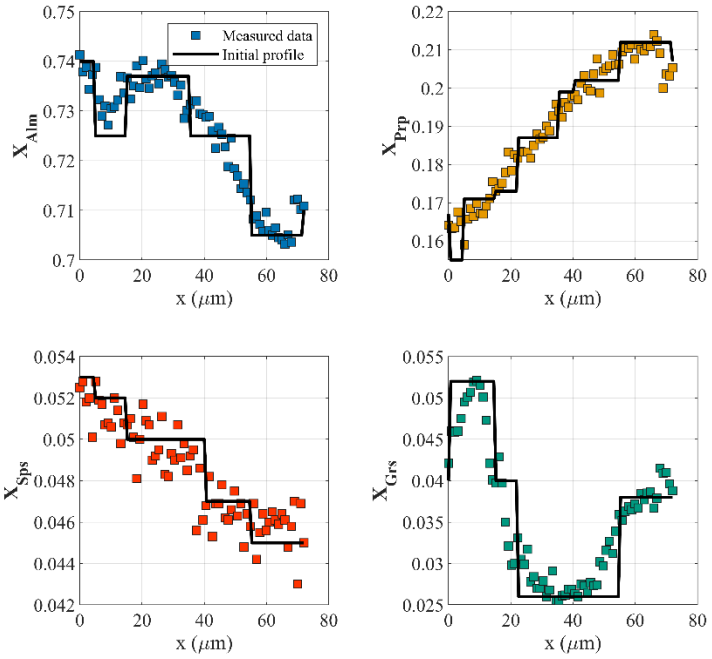

Figure S. 3.4: Measured compositional profiles of Grt15 (squares) and initial conditions (black lines) used for the evaluation of GDIFF models.

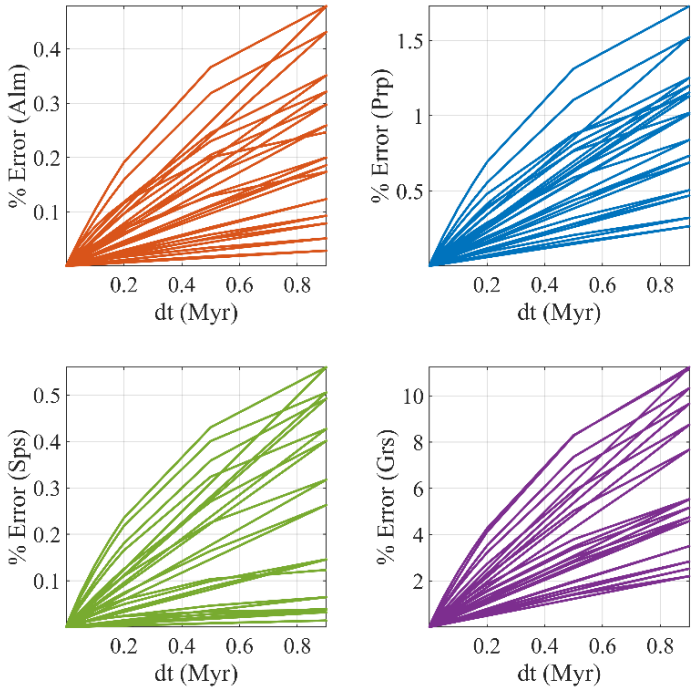

Figure S. 3.5: Plots showing the percentage of error generated for each modeled endmember of garnet with GDIFF for different numerical timesteps (dt). Different cooling rates and initial

temperatures were tested spanning the investigated range. A timestep of 0.02 Myr was chosen as it produces errors well-below 1%.

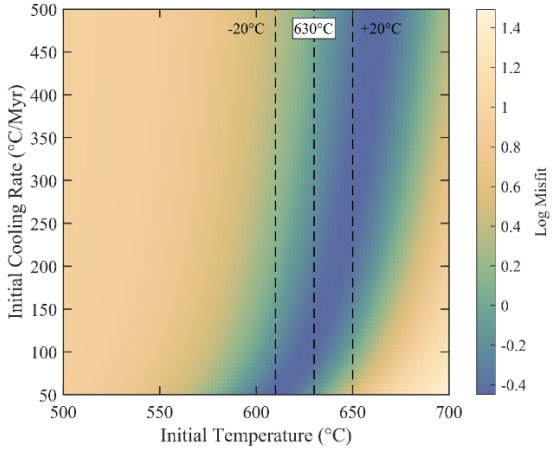

Figure S. 3.6: Misfit map for all considered combinations of initial temperature and initial cooling rate using GDIFF. The misfit quantifies the difference between modeled and measured garnet compositions. This misfit map was constructed by assuming that the grossular component is ten times more important than the other three components.

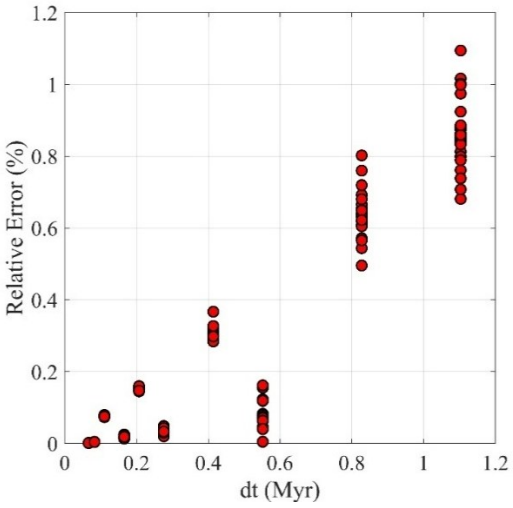

Figure S. 3.7: Plot representing the relative percentage of error generated using different timesteps in KADMOS. Different cooling rates and initial temperatures were tested spanning the entire investigated range. A timestep of 0.27 Myr was chosen as it produces errors well-below 1%.

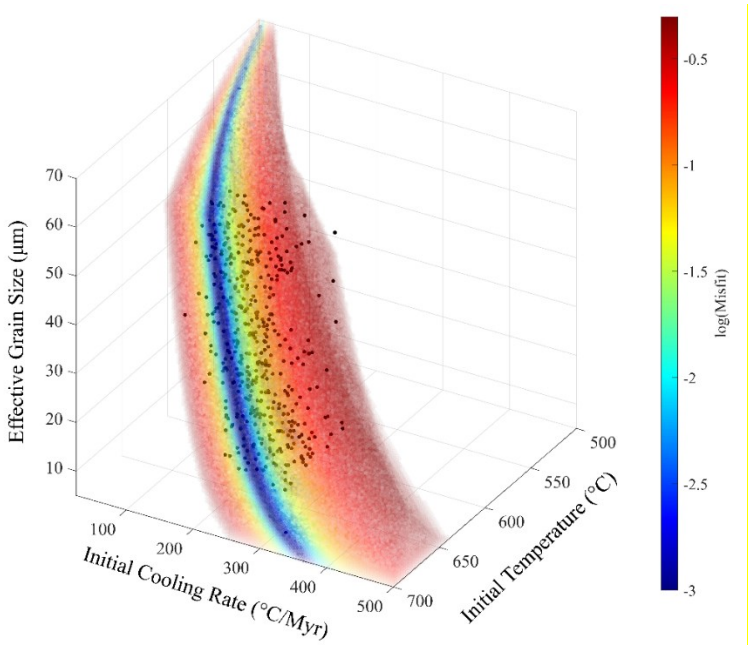

Figure S. 3.8: Direct search results for a three-dimensional case using KADMOS. The misfit quantifies the difference between modeled and measured muscovite age. Misfits with values lower than 0.6 Myr are plotted here. The black dots represent the samples drawn from HMC (see main text for more details). A clear zone of low misfits is indicated showing how the effective grain size has not a significant effect on the measured age.

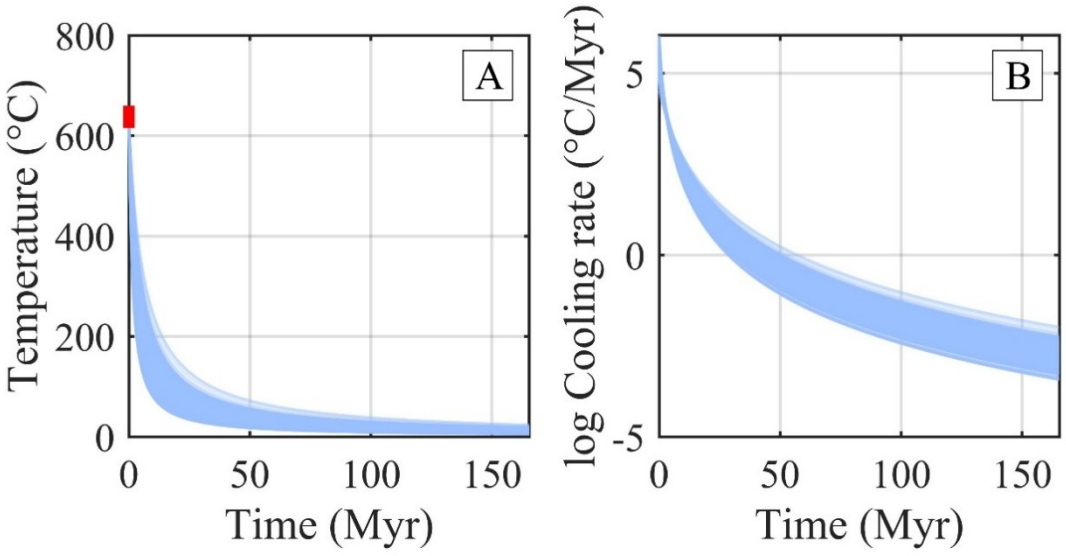

Figure S. 3.9: (A) Time-temperature diagram illustrating the cooling paths corresponding to the accepted initial cooling rates and initial temperatures derived from the HMC analysis. The thick red band denotes the range of accepted initial equilibration temperatures. (B) Cooling rate evolution for each of the accepted cooling paths

3.8 Data availability

The codes developed in the present study and supplementary figures are publicly available and can be downloaded from https://doi.org/10.5281/zenodo.18247900

3.9 Funding

E. Moulas and D. Moutzouris would like to acknowledge the German Research Foundation for financial support (DFG; project number 512790090). S. Schorn acknowledges the Alexander von Humboldt Foundation for support.

3.10 References

Agard, P., Yamato, P., Soret, M., Prigent, C., Guillot, S., Plunder, A., Dubacq, B., Chauvet, A., & Monié, P. (2016). Plate interface rheological switches during subduction infancy: Control on slab penetration and metamorphic sole formation. Earth and Planetary Science Letters, 451, 208–220. https://doi.org/10.1016/j.epsl.2016.06.054

Ague, J. J., & Baxter, E. F. (2007). Brief thermal pulses during mountain building recorded by Sr diffusion in apatite and multicomponent diffusion in garnet. Earth and Planetary Science Letters, 261(3–4), 500–516. https://doi.org/10.1016/j.epsl.2007.07.017

Ambrose, T. K., Waters, D. J., Searle, M. P., Gopon, P., & Forshaw, J. B. (2021). Burial, Accretion, and Exhumation of the Metamorphic Sole of the Oman-UAE Ophiolite. Tectonics, 40(4), e2020TC006392. https://doi.org/10.1029/2020TC006392

Arnold, V. I. (1974). Mathematical Methods of Classical Mechanics (Second, Vol. 60). Springer.

Bailer-Jones, C. A. L. (2017). Practical Bayesian Inference: A Primer for Physical Scientists. In Practical Bayesian Inference (1st ed.). Cambridge University Press. https://doi.org/10.1017/9781108123891.001

Batanova, V. G., Sobolev, A. V., & Magnin, V. (2018). Trace element analysis by EPMA in geosciences: Detection limit, precision and accuracy. IOP Conference Series: Materials Science and Engineering, 304, 012001. https://doi.org/10.1088/1757-899x/304/1/012001

Baumann, T. S., & Kaus, B. J. P. (2015). Geodynamic inversion to constrain the non-linear rheology of the lithosphere. Geophysical Journal International, 202(2), 1289–1316. https://doi.org/10.1093/gji/ggv201

Betancourt, M. J., Byrne, S., & Girolami, M. (2015). Optimizing The Integrator Step Size for Hamiltonian Monte Carlo (No. arXiv:1411.6669). arXiv. https://doi.org/10.48550/arXiv.1411.6669

Betancourt, M. (2018). A Conceptual Introduction to Hamiltonian Monte Carlo (No. arXiv:1701.02434). arXiv. https://doi.org/10.48550/arXiv.1701.02434

Bezanson, J., Edelman, A., Karpinski, S., & Shah, V. B. (2017). Julia: A Fresh Approach to Numerical Computing. SIAM Review, 59(1), 65–98. https://doi.org/10.1137/141000671

Brown, M. (2023). Some thoughts about eclogites and related rocks. European Journal of Mineralogy, 35(4), 523–547. https://doi.org/10.5194/ejm-35-523-2023

Burg, J.-P., & Moulas, E. (2022). Cooling-rate constraints from metapelites across two inverted metamorphic sequences of the Alpine-Himalayan belt; evidence for viscous heating. Journal of Structural Geology, 156, 104536. https://doi.org/10.1016/j.jsg.2022.104536

Carpenter, B., Gelman, A., Hoffman, M. D., Lee, D., Goodrich, B., Betancourt, M., Brubaker, M., Guo, J., Li, P., & Riddell, A. (2017). Stan: A Probabilistic Programming Language. Journal of Statistical Software, 76(1). https://doi.org/10.18637/jss.v076.i01

Chakraborty, S., & Ganguly, J. (1992). Cation diffusion in aluminosilicate garnets: Experimental determination in spessartine-almandine diffusion couples, evaluation of effective binary diffusion coefficients, and applications. Contributions to Mineralogy and Petrology, 111(1), 74–86. https://doi.org/10.1007/BF00296579

Cheng, H., Bloch, E. M., Moulas, E., & Vervoort, J. D. (2020). Reconciliation of discrepant U–Pb, Lu–Hf, Sm–Nd, Ar–Ar and U–Th/He dates in an amphibolite from the Cathaysia Block in Southern China. Contributions to Mineralogy and Petrology, 175(1), 4. https://doi.org/10.1007/s00410-019-1644-9

Cherniak, D. J., Watson, E. B., & Wark, D. A. (2007). Ti diffusion in quartz. Chemical Geology, 236(1–2), 65–74. https://doi.org/10.1016/j.chemgeo.2006.09.001

Costa, F., Shea, T., & Ubide, T. (2020). Diffusion chronometry and the timescales of magmatic processes. Nature Reviews Earth & Environment, 1(4), 201–214. https://doi.org/10.1038/s43017-020-0038-x

Cowan, R. J., Searle, M. P., & Waters, D. J. (2014). Structure of the metamorphic sole to the Oman Ophiolite, Sumeini Window and Wadi Tayyin: Implications for ophiolite obduction processes. Geological Society, London, Special Publications, 392(1), 155–175. https://doi.org/10.1144/SP392.8

De Lima, P. D. S., Ferreira, M. S., Corso, G., & De Araújo, J. M. (2024). Bayesian time-lapse full waveform inversion using Hamiltonian Monte Carlo. Geophysical Prospecting, 72(9), 3381–3398. https://doi.org/10.1111/1365-2478.13604

Duane, S., Kennedy, A. D., Pendleton, B. J., & Roweth, D. (1987). Hybrid Monte Carlo. Physics Letters B, 195(2), 216–222. https://doi.org/10.1016/0370-2693(87)91197-X

Duretz, T., Agard, P., Yamato, P., Ducassou, C., Burov, E. B., & Gerya, T. V. (2016). Thermo-mechanical modeling of the obduction process based on the Oman Ophiolite case. Gondwana Research, 32, 1–10. https://doi.org/10.1016/j.gr.2015.02.002

Eidsvik, J., & Tjelmeland, H. (2006). On directional Metropolis–Hastings algorithms. Statistics and Computing, 16(1), 93–106. https://doi.org/10.1007/s11222-006-5536-2

Faryad, S. W., & Chakraborty, S. (2005). Duration of Eo-Alpine metamorphic events obtained from multicomponent diffusion modeling of garnet: A case study from the Eastern Alps. Contributions to Mineralogy and Petrology, 150(3), 306–318. https://doi.org/10.1007/s00410-005-0020-0

Fichtner, A., & Zunino, A. (2019). Hamiltonian Nullspace Shuttles. Geophysical Research Letters, 46(2), 644–651. https://doi.org/10.1029/2018gl080931

Fichtner, A., Zunino, A., Gebraad, L., & Boehm, C. (2021). Autotuning Hamiltonian Monte Carlo for efficient generalized nullspace exploration. Geophysical Journal International, 227(2), 941–968. https://doi.org/10.1093/gji/ggab270

Fjelde, T. E., Xu, K., Widmann, D., Tarek, M., Pfiffer, C., Trapp, M., Axen, S. D., Sun, X., Hauru, M., Yong, P., Tebbutt, W., Ghahramani, Z., & Ge, H. (2025). Turing.jl: A general-purpose probabilistic programming language. ACM Transactions on Probabilistic Machine Learning. https://doi.org/10.1145/3711897

Garber, J. M., Rioux, M., Smye, A. J., Cruz-Uribe, A. M., Baker, P. L., Vervoort, J. D., Searle, M. P., & Feineman, M. D. (2025). Shear heating during rapid subduction initiation beneath the Samail Ophiolite. Nature Geoscience, 18, 653–660. https://doi.org/10.1038/s41561-025-01711-6

Ge, H., Xu, K., & Ghahramani, Z. (2018). Turing: A language for flexible probabilistic inference. Proceedings of the 21st International Conference on Artifcial Intelligence and Statistics, 84.

Gebraad, L., Boehm, C., & Fichtner, A. (2020). Bayesian Elastic Full-Waveform Inversion Using Hamiltonian Monte Carlo. Journal of Geophysical Research: Solid Earth, 125(3), e2019JB018428. https://doi.org/10.1029/2019JB018428

Girolami, M., & Calderhead, B. (2011). Riemann Manifold Langevin and Hamiltonian Monte Carlo Methods. Journal of the Royal Statistical Society Series B: Statistical Methodology, 73(2), 123–214. https://doi.org/10.1111/j.1467-9868.2010.00765.x

Guilmette, C., Smit, M. A., Van Hinsbergen, D. J. J., Gürer, D., Corfu, F., Charette, B., Maffione, M., Rabeau, O., & Savard, D. (2018). Forced subduction initiation recorded in the sole and crust of the Semail Ophiolite of Oman. Nature Geoscience, 11(9), 688–695. https://doi.org/10.1038/s41561-018-0209-2

Hacker, B. R., Mosenfelder, J. L., & Gnos, E. (1996). Rapid emplacement of the Oman ophiolite: Thermal and geochronologic constraints. Tectonics, 15(6), 1230–1247. https://doi.org/10.1029/96TC01973

Hajian, A. (2007). Efficient cosmological parameter estimation with Hamiltonian Monte Carlo technique. Physical Review D, 75(8). https://doi.org/10.1103/physrevd.75.083525

Harrison, T. M., Célérier, J., Aikman, A. B., Hermann, J., & Heizler, M. T. (2009). Diffusion of 40Ar in muscovite. Geochimica et Cosmochimica Acta, 73(4), 1039–1051. https://doi.org/10.1016/j.gca.2008.09.038

Hastings, W. K. (1970). Monte Carlo sampling methods using Markov chains and their applications. Biometrika, 57(1), 97–109. https://doi.org/10.1093/biomet/57.1.97

Hoffman, M. D., & Gelman, A. (2014). The No-U-Turn Sampler: Adaptively Setting Path Lengths in Hamiltonian Monte Carlo. Journal of Machine Learning Research, 15, 593–1623.

Ibragimov, I., Kiss, D., & Moulas, E. (2024). A thermo-mechanical model of the thermal evolution and incorporation of metamorphic soles in Tethyan ophiolites: A case study from Oman. Austrian Journal of Earth Sciences, 117(1), 13–24. https://doi.org/10.17738/ajes.2024.0002

Jamieson, R. A. (1986). P-T paths from high temperature shear zones beneath ophiolites. Journal of Metamorphic Geology, 4(1), 3–22. https://doi.org/10.1111/j.1525-1314.1986.tb00335.x

Kabanikhin, S. I. (2008). Definitions and examples of inverse and ill-posed problems. Journal of Inverse and Ill-Posed Problems, 16(4). https://doi.org/10.1515/jiip.2008.019

Kelley, S. (2002). K-Ar and Ar-Ar Dating. Reviews in Mineralogy and Geochemistry, 47(1), 785–818. https://doi.org/10.2138/rmg.2002.47.17

Kent, A. J. R., Hutcheon, I. D., Ryerson, F. J., & Phinney, D. L. (2001). The temperature of formation of carbonate in martian meteorite ALH84001: Constraints from cation

diffusion. Geochimica et Cosmochimica Acta, 65(2), 311–321. https://doi.org/10.1016/s0016-7037(00)00528-7

Koch, M. C., Fujisawa, K., & Murakami, A. (2020). Adjoint Hamiltonian Monte Carlo algorithm for the estimation of elastic modulus through the inversion of elastic wave propagation data. International Journal for Numerical Methods in Engineering, 121(6), 1037–1067. https://doi.org/10.1002/nme.6256

Kohn, M. J., & Spear, F. (2000). Retrograde net transfer reaction insurance for pressure-temperature estimates. Geology, 28(12), 1127. https://doi.org/10.1130/0091-7613(2000)28%253C1127:rntrif%253E2.0.co;2

Lasaga, A. C. (1979). Multicomponent exchange and diffusion in silicates. Geochimica et Cosmochimica Acta, 43(4), 455–469. https://doi.org/10.1016/0016-7037(79)90158-3

Lasaga, A. C. (1983). Geospeedometry: An Extension of Geothermometry. In S. K. Saxena (Ed.), Kinetics and Equilibrium in Mineral Reactions (Vol. 3, pp. 81–114). Springer New York. https://doi.org/10.1007/978-1-4612-5587-1_3

Lasaga, A. C., Richardson, S. M., & Holland, H. D. (1977). The Mathematics of Cation Diffusion and Exchange Between Silicate Minerals During Retrograde Metamorphism. In S. K. Saxena, S. Bhattacharji, H. Annersten, & O. Stephansson (Eds.), Energetics of Geological Processes (pp. 353–388). Springer Berlin Heidelberg. https://doi.org/10.1007/978-3-642-86574-9_15

Liati, A., Gebauer, D., & Fanning, C. M. (2004). The age of ophiolitic rocks of the Hellenides (Vourinos, Pindos, Crete): First U–Pb ion microprobe (SHRIMP) zircon ages. Chemical Geology, 207(3–4), 171–188. https://doi.org/10.1016/j.chemgeo.2004.02.010

Mackay-Champion, T., & Cawood, I. P. (2025). An Inverse Method for Quantifying Petrological Parameters and Uncertainty in Phase Equilibrium Modelling. Journal of Metamorphic Geology, jmg.70016. https://doi.org/10.1111/jmg.70016

Medaris, L. G., Wang, H. F., Mísař, Z., & Jelínek, E. (1990). Thermobarometry, diffusion modelling and cooling rates of crustal garnet peridotites: Two examples from the Moldanubian zone of the Bohemian Massif. Lithos, 25(1–3), 189–202. https://doi.org/10.1016/0024-4937(90)90014-r

Mehlig, B., Heermann, D. W., & Forrest, B. M. (1992). Hybrid Monte Carlo method for condensed-matter systems. Physical Review B, 45(2), 679–685. https://doi.org/10.1103/physrevb.45.679

Metropolis, N., Rosenbluth, A. W., Rosenbluth, M. N., Teller, A. H., & Teller, E. (1953). Equation of State Calculations by Fast Computing Machines. The Journal of Chemical Physics, 21(6), 1087–1092. https://doi.org/10.1063/1.1699114

Mikkola, S., & Tanikawa, K. (1999). Explicit Symplectic Algorithms for time-transformed Hamiltonians. Celestial Mechanics and Dynamical Astronomy, 74, 287–295.

Moulas, E. (2023). GDIFF: A Finite Difference code for the calculation of multicomponent diffusion in garnet (Version v 1.2) [Computer software]. Zenodo. https://doi.org/10.5281/ZENODO.7805989

Moulas, E., & Brandon, M. T. (2022). KADMOS: A Finite Element code for the calculation of apparent K-Ar ages in minerals (Version 1) [Computer software]. Zenodo. https://doi.org/10.5281/ZENODO.7358138

Moulas, E., Podladchikov, Y. Y., Aranovich, L. Ya., & Kostopoulos, D. (2013). The problem of depth in geology: When pressure does not translate into depth. Petrology, 21(6), 527–538. https://doi.org/10.1134/S0869591113060052

Moutzouris, D., Moulas, E., Kostopoulos, D., Pomonis, P., Beranoaguirre, A., Chatzitheodoridis, E., & Gerdes, A. (2025). Emplacement of the Pindos ophiolite, NW Greece: P-T-t-kinematic constraints from the metamorphic sole. Lithos, 516–517(108285). https://doi.org/10.1016/j.lithos.2025.108285

Mulder, J. A., Berry, R. F., Meffre, S., & Halpin, J. A. (2016). The metamorphic sole of the western Tasmanian ophiolite: New insights into the Cambrian tectonic setting of the Gondwana Pacific margin. Gondwana Research, 38, 351–369. https://doi.org/10.1016/j.gr.2015.12.010

Müller, T., Dohmen, R., Becker, H. W., Ter Heege, J. H., & Chakraborty, S. (2013). Fe–Mg interdiffusion rates in clinopyroxene: Experimental data and implications for Fe–Mg exchange geothermometers. Contributions to Mineralogy and Petrology, 166(6), 1563–1576. https://doi.org/10.1007/s00410-013-0941-y

Neal, R. M. (1996). Bayesian Learning for Neural Networks. Springer New York. https://doi.org/10.1007/978-1-4612-0745-0

Neal, R. M. (2011). MCMC using Hamiltonian dynamics. https://doi.org/10.1201/b10905

Neidinger, R. D. (2010). Introduction to Automatic Differentiation and MATLAB Object-Oriented Programming. SIAM Review, 52(3), 545–563. https://doi.org/10.1137/080743627

Olker, B., Altherr, R., & Paquin, J. (2003). Fast exhumation of the ultrahigh-pressure Alpe Arami garnet peridotite (Central Alps, Switzerland): Constraints from

geospeedometry and thermal modelling. Journal of Metamorphic Geology, 21(4), 395–402. https://doi.org/10.1046/j.1525-1314.2003.00450.x

Reuber, G. S. (2021). Statistical and deterministic inverse methods in the geosciences: Introduction, review, and application to the nonlinear diffusion equation. GEM - International Journal on Geomathematics, 12(1). https://doi.org/10.1007/s13137-021-00186-y

Revels, J., Lubin, M., & Papamarkou, T. (2016). Forward-Mode Automatic Differentiation in Julia (No. arXiv:1607.07892). arXiv. https://doi.org/10.48550/arXiv.1607.07892

Schorn, S., Moulas, E., & Stüwe, K. (2024). Exothermic reactions and 39Ar–40Ar thermochronology: Hydration leads to younger apparent ages. Geology, 52(6), 458–462. https://doi.org/10.1130/G51776.1

Schwarzenbach, E. M., Vogel, M., Früh-Green, G. L., & Boschi, C. (2021). Serpentinization, Carbonation, and Metasomatism of Ultramafic Sequences in the Northern Apennine Ophiolite (NW Italy). Journal of Geophysical Research: Solid Earth, 126(5), e2020JB020619. https://doi.org/10.1029/2020JB020619

Searle, M., & Cox, J. (1999). Tectonic setting, origin, and obduction of the Oman ophiolite. Geological Society of America Bulletin, 111(1). https://doi.org/10.1130/0016-7606(1999)111%253C0104:TSOAOO%253E2.3.CO;2

Searle, M. P., Waters, D. J., Garber, J. M., Rioux, M., Cherry, A. G., & Ambrose, T. K. (2015). Structure and metamorphism beneath the obducting Oman ophiolite: Evidence from the Bani Hamid granulites, northern Oman mountains. Geosphere, 11(6), 1812–1836. https://doi.org/10.1130/GES01199.1

Sen, M. K., & Biswas, R. (2017). Transdimensional seismic inversion using the reversible jump Hamiltonian Monte Carlo algorithm. GEOPHYSICS, 82(3), R119–R134. https://doi.org/10.1190/geo2016-0010.1

Spear, F. S. (2004). Fast Cooling and Exhumation of the Valhalla Metamorphic Core Complex, Southeastern British Columbia. International Geology Review, 46(3), 193–209. https://doi.org/10.2747/0020-6814.46.3.193

Tagliaferri, A., Moulas, E., Schmalholz, S. M., & Schenker, F. L. (2025). Fast and Spatially Heterogeneous Cooling Rates at Amphibolite-Facies Conditions in the Lepontine Alps (Switzerland). Geochemistry, Geophysics, Geosystems, 26(11), e2025GC012410. https://doi.org/10.1029/2025GC012410

Turner, G., Miller, J. A., & Grasty, R. L. (1966). The thermal history of the Bruderheim meteorite. Earth and Planetary Science Letters, 1(4), 155–157. https://doi.org/10.1016/0012-821X(66)90061-6

Xu, K., Ge, H., Tebbutt, W., Tarek, M., Trapp, M., & Ghahramani, Z. (2020). AdvancedHMC.jl: A robust, modular and efficient implementation of advanced HMC algorithms. 2nd Symposium on Advances in Approximate Bayesian Inference, 118, 1–10.

Xu, Y., Chu, W., Huang, S., Guo, R., Lu, S., & Nan, F. (2025). Three-dimensional gravity inversion based on the Hamiltonian Monte Carlo method. Geophysical Prospecting, 73, 1301–1314. https://doi.org/10.1111/1365-2478.70016

Yoshida, H. (1990). Construction of higher order symplectic integrators. Physics Letters A, 150(5–7), 262–268. https://doi.org/10.1016/0375-9601(90)90092-3

Zhong, X., Moulas, E., & Tajčmanová, L. (2018). Tiny timekeepers witnessing high-rate exhumation processes. Scientific Reports, 8(1), 2234. https://doi.org/10.1038/s41598-018-20291-7

Zhong, X., Moulas, E., & Tajčmanová, L. (2020). Post-entrapment modification of residual inclusion pressure and its implications for Raman elastic thermobarometry. Solid Earth, 11(1), 223–240. https://doi.org/10.5194/se-11-223-2020

Zunino, A., Ghirotto, A., Armadillo, E., & Fichtner, A. (2022). Hamiltonian Monte Carlo Probabilistic Joint Inversion of 2D (2.75D) Gravity and Magnetic Data. Geophysical Research Letters, 49(20), e2022GL099789. https://doi.org/10.1029/2022GL099789

Zuza, A. V., Levy, D. A., & Mulligan, S. R. (2022). Geologic field evidence for non-lithostatic overpressure recorded in the North American Cordillera hinterland, northeast Nevada. Geoscience Frontiers, 13(2), 101099. https://doi.org/10.1016/j.gsf.2020.10.006

Chapter 4: Rapid cooling in metamorphic soles revealed from Quartz-in-Garnet viscoelastic modeling

Author contribution

The author of this dissertation prepared the original manuscript, developed the numerical model, implemented the primary codes for inversion and Hamiltonian Monte Carlo, designed the figures and performed the calculations, data analysis and interpretation of the results.

Abstract

Metamorphic soles are thin slivers of metamorphic rocks located at the base of ophiolitic sequences. They are characterized by a complex Pressure-Temperature-time (P-T-t) evolution that drives a series of chemical and mechanical transformations. With recent advances in numerical modeling, their mechanical behavior can be investigated to yield valuable insights into the processes governing their formation. In this chapter, we develop a viscoelastic thermomechanical numerical model and couple it with a Hamiltonian Monte Carlo inversion algorithm. This framework is used to constrain key parameters that shed light on the formation of the Pindos metamorphic sole. In particular, we estimate the initial temperature and pressure of equilibration, as well as the initial cooling and decompression rates required to reproduce the observed maximum residual pressure of quartz inclusions in garnet. Our results indicate that, to preserve a maximum residual pressure of 0.387 GPa in quartz, the metamorphic sole must have undergone rapid cooling with an initial cooling rate exceeding 100 °C/Myr. Such rapid cooling helps maintain the quartz-in-garnet system within the elastic deformational regime. Furthermore, the studied mica schist likely began its retrograde evolution at an initial temperature of approximately 630 °C and a pressure of 1.2 GPa. In contrast, the decompression rate appears to have a negligible influence on reproducing the observed data. These findings are consistent with the independent petrological analysis presented in Chapter 2 and the diffusion-based inversion results discussed in Chapter 3. Finally, the agreement of our results with previous numerical and petrological work serves as a strong indication that shear heating was the dominant factor controlling the formation and subsequent cooling of the Pindos metamorphic sole.

4.1 Introduction

Metamorphic soles are thin layers of metamorphic rocks that occur at the base of ophiolite sequences. Most of the volume of metamorphic soles is comprised of metapelites and metabasites that record conditions spanning from greenschist to granulite facies (e.g., Carosi et al., 1996). These rocks are widely used to study processes related to the obduction and emplacement of ophiolites onto continental crust. In particular, metamorphic soles preserve records of their complex Pressure-Temperature-time (P-T-t) evolution, making them valuable archives for reconstructing tectono-metamorphic histories. However, despite decades of research, the mechanisms governing their formation and subsequent exhumation remain debated (Agard et al., 2016; Ambrose et al., 2021; Duretz et al., 2016; Garber et al., 2025; Guilmette et al., 2023; Hacker, 1994; Ibragimov et al., 2024; Jamieson, 1980; M. Searle & Cox, 1999).

One key aspect of metamorphic soles is their high-grade metamorphic character compared to the surrounding rocks. This characteristic has been the focus of extensive petrological research for many decades (Dewey & Casey, 2013; Hacker, 1991; Jamieson, 1986; Rioux et al., 2023; M. P. Searle & Malpas, 1982). Recent findings have indicated that, it is not only the high-grade P-T conditions that need to be explained but also the short, temporal character of the obduction process (Garber et al., 2025; Ibragimov et al., 2024; Ibragimov & Moulas, 2024). Evidence for the short temporal character of such processes are, so far, explained best with the influence of dissipated heat during metamorphism, followed by a period of rapid quenching during the rapid heat conduction on the cold-footwall rocks (Ibragimov et al., 2024). Therefore, the investigation of metamorphic-sole rocks can offer insights into thermally-activated, fast-cooling processes. The mechanical deformation of minerals at high-grade conditions offers a unique opportunity in the investigation of thermally-activated processes. Chemical diffusion and rate-dependent plasticity, commonly known also as viscous creep, can be used to place constraints on the temporal character of mineral behavior (Zhong et al., 2018, 2020).

The development of stress in host-inclusion systems is known for many years (e.g., Rosenfeld & Chase, 1961). This approach is based on the fact that during the P-T evolution of a rock, differences in thermal expansivity and bulk modulus of the inclusion and the host generate pressure differences across the two minerals (e.g., Zhang, 1998 and references therein). The final/residual pressure of the inclusion can be directly measured at room conditions using analytical techniques such as Raman spectroscopy (Angel et al., 2019). In the case that the system behaved elastically during the P-T-t evolution and based on different

assumptions (see Moulas et al., 2020), the residual pressure of mineral inclusions measured at room conditions can be used to derive the conditions of entrapment (e.g., Angel et al., 2014; Van Der Molen & Van Roermund, 1986; Zhang, 1998). Under purely elastic behavior the inclusion-in-host systems are path-independent. However, when temperature effects are considered, the mechanical response of an inclusion-in-host system becomes more complex. More specifically, at elevated temperatures the host mineral may transition from an elastic to a viscous behavior which can result in partial or complete relaxation of inclusion pressure along the P-T-t evolution (Dabrowski et al., 2015; Pummell & Thomas, 2024; Zhong et al., 2020). In such cases, the system becomes path-dependent. This means that different P-T-t paths lead to different and unique inclusion pressure evolutions. Therefore, the residual pressure measured in mineral inclusions commonly reflects the combined effect of elastic and viscous deformation. In such complicated scenarios, numerical models are needed to simulate the visco-elastic behavior of the inclusion-in-host systems. Direct comparison of natural data (i.e., residual pressures of inclusions) with modeled outputs can yield valuable information on the P-T-t evolution of rocks. These models are also used to quantify parameters such as the cooling and decompression rate that are responsible for observing the residual pressure of inclusions and other measured data (Luisier et al., 2023; Zhong et al., 2018; Zhukov & Korsakov, 2015).

In the present study we present a mechanical model to simulate the deformational behavior of quartz inclusions hosted in garnet. This mechanical forward model is used to investigate the cooling and decompression history of a garnet-mica shist from the Pindos metamorphic sole in northwest Greece (Moutzouris et al., 2025). The forward model was coupled with a Hamiltonian Monte Carlo (HMC) algorithm to quantify the initial temperature, pressure, cooling rate and decompression rate responsible for the observed residual pressure in quartz (Figure 4.1). The inversion results indicate that the studied rocks must have cooled from conditions of about 630 ± 21.5 °C and 1.2 ± 0.03 GPa. These calculations are consistent in an independent manner with previous thermobarometric results (Moutzouris et al., 2025). The model further suggests rapid initial cooling (242.3 ± 70.9 °C/Myr) which prevented the pressure relaxation of quartz inclusions and has maintained the system in the elastic deformation regime. This finding independently agrees with cooling rate constraints derived from diffusion modeling (Moutzouris et al., 2026). Finally, we show that, for this case, the decompression rate has a negligible influence on the final residual pressure of quartz inclusions. A key finding of the present work is the strong agreement between diffusion and mechanical modeling in relation to natural data. The results highlight the importance of the

fast, transient character of the metamorphic sole formation in the preservation of the elastic character of mineral inclusions in garnet.

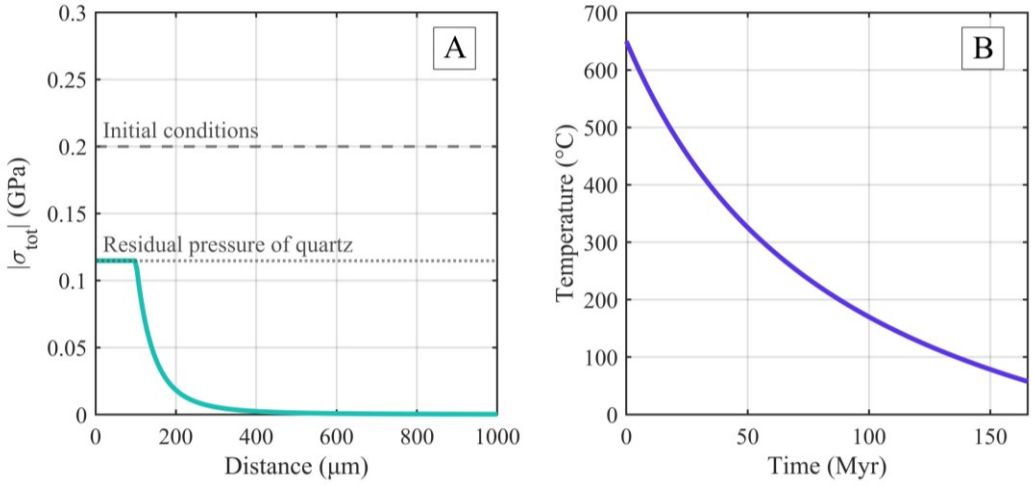

Figure 4.1: Conceptual model illustrating the goal of this study. (A) The total radial stress is shown in the domain of a quartz inclusion (radius: 100 μm) hosted within garnet. Initially, both minerals are in mechanical equilibrium at a stress value of 0.2 GPa. As the system cools along the path shown in (B), quartz and garnet respond differently leading to the development of a stress difference. By the time surface conditions are reached, the quartz inclusion retains a residual pressure as shown in (A). In this study, we aim to quantify the initial cooling rate, decompression rate, temperature and pressure that can explain the measured residual pressure in quartz from the Pindos metamorphic sole.

4.2 Methods

4.2.1 Governing Equations

The mechanical forward problem solves the conservation of momentum and mass in one dimension and in spherical coordinates. Due to the small scale of the model domain, and the large timescales considered, we do not need to solve for the temperature evolution in the host-inclusion system. It is thus assumed that the host-inclusion system is always at thermal equilibrium (homogenous temperature). In addition, for the conditions investigated here, we do not consider inertia and buoyancy terms. These assumptions closely follow the model formulation used in Zhong et al. (2018, 2020).

Momentum conservation (force balance) in the radial direction is written as:

$$\frac{\partial \tau_{rr}}{\partial r} - \frac{\partial P}{\partial r} + \frac{3\tau_{rr}}{r} = 0 \qquad (4.1)$$

where r is the radial coordinate (m), P is pressure (Pa) and τ_{rr} is the radial deviatoric stress (Pa). To close the system of equations two expressions are required for P and τ_{rr}. In this model we consider compressibility, therefore the density of minerals is allowed to change with time. For this reason, the evolution of P with time is derived from the combination of mass conservation and an Equation Of State (EOS; for details see Appendix A of Moulas et al., 2020):

$$\frac{dP}{dt} = -K\dot{\Theta} + \alpha K\frac{dT}{dt} \tag{4.2}$$

where K is the bulk modulus (in Pa), α is the thermal expansivity (in K^{-1}), and $\dot{\Theta}$ is the divergence of velocity (in s^{-1}) which, in the radial direction, is equal to:

$$\dot{\Theta} = \frac{1}{r^2}\frac{\partial}{\partial r}(r^2 v_r) = \frac{\partial v_r}{\partial r} + \frac{2v_r}{r} \tag{4.3}$$

where v_r is the velocity in the radial direction (in m/s). Substituting equation (4.3) into equation (4.2) we obtain an expression for pressure (defined as the negative mean stress):

$$\frac{dP}{dt} = -K\frac{1}{r^2}\frac{\partial}{\partial r}(r^2 v_r) + \alpha K\frac{dT}{dt} \tag{4.4}$$

To calculate the deviatoric radial stress (τ_{rr}) we use a Maxwell visco-elastic rheological model. By definition. the Maxwell model assumes that the total viscous stress is equal to the total elastic stress. In addition, the total deviatoric strain rate ($\dot{\varepsilon}_{rr}^{T}$), is the sum of the elastic deviatoric strain rate ($\dot{\varepsilon}_{rr}^{e}$), the viscous deviatoric strain rate ($\dot{\varepsilon}_{rr}^{v}$) and plastic deviatoric strain rate ($\dot{\varepsilon}_{rr}^{p}$):

$$\dot{\varepsilon}_{rr}^{T} = \dot{\varepsilon}_{rr}^{e} + \dot{\varepsilon}_{rr}^{v} + \dot{\varepsilon}_{rr}^{p} \tag{4.5}$$

It has been demonstrated that, due to their stiffness, host-inclusion mineral systems can be appropriately modelled using the small-strain approximation (Moulas et al. 2023). Thus, our use of strain rate tensor is equivalent to deformation rate tensor for viscous materials. The viscous deviatoric strain rate can be described with the following constitutive law:

$$\dot{\varepsilon}_{rr}^{v} = \frac{\tau_{rr}}{2\eta} \tag{4.6}$$

where η is the effective viscosity (in Pa·s). To calculate η we consider the non-Newtonian flow-law formulation as shown in Dabrowski et al. (2015). Therefore, η can be recasted as a function of τ_{rr} in the following manner:

$$\eta = W|\tau_{rr}|^{1-n} \tag{4.7}$$

where W is the experimentally-derived, pre-exponential factor of the flow law and n is the power-law exponent. Since we use the flow law of Wang & Ji (1999), W is given by:

$$W = \frac{G^n}{2B}\exp\left(g \cdot \frac{T_m}{T}\right) \tag{4.8}$$

where G is the shear modulus of the host mineral (Pa), g and B (s^{-1}) are experimentally determined parameters and T_m is the melting temperature (K) of the host.

To derive the constitutive law for the elastic deviatoric strain rate, we first express the elastic deviatoric strain (ε^e_{rr}) as:

$$\varepsilon^e_{rr} = \frac{\tau_{rr}}{2G} \tag{4.9}$$

Then, by differentiating equation (4.9) with respect to time and assuming that the shear modulus G is time-independent, we write:

$$\dot{\varepsilon}^e_{rr} = \frac{\dot{\tau}_{rr}}{2G} \tag{4.10}$$

where $\dot{\tau}_{rr}$ is the derivative of τ_{rr} with respect to time.

The total plastic strain rate tensor ($\dot{\varepsilon}^p_{ij}$) is expressed by the following relation:

$$\dot{\varepsilon}^p_{ij} = \lambda\frac{\partial Q}{\partial \sigma_{ij}} \tag{4.11}$$

where λ is the plastic multiplier, Q is the plastic flow potential (see for example Kaus, 2010 and references therein) and σ_{ij} is the stress tensor. In our one-dimensional case, the deviatoric plastic strain rate in the radial direction ($\dot{\varepsilon}^p_{rr}$) is therefore expressed as:

$$\dot{\varepsilon}^p_{rr} = \lambda'\frac{\partial Q}{\partial \tau_{rr}} \tag{4.12}$$

where λ' is the plastic multiplier corresponding for this strain rate component.

To account for conditions of high deviatoric stresses where the host may behave in a plastic manner, a Tresca criterion is applied. By plastic, we mean the rate-independent plasticity that depends only on the value of a yield stress (e.g., Hill, 1950; Moulas et al., 2023). The Tresca criterion states that time-independent plastic deformation occurs when:

$$|\sigma_{rr} - \sigma_{\theta\theta}| \geq Y \tag{4.13}$$

where σ_{rr} is the total radial stress (Pa), $\sigma_{\theta\theta}$ is the total tangential stress (Pa) and Y is the yield strength of the host (Pa). Using the total stress decomposition in which $\sigma_{rr} = \tau_{rr} - P$ and $\sigma_{\theta\theta} = \tau_{\theta\theta} - P$, it can be shown that equation (4.13) can be expressed as:

$$|\tau_{rr} - \tau_{\theta\theta}| \geq Y \tag{4.14}$$

However, due to spherical symmetry, $\tau_{\theta\theta} = -1/2\tau_{rr}$. Therefore, equation (4.14) becomes:

$$\left|\frac{3}{2}\tau_{rr}\right| \geq Y \tag{4.15}$$

Combining the Tresca criterion of equation (4.15) with equation (4.12), plasticity is considered in the following manner:

$$if\ \left|\frac{3}{2}\tau_{rr}\right| < Y, then\ \lambda' = 0 \tag{4.16}$$

$$if\ \left|\frac{3}{2}\tau_{rr}\right| \geq Y, then\ \lambda' > 0\ and\ \tau_{rr} = \frac{2}{3}Y \cdot sign(\dot{\varepsilon}_{rr}^{T}) \tag{4.17}$$

Therefore, equations (4.16) and (4.17) indicate that time-independent plastic deformation occurs only when the radial deviatoric stress exceed the Tresca yield stress. In all other cases, the plastic deviatoric strain rate is zero and the material exhibits purely viscoelastic behavior.

In the viscoelastic case, λ' is equal to zero and equations (4.6) and (4.10) are substituted to yield:

$$\dot{\varepsilon}_{rr}^{T} = \frac{\dot{\tau}_{rr}}{2G} + \frac{\tau_{rr}}{2\eta} \tag{4.18}$$

The system of equations is closed by expressing $\dot{\varepsilon}_{rr}^{T}$ based on kinematic relations:

$$\dot{\varepsilon}_{rr}^{T} = \frac{\partial v_r}{\partial r} - \frac{1}{3}\dot{\Theta} \tag{4.19}$$

The divergence of velocity $\dot{\Theta}$ can be substituted in equation (4.19) to yield:

$$\dot{\varepsilon}_{rr}^{T} = \frac{2}{3}\left(\frac{\partial v_r}{\partial r} - \frac{v_r}{r}\right) \tag{4.20}$$

4.2.2 Discretization

To proceed with the solution of the mechanical problem we discretize the equations using the finite difference method with implicit time (backward Euler) integration. Our approach follows the velocity-pressure formulation. The non-Newtonian flow law and the time-independent plasticity impose a non-linear behavior in the model. For this reason, we apply non-linear direct iterations (Picard) for each physical timestep until the solutions converge below a numerical tolerance of 10^{-10}. A numerical resolution of 100 grid points was chosen along with a physical timestep of 20,000 years. More details on the discretization procedure follow below.

The momentum conservation equation (4.1) requires an expression for the deviatoric stress. We begin by discretizing equation (4.18) as follows:

$$\dot{\varepsilon}_{rr}^{T} = \frac{(\tau_{rr}^{new} - \tau_{rr}^{old})}{2G \cdot dt} + \frac{\tau_{rr}^{new}}{2\eta} \tag{4.21}$$

where τ_{rr}^{new} is the unknown deviatoric stress in the new physical timestep and τ_{rr}^{old} is deviatoric stress calculated in the previous/old timestep. The previous equation assumes a purely viscoelastic behavior. By rearranging equation (4.21) we can show that:

$$\tau_{rr}^{new} = \frac{\xi}{1+\xi}\tau_{rr}^{old} + \frac{2\eta\dot{\varepsilon}_{rr}^{T}}{1+\xi} \tag{4.22}$$

where ξ is the Maxwell viscoelastic timescale and is equal to $\frac{\eta}{G \cdot dt}$. Equation (4.22) can be further simplified by grouping terms in the following manner:

$$\tau_{rr}^{new} = C\tau_{rr}^{old} + D\dot{\varepsilon}_{rr}^{T} \tag{4.23}$$

where $C = \frac{\xi}{1+\xi}$ and $D = \frac{2\eta}{1+\xi}$. The deviatoric strain rate from equation (4.20) is then substituted in equation (4.23). The result is:

$$\tau_{rr}^{new} = C\tau_{rr}^{old} + \frac{2D}{3}\frac{\partial v_r}{\partial r} - \frac{2D}{3}\frac{v_r}{r} \tag{4.24}$$

The system of equations is solved on a staggered grid as the one shown in Figure 4.2. However, if plastic deformation occurs, the radial stress component τ_{rr}^{new} is calculated via (4.17). In Figure 4.2, the green dashes correspond to the velocity (v_r) nodes whereas the filled, purple circles correspond to the pressure nodes where P and the material properties (G, K, η, α) exist. An additional ghost node is required to apply an external pressure boundary

condition. The pressure boundary condition is applied together with a zero deviatoric radial stress at the boundary. This choice of boundary condition implies that the host-inclusion system is immersed in a hydrostatic medium of negligible differential stress. In the following sections we will omit the subscripts "rr" for readability. If we assume that i corresponds to the index of the velocity nodes (Figure 4.2) then the different terms of the momentum conservation equation can be discretized as follows:

$$\frac{\partial \tau}{\partial r} = \frac{\tau_{i+1}^{new} - \tau_{i-1}^{new}}{\Delta r}$$

$$-\frac{\partial P}{\partial r} = -\frac{P_{i+1}^{new} - P_{i-1}^{new}}{\Delta r}$$

$$\frac{3\tau}{r} = \frac{3}{2r_i}(\tau_{i+1}^{new} + \tau_{i-1}^{new}) \tag{4.25}$$

in which, the deviatoric stresses are discretized based on equation (4.24):

$$\tau_{i+1}^{new} = C_{i+1}\tau_{i+1}^{old} + \frac{2}{3}D_{i+1}\frac{v_{i+1} - v_i}{\Delta r} - \frac{D_{i+1}}{3r_{i+1}}(v_{i+1} + v_i)$$

$$\tau_{i-1}^{new} = C_{i-1}\tau_{i-1}^{old} + \frac{2}{3}D_{i-1}\frac{v_i - v_{i-1}}{\Delta r} - \frac{D_{i-1}}{3r_{i-1}}(v_i + v_{i-1}) \tag{4.26}$$

The pressure equation (4.4) is discretized in a similar manner for all pressure unknowns with index j on the grid:

$$P_j^{new} + \Delta t K_j \frac{v_{j+1} - v_{j-1}}{\Delta r} + \frac{\Delta t K_j}{r_j}\left(v_{j+1} + v_{j-1}\right) = P_j^{old} + \alpha_j K_j (T^{new} - T^{old}) \tag{4.27}$$

Equations (4.25), (4.26) and (4.27) can be rearranged to derive the coefficients of the unknown velocities and pressures but also the known right-hand side values. All of the coefficients are given in Tables 4.1 and 4.2.

Table 4.1: Coefficients of velocities, pressures and right-hand side vector for the discretization of the momentum conservation equation. Variable i corresponds to the indices of velocity unknowns.

v_i	$-\frac{D_{i+1}}{2r_i r_{i+1}} - \frac{D_{i+1}}{3\Delta r \cdot r_{i+1}} - \frac{D_{i-1}}{2r_i r_{i-1}} - \frac{D_{i+1}}{\Delta r \cdot r_i} + \frac{D_{i-1}}{\Delta r \cdot r_i} + \frac{D_{i-1}}{3\Delta r \cdot r_{i-1}} - \frac{2D_{i+1}}{3\Delta r^2} - \frac{2D_{i-1}}{3\Delta r^2}$
v_{i+1}	$-\frac{D_{i+1}}{2r_i r_{i+1}} - \frac{D_{i+1}}{3\Delta r \cdot r_{i+1}} + \frac{D_{i+1}}{\Delta r \cdot r_i} + \frac{2D_{i+1}}{3\Delta r^2}$
v_{i-1}	$-\frac{D_{i-1}}{2r_i r_{i-1}} - \frac{D_{i-1}}{\Delta r \cdot r_i} + \frac{D_{i-1}}{3\Delta r \cdot r_{i-1}} + \frac{2D_{i-1}}{3\Delta r^2}$
P_{i+1}^{new}	$-\frac{1}{\Delta r}$
P_{i-1}^{new}	$\frac{1}{\Delta r}$
Right-hand side	$-\frac{3C_{i+1}\tau_{i+1}^{old}}{2r_i} - \frac{3C_{i-1}\tau_{i-1}^{old}}{2r_i} - \frac{C_{i+1}\tau_{i+1}^{old}}{\Delta r} + \frac{C_{i-1}\tau_{i-1}^{old}}{\Delta r}$

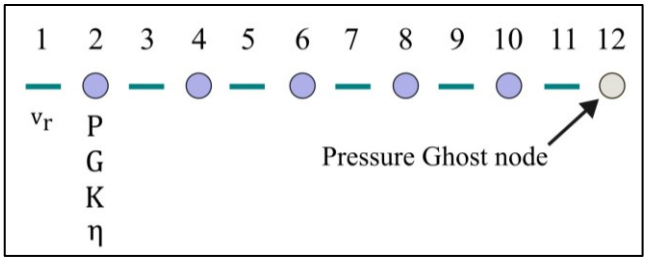

Figure 4.2: The staggered grid that is used to discretize and solve the system of equations. Green lines correspond to the grid points of velocity. Purple circles correspond to the grid points of pressure but also material properties. An additional node (grid point 12) is added for the pressure boundary condition.

Table 4.2: Coefficients of velocities, pressure and right-hand side vector for the discretization of the compressibility equation. Variable j corresponds to the indices of pressure unknowns.

v_{j+1}	$\frac{\Delta t K_j}{\Delta r} + \frac{\Delta t K_j}{r_j}$
v_{j-1}	$-\frac{\Delta t K_j}{\Delta r} + \frac{\Delta t K_j}{r_j}$
P_j^{new}	1
Right-hand side	$P_j^{old} + \alpha_j K_j (T^{new} - T^{old})$

4.2.3 Inversion algorithm and P-T-t paths

In this work, we combine a one-dimensional (1D) forward thermo-mechanical model with an HMC approach (see chapter 3 for details) to constrain the pressure-temperature-time (P-T-t) evolution of the Pindos metamorphic-sole metapelites (Moutzouris et al., 2025; chapter 2). We focus on the preservation of residual pressure values of quartz inclusions in garnet from metapelites (see chapter 2). Our inversion aims to quantify the P-T history ($P(t)$ and $T(t)$) required to reproduce the observed maximum residual pressure of quartz inclusions in the samples (0.387 GPa; chapter 2).

The inversion procedure is composed of two parts, the forward problem that is needed to solve the stress evolution of a quartz inclusion, and the HMC procedure is used to assess the parameters needed to describe the P-T history. The forward model is a one-dimensional, visco-elasto-plastic mechanical model that assumes spherical symmetry. The physical properties and the numerical parameters used are reported in the Supplementary Material.

For the inversion of the pressure and temperature history we regularize the inverse problem by assuming monotonic (in time) P-T histories. Thus, the temperature and pressure evolution of the rock is given by the following functions:

$$T(t) = \frac{T_0}{1 + a \cdot \frac{t}{T_0}} \quad \text{and} \quad P(t) = \frac{P_0}{1 + b \cdot \frac{t}{P_0}}$$

where T_0 is the initial equilibration temperature (°C), a is the initial cooling rate (°C /Myr), t is time (Myr), P_0 is the initial equilibration pressure (GPa) and b is the initial decompression rate (GPa/Myr). The choice of the asymptotic path for temperature is justified based on arguments presented in chapter 2. The asymptotic path for pressure is assumed to evolve similarly to temperature, preventing unrealistically high pressures at low temperatures. The models are run for a total duration of 165.5 Myr, following the dating results presented in chapter 2.

The mechanical forward model is applied in combination with HMC inverse method. HMC is a gradient-based sampling technique that is used to explore high-dimensional parameter spaces and quantify the uncertainty of model parameters (Betancourt, 2018; Neal, 1996, 2011). This technique is based on physical concepts from Hamiltonian dynamics and proposes large jumps in the parameter space which make the exploration of this parameter space efficient (Betancourt, 2018). In this study, we have used the *AdvancedHMC.jl* package of Xu et al.

(2020) which is incorporated in the *Turing.jl* probabilistic library (Fjelde et al., 2025). An application of HMC in a petrological framework and additional details on the method can be found in chapter 3.

Our algorithm proceeds through the following steps: (a) Initial values for T_0, P_0, a and b are selected based on their prior probability distributions. (b) Hamiltonian dynamics are then simulated by repeatedly solving the forward model to generate large jumps in the four-dimensional (T_0, P_0, a and b) parameter space using gradient information (Betancourt, 2018; Neal, 2011; and chapter 3 of this work). (c) The newly proposed accepted samples of T_0, P_0, a and b are evaluated according to their likelihood of reproducing the observed residual pressure of quartz inclusions. (d) Steps (a)-(c) are repeated until a sufficient number of samples has been obtained. For more details the reader is referred to chapter 3.

4.3 Results

Inversion based on HMC requires prior probability distributions as inputs for the investigated parameters (see chapter 3). The output of the inversion is represented by posterior probability distributions which show what parameter values are more likely to reproduce the observed data (e.g., residual pressure of quartz). These posterior probability distributions depend on priors. In general, parameters that are poorly constrained or unknown are represented by uniform prior distributions. Parameters that are better constrained are described by Gaussian probability distributions. Based on the inversion results of Moutzouris et al. (2026; see also chapter 3) we have assumed a $\mathcal{N}(241.3, 76.5)$ prior distribution for the initial cooling rate (a). That corresponds to a Gaussian distribution with a mean of 241.3 °C/Myr and a standard deviation of 76.5 °C/Myr. Based on the results of Moutzouris et al. (2025; see also chapter 2), we used a $\mathcal{N}(630.0, 20.0)$ for initial equilibration temperature (°C) and a $\mathcal{N}(1.1, 0.2)$ for initial pressure (GPa). The initial decompression rate (b) has not been previously constrained. Therefore, we considered a uniform prior distribution ranging from 0.01 to 1.0 GPa/Myr.

We used a total of 600 HMC samples and a random seed value of 42 to ensure reproducibility. The resulting computation time of our inversion was 14.0 hours requiring a total of 10,083 forward model evaluations. The results of the exploration of the four-dimensional parameter space are presented in Figure 4.3 and Figure 4.4. Figure 4.3A and 4.3B represent trace plots showing the progressively accepted parameter values for the initial cooling rate and the initial temperature. There is no visible large-scale trend which is an indication that

the algorithm has converged (see chapter 3). The initial cooling rate (Figure 4.3C) is described by a Gaussian posterior distribution with a mean of 242.2 °C/Myr and a standard deviation of 72.7 °C/Myr. There is a 68 % probability to reproduce the observed maximum residual pressure of quartz with initial cooling rates ranging from 165.2 to 318.2 °C/Myr. The mode (highest probability value) is at 255.1 °C/Myr. This shows that the posterior probability of initial cooling rate has changed negligibly compared to the assumed prior distribution. The same holds true for the initial equilibration temperature which shows a Gaussian posterior distribution with a mean of 627.3 °C and a standard deviation of 20.0 °C (Figure 4.3D).

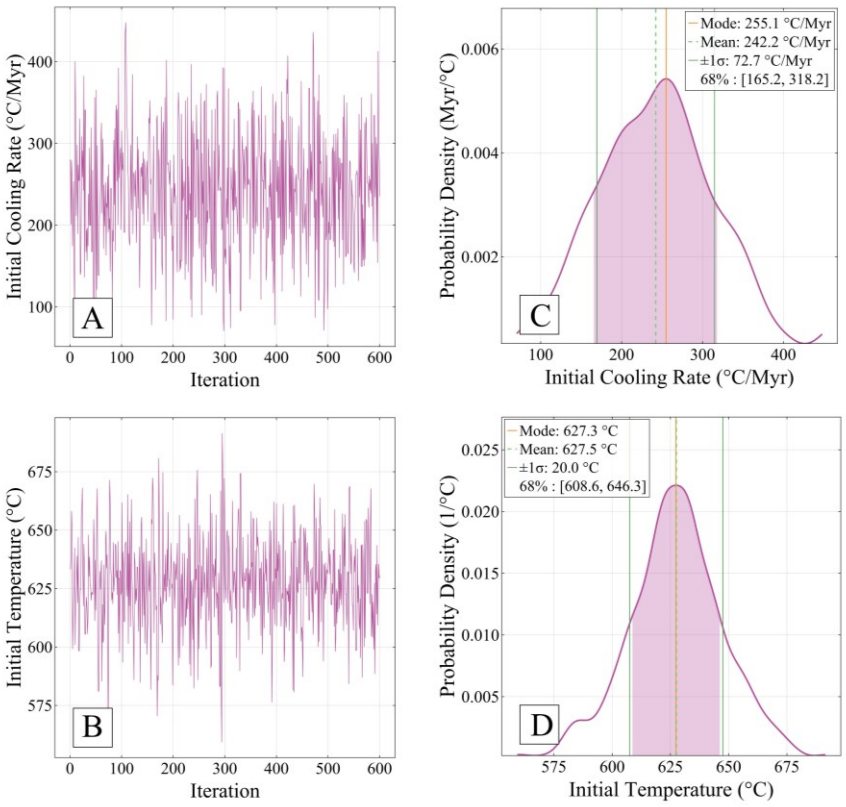

Figure 4.3: HMC results for initial cooling rate and initial temperature. (A) and (B) show the produced trace plots. The lack of a visible trend is an indication of convergence. (C) and (D) show the posterior distributions for the two parameters. Both parameters are described by well-defined Gaussian distributions.

The trace plots of initial pressure and initial decompression rate also show convergence (Figure 4.4A and 4.4B). The initial pressure is described by a well-defined Gaussian probability distribution with a mean of 1.226 GPa and a standard deviation of 0.026 GPa (Figure 4.4C). The mode of initial pressure coincides with the mean. The 68 % probability region lies between 1.203 and 1.252 GPa. The initial decompression rate shows a uniform posterior probability

distribution (Figure 4.4D). The 68 % probability region is found between a value of 0.197 and 0.834 GPa/Myr. However, lower and values than 0.197 GPa/Myr are also possible (Figure 4.4D).

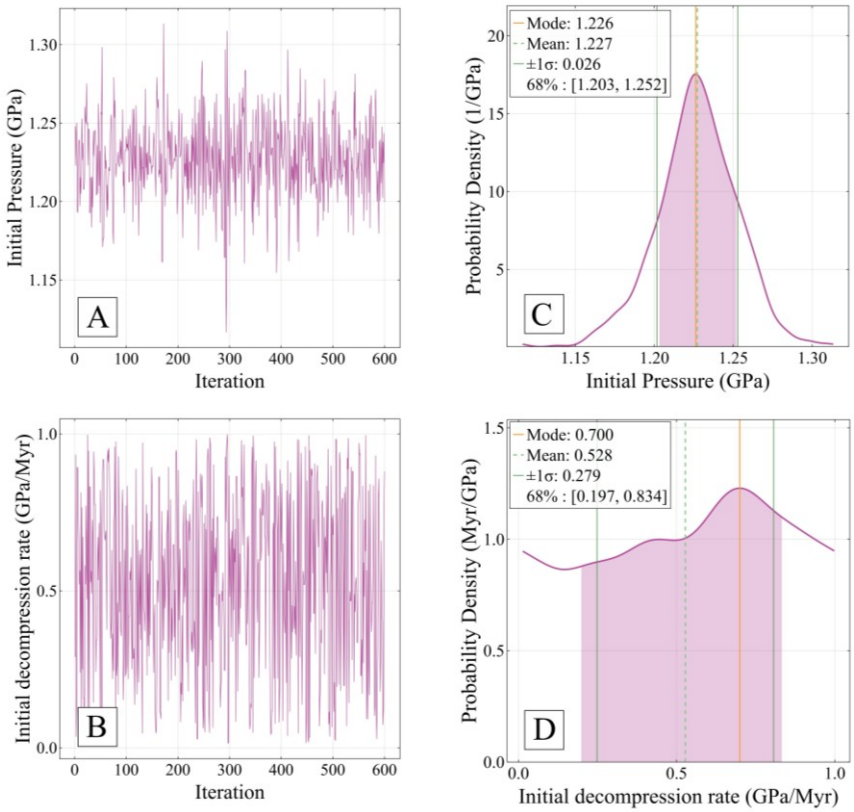

Figure 4.4: HMC results for initial pressure and initial decompression rate. (A) and (B) show the produced trace plots. The lack of a visible trend is an indication of convergence. (C) and (D) show the posterior distributions for the two parameters. The initial pressure shows a well-defined Gaussian posterior distribution while the decompression rate shows uniform characteristics indicating that it does not play a significant role in fitting the observed residual pressure of quartz.

To confirm the results obtained from the HMC inversion, we additionally generated misfit maps using a grid search approach. Misfit quantifies the squared difference between the observed residual pressure in quartz and the modeled one. We constructed two misfit maps: one exploring the parameter space defined by initial temperature and initial cooling rate (for a fixed initial pressure of 1.2 GPa and decompression rate of 0.9 GPa/Myr), and another exploring initial pressure and initial decompression rate (for a fixed initial temperature of 630 °C and cooling rate of 100 °C/Myr). The grid search systematically evaluates all remaining parameter combinations within these two separate spaces and calculates the corresponding

misfit surface (shown as a colourmap in the parameter space). This allows us to identify regions of the parameter space that provide the best fit between the model and the observations. In addition, in cases of few unknown parameters as in this case, the visual inspection of the misfit surface allows the identification of local minima and parameter tradeoffs. It is important to note that, with the grid search approach, each misfit map is computed over two parameters at a time. This is used only as a visual aid and contrasts with the HMC inversion, which explores all four parameters simultaneously in a single four-dimensional parameter space.

The results of the grid search are presented in Figure 4.5. Figure 4.5A shows a well-defined region, in the parameter space of initial temperature and initial cooling rate, where the misfit is low. This region indicates that if the initial temperature was at ~550 °C, low cooling rates would be sufficient to recover the observed residual pressure of quartz in garnet. For temperatures in the order of 630 °C as in our case, cooling rates of over 100 °C/Myr are required. In the parameter space defined by the initial pressure and initial decompression rate (Figure 4.5B) it is shown that the decompression rate does not affect the fit of the residual pressure of quartz and that the system must have started from an initial pressure of ~1.2 GPa.

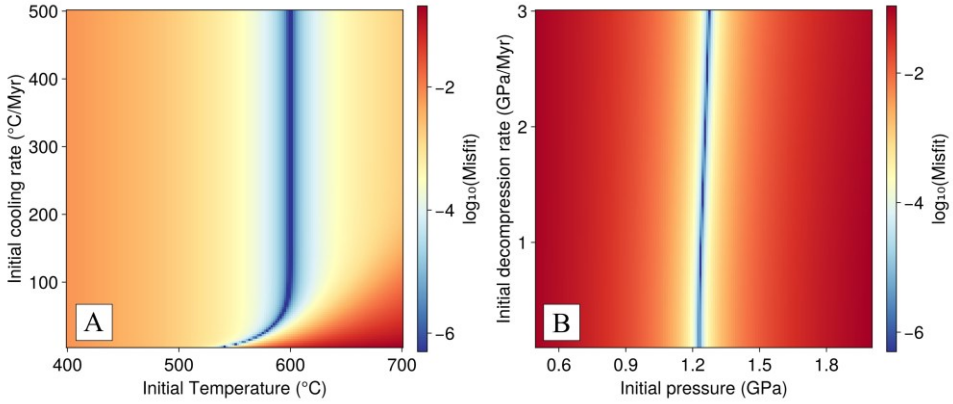

Figure 4.5: Grid search results. (A) Misfit map in the initial temperature and initial cooling rate parameter space (initial pressure and initial decompression rate are taken as constant). A well-defined, low-misfit region is identified that points to high cooling rates at temperatures of ~630 °C. (B) Misfit map in the initial pressure and initial decompression rate parameter space (initial temperature and initial cooling rate are taken as constant). A low-misfit region is identified showing that the rocks must have started decompressing from a pressure of ~1.2 GPa.

4.4 Discussion

The results presented in this chapter show a profound agreement with the results of Chapter 3 (Moutzouris et al., 2025) and Chapter 4 (Moutzouris et al., 2026). Evidently, in order to

observe the currently measured residual pressure of quartz in garnet (0.387 GPa; Moutzouris et al., 2025), the investigated rocks from the Pindos metamorphic sole must have started their retrograde path from 1.2 GPa and 630 °C. These results are consistent across all methodologies that have been used, from phase-equilibria modeling (Figure 2.9), to inverse diffusion modelling (Figure 3.4 to Figure 3.10), and finally, to inverse mechanical modelling of host-inclusion systems (Figure 4.3 and Figure 4.5).

Another significant finding is the close agreement between cooling rates estimated from mechanical modeling and those inferred from diffusion approaches. These methods indicate high cooling rates (>100 °C/Myr). These rapid cooling rates strongly suggest that the quartz-in-garnet system remained largely within the elastic regime. This is because slower cooling would prolong high-temperature conditions, allowing viscous relaxation to dominate (Dabrowski et al., 2015; Zhong et al., 2020). Therefore, the high cooling rates reflect the elastic limit, ensuring that inclusions retain the entrapment conditions that can be reliably determined using an elastic analytical solution (e.g., Moutzouris et al., 2025). In contrast, decompression rates appear to have minimal impact on the results. This is because the deformation around the quartz inclusions is limited, due to their spherical shapes and relatively small size, and this makes them suitable for elastic barometry. If the inclusions were larger and of arbitrary shape, the resulting stress concentration in the mineral host would enable rate-independent plastic deformation. In such cases, the degree of plastic deformation around inclusions can be sensitive to decompression rates (e.g., Luisier et al., 2023). However, the inclusions that were chosen in this study were such that the deformation in the surrounding garnet host was mostly viscoelastic, and thus strongly temperature dependent.

Mechanical inversion allows us to constrain the full retrograde P-T-t paths that the rocks must have followed to attain the currently measured residual pressure of quartz. The quantified paths, based on the accepted HMC samples, are plotted in Figure 4. Figure 4A shows the P-T-t trajectories overlaid on the phase-diagram section presented in Chapter 2 (Figure 2.9A). In Figure 4A, the deep green region highlights areas where the P-T-t paths are highly concentrated, while the light green area represents the full range of accepted paths. From Figure 4A it is evident that the investigated mica schist evolved rapidly from the peak biotite-garnet-muscovite-paragonite-quartz-melt assemblage to conditions where chlorite became stable. According to the calculated P-T-t paths, the rock crossed the solidus within an average of 0.2 Myr and reached 500 °C in approximately 1.1 Myr. The closing temperature for major element diffusion in garnet (~300 °C) was reached after an estimated 3.6 Myr. Figure 4B shows the full

accepted P-T-t paths. Some of the accepted P-T-t paths reach very high pressures relatively to their low temperatures (e.g., 300 °C at 1.2 GPa). This behavior could be explained from a combination of rapid cooling and very slow decompression at the subduction fault zone. Although such paths satisfy the data, our results show that the decompression rate has a negligible influence on the final outcome, and therefore, these datapoints cannot be used to infer the actual decompression path.

Our results carry significant implications about the cooling histories of ophiolitic soles. Cooling from ~630 °C to 500 °C within 1.1 Myr may, at a first glance, appear excessive, but such results are consistent with previous studies of the Oman metamorphic sole, where cooling to ~550 °C has been estimated to occur within 1-2 Myr (Hacker et al., 1996). Such results align well with other thermomechanical investigations of the Oman ophiolite (Ibragimov et al., 2024; their Figure 6b). The high cooling rates, determined in this work, provide valuable natural constraints on the processes driving metamorphic sole formation. Importantly, our results support the requirement of a transient process to explain the rapid thermal evolution of the metamorphic sole. In the case of the Pindos metamorphic sole, the important agreement between cooling rates derived from the comparison of numerical models with natural data (Chapter 2, 3 and 4) and the results of purely numerical studies (Duretz et al., 2016; Ibragimov et al., 2024) indicates that shear heating was the dominant mechanism responsible for its generation.

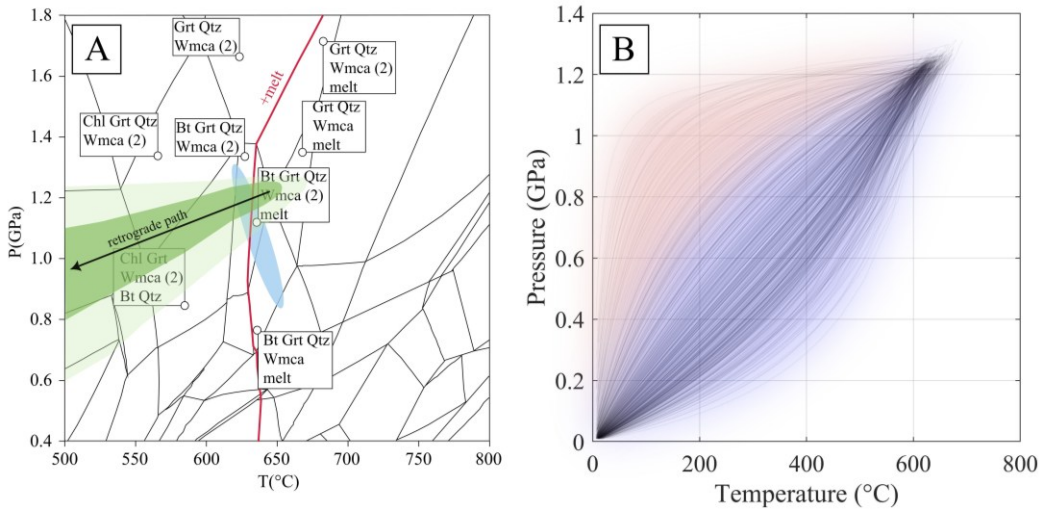

Figure 4.6: (A) The calculated evolution of the mica-schist from the Pindos metamorphic sole based on the accepted HMC samples of the mechanical inversion plotted on top of the phase diagram presented in Chapter 3 (Moutzouris et al., 2025). The dark green area indicates high density of P-T-t paths while light green indicates the entire area occupied by the accepted P-T-

t paths. (B) The full quantified P-T-t trajectories from initial to surface conditions based on our mechanical inversion. The paths shown within the red-shaded region indicate relatively high cooling rates coupled with low decompression rates. This pattern reflects limitations as the available data are not sufficient to constrain decompression rates accurately.

4.5 Conclusions

Mechanical inversion based on host-inclusion viscoelastic systems was used in this work to invert for the cooling rates of metamorphic-sole rocks. This approach is based on easy-to-obtain data since it only requires simple spectroscopic analyses of mineral inclusions. When these data are combined with a mechanical forward model, this method can provide robust constraints on metamorphic histories. In the case of the Pindos ophiolite, our mechanical inversion results indicate high cooling rates which exceed a value of 100 °C/Myr. Such high cooling rates are necessary to reproduce the observed residual pressure of quartz (0.387 GPa; Moutzouris et al., 2025). The implication of such cooling rates is that the quartz-in-garnet system has remained in the elastic deformational regime with negligible influence of viscous relaxation at high temperatures. Furthermore, our inversion suggests that the studied mica schist started its retrograde path from an initial temperature of 627.3 ± 20.0 °C and an initial pressure of 1.2 ± 0.03 GPa. Regarding the decompression rate, our inversion approach showed that it does not play a significant role in reproducing the observed residual pressure of quartz. Our results show a significant agreement with previous petrological work (Moutzouris et al., 2025; Chapter 2), inverse diffusion modeling (Moutzouris et al., 2026; Chapter 3) and purely numerical studies of metamorphic soles (Duretz et al., 2016; Ibragimov et al., 2024) suggesting that shear heating was the dominant mechanism for metamorphic sole formation.

4.6 Supplementary Material

4.6.1 Model parameters

The exact model parameters used for this study are displayed in Table S. 4.1. The viscosity (rate-dependent plasticity) of the host is expressed with the non-Newtonian flow law of Wang & Ji (1999). The melting temperature of almandine-rich garnet is taken from Karato et al. (1995). The thermoelastic properties for quartz have been obtained from Angel et al. (2015). The thermoelastic properties for almandine are taken from Enami et al. (2007) and references therein. Rate-independent plasticity is activated if differential stresses exceed the 5.0 GPa yield strength of almandine-pyrope garnet (Whitney et al., 2007). We considered a garnet with a radius of 300 μm and a quartz inclusion radius of 10 μm.

Table S. 4.1: Parameter values used for the mechanical forward model. K: Bulk modulus, G: Shear modulus, α: thermal expansivity, Y: yield strength of garnet, n: power-law exponent of garnet, T_m: melting temperature of garnet, B and g flow-law parameters. L: Radius of crystal.

	K (GPa)	G (GPa)	α (1/K)	Y (GPa)	T_m (K)	B (s^{-1})	g	n	L (µm)
Quartz	37.12	44.3	$3.64 \cdot 10^{-5}$	-	-	-	-	-	10
Garnet	175.1	92.1	$1.57 \cdot 10^{-5}$	5.0	1570	exp(40.1)	32	3	300

4.6.2 Benchmarks

Our thermo-mechanical code has been tested and benchmarked with a variety of published analytical solutions that consider different assumptions and rheological behaviors. Firstly, we tested a purely elastic case that assumes a pressurized hollow sphere surrounded by an elastic shell (p. 197; Bower, 2010). This analytical solution assumes the absence of body forces while the outer and inner surfaces of the system are subjected to a pressure. The numerical and analytical solutions of differential stress are presented in Figure S. 4.1.

We subsequently tested an elasto-plastic case against the benchmark of Bower (p. 215; 2010). This benchmark considers two domains: one domain affected by rate-independent plasticity and a purely elastic domain (see Moulas et al., 2023; their Fig. 7 for details). We have used a constant pressure for the inclusion domain and a stress-free/zero-velocity boundary for the outer surface of the model. The inclusion radius was set to be 10 times smaller than the radius of the host. A numerical resolution of 2000 grid points was used. Figure S. 4.2 shows the comparison of the normalized total stress over the yield strength between numerical and analytical solution.

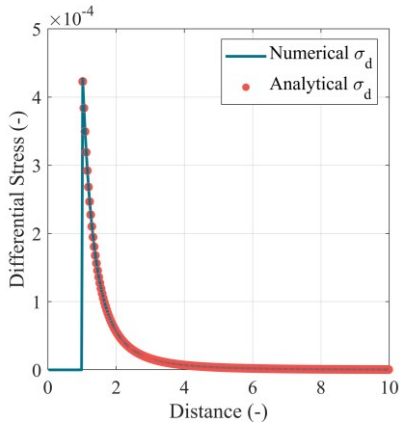

Figure S. 4.1: Comparison of differential stress for the host mineral between our purely elastic numerical code and the analytical benchmark of Bower (2010). The region of the inclusion can

be identified by the constant differential stress. The solutions are expressed in nondimensional (normalized) units.

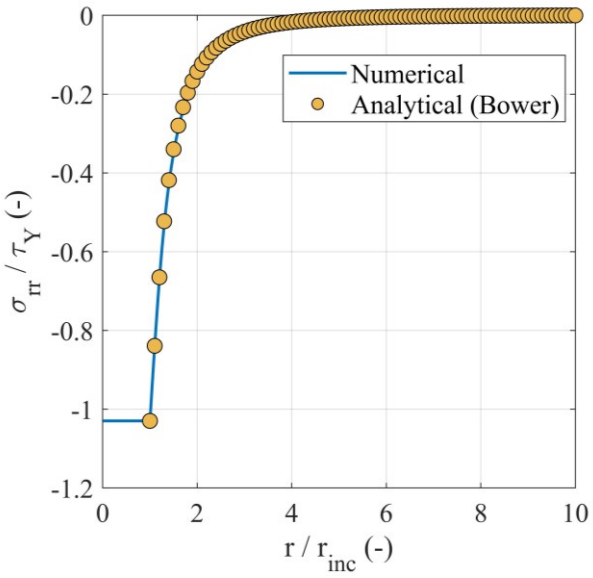

Figure S. 4.2: Comparison of total stress in the radial direction normalized by the yield strength of the host between our elastoplastic numerical model and the analytical plasticity benchmark (Bower, 2010, p. 215). The x axis represents distance normalized by the radius of the inclusion. The solutions are expressed in nondimensional units.

As a following benchmark, we tested the visco-elastic behavior of our code against the analytical solution of Dabrowski et al. (2015). We first benchmarked the linear case in which the power law exponent is equal to unity ($n = 1$). To perform this benchmark, we initialized the model with a mechanically equilibrated elastic solution in which a pressure difference between the inclusion and the host is developed. Starting from this configuration, we then simulated the subsequent pressure relaxation using our viscoelastic scheme. We assumed that the inclusion has a radius 200 times smaller than that of the host. Since the solution of Dabrowski et al. (2015) assumes that the host behaves as an incompressible viscous solid, incompressibility in our model was approximated by assigning bulk and shear moduli to the host that are 6 orders of magnitude larger than those of the inclusion. A zero-velocity boundary condition was forced at both sides of the model domain after the initial elastic configuration. The comparison of the pressure drop in the inclusion between our numerical model and the analytical solution is presented in Figure S. 4.3.

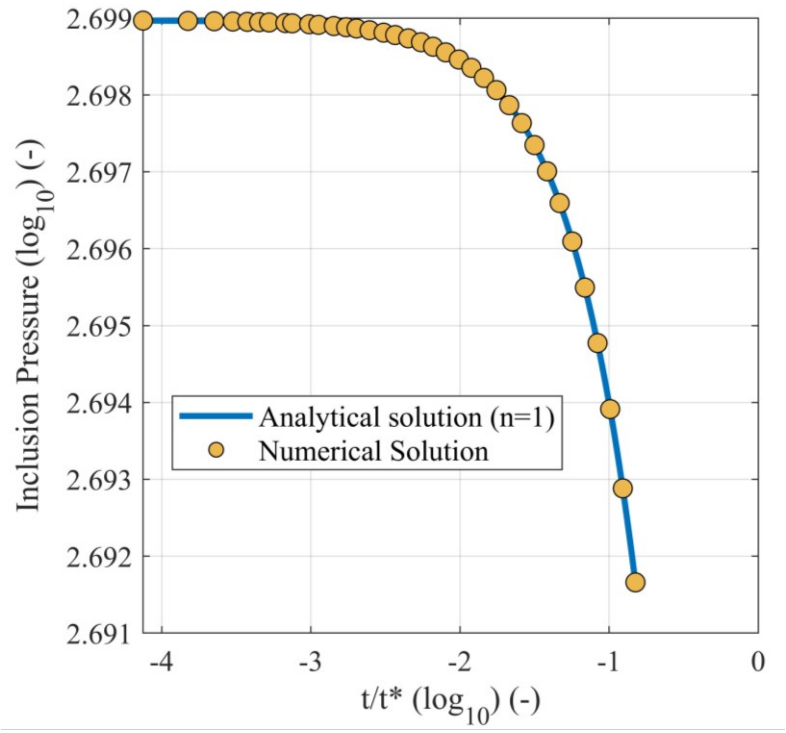

Figure S. 4.3: Comparison between our viscoelastic test case for $n = 1$ and the analytical solution of Dabrowski et al. (2015). The x axis corresponds to time normalized by the characteristic timescale (see Dabrowski et al., 2015) and the y axis shows the inclusion pressure. The solutions are expressed in nondimensional units.

We subsequently considered cases in which the non-Newtonian flow law exponent is higher than 1 (Dabrowski et al., 2015). Once more, an initial elastic solution was the input for the mechanical model, and we modeled the pressure relaxation from this initial configuration. We chose a large timestep (based on the Maxwell timescale) to be in the viscous deformational regime. The moduli of the host were chosen to be 6 orders of magnitude greater than those of the inclusion to emulate incompressibility. A spatial resolution of 100 was enough to reproduce the analytical solution. The inclusion was set to be 100 times smaller than the host. A numerical tolerance of 10^{-6} was set for the non-linear Picard iterations. A constant far-field velocity boundary condition was assigned to the right side of the domain. The results of the benchmark for $n = 3$ and $n = 5$ are presented in Figure S. 4.4.

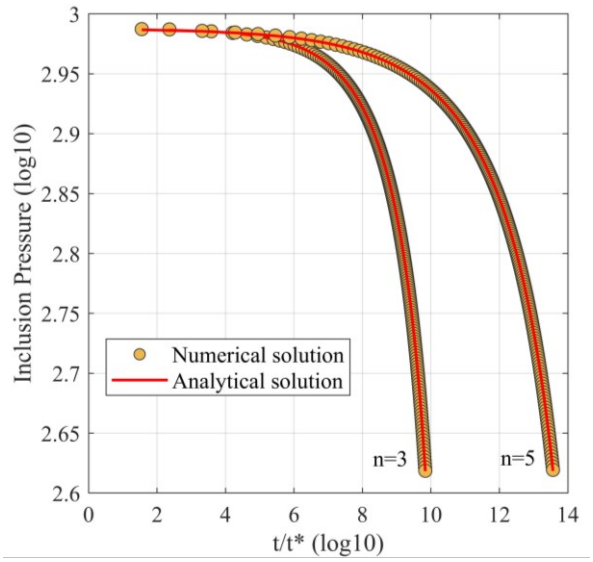

Figure S. 4.4: Comparison between our viscoelastic numerical model and the analytical solution of Dabrowski et al. (2015) for power law exponents equal to 3 and 5. The x axis correspond to time normalized by the characteristic timescale (see Dabrowski et al., 2015) and the y axis shows the inclusion pressure. The solutions are expressed in nondimensional units.

Finally, we considered the analytical solution of Dragoni & Magnanensi (1989). This analytical solution considers three different domains: a spherical inclusion which is surrounded by a Maxwell visco-elastic shell and an elastic outer medium (Figure S. 4.5). The analytical solution aims at simulating the effect of high temperatures on rocks adjacent to a magma chamber. The high temperature of the magma chamber is causing the adjacent rocks to behave in a visco-elastic manner while the outer rock medium is not affected by temperature and remains elastic. In addition, the solution assumes that the magma chamber is internally pressurized. The result of the solution is the evolution of stresses around the magma chamber with time. To simulate this setup, we split the numerical model into three domains. In the first domain, the inclusion is described by a prescribed pressure. We then followed the assumptions of Dragoni & Magnanensi (1989), namely that the elastic outer domain has the same shear modulus as the visco-elastic shell, and that the bulk modulus of the visco-elastic shell is equal to 5/3 times its shear modulus. A spatial resolution of 300 was used. The evolution of this system in time and its comparison to the analytical solution is plotted in Figure S. 4.6.

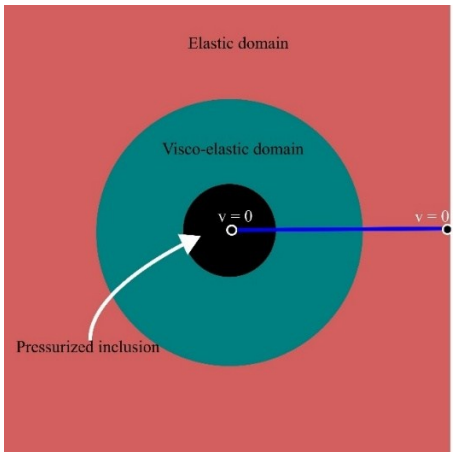

Figure S. 4.5: The model configuration used for the benchmark of Dragoni & Magnanensi (1989). Three different domains are considered: a pressurized inclusion in the middle, surrounded by a visco-elastic medium and an outer purely elastic domain. The blue line shows the one-dimensional modeled profile of this configuration. Zero-velocity Dirichlet boundary conditions are applied.

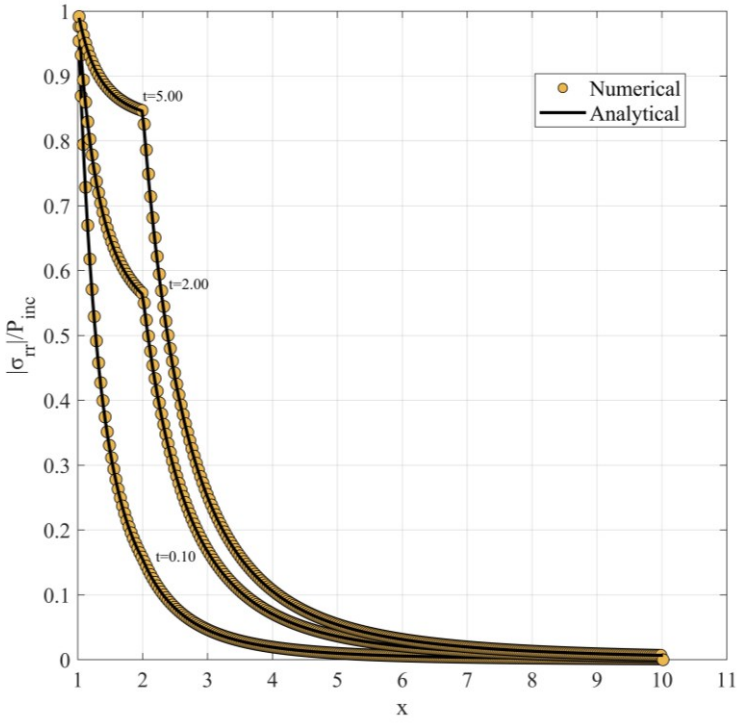

Figure S. 4.6: This figure compares the total normal stress normalized by the inclusion pressure (constant) between our numerical implementation and the analytical solution of Dragoni & Magnanensi (1989). The x axis corresponds to distance. The solutions are expressed in nondimensional units.

4.6.3 Numerical convergence

Here, we assess the effect of grid and timestep resolution on the accuracy of our code. To evaluate the influence of grid resolution, we progressively increased the spatial resolution of the model and tracked the residual pressure of quartz to investigate how the resolution affects the model output. A similar approach was following for the timestep as we progressively increased the simulation timestep to assess the accuracy of the solution.

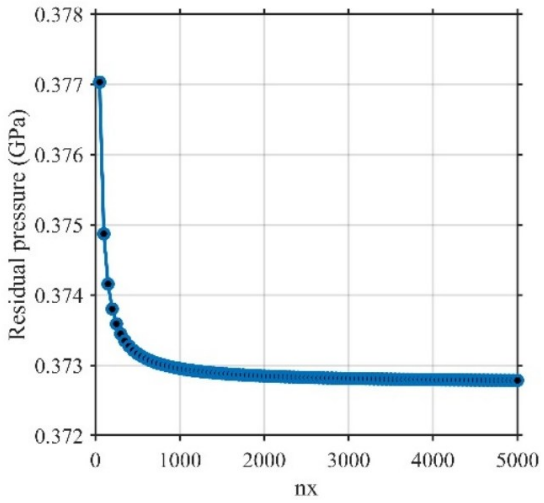

Figure S. 4.7: The effect of grid resolution on the accuracy of our code. Low resolutions impose errors in the order of 0.004 GPa while the increase of spatial resolution leads to the numerical convergence of the solution.

The results of these numerical tests are shown in Figure S. 4.7 Figure S. 4.8. Figure S. 4.7 shows the convergence of the algorithm with increasing spatial resolution. A grid of 50 spatial points produces errors in the order of 0.004 GPa. Figure S. 4.8 shows that increasing the timestep beyond 0.1 Myr dramatically affects the calculated residual pressure of quartz. Timesteps in the order 0.1 Myr and below are producing errors below 0.004 GPa.

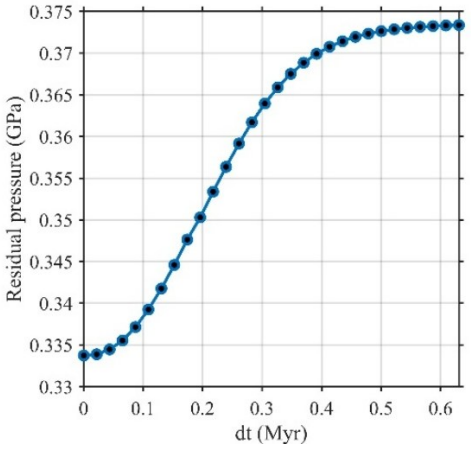

Figure S. 4.8: The effect of timestep on the accuracy of our code. Timesteps below 0.1 Myr impose an error in the order of 0.004 GPa. The error increases drastically for larger timesteps.

4.7 Funding

The authors acknowledge the German Research Foundation (DFG; project number 512790090) for financial support.

4.8 References

Agard, P., Yamato, P., Soret, M., Prigent, C., Guillot, S., Plunder, A., Dubacq, B., Chauvet, A., & Monié, P. (2016). Plate interface rheological switches during subduction infancy: Control on slab penetration and metamorphic sole formation. *Earth and Planetary Science Letters*, *451*, 208–220. https://doi.org/10.1016/j.epsl.2016.06.054

Ambrose, T. K., Waters, D. J., Searle, M. P., Gopon, P., & Forshaw, J. B. (2021). Burial, Accretion, and Exhumation of the Metamorphic Sole of the Oman-UAE Ophiolite. *Tectonics*, *40*(4), e2020TC006392. https://doi.org/10.1029/2020TC006392

Angel, R. J., Mazzucchelli, M. L., Alvaro, M., Nimis, P., & Nestola, F. (2014). Geobarometry from host-inclusion systems: The role of elastic relaxation. *American Mineralogist*, *99*(10), 2146–2149. https://doi.org/10.2138/am-2014-5047

Angel, R. J., Nimis, P., Mazzucchelli, M. L., Alvaro, M., & Nestola, F. (2015). How large are departures from lithostatic pressure? Constraints from host–inclusion elasticity. *Journal of Metamorphic Geology*, *33*(8), 801–813. https://doi.org/10.1111/jmg.12138

Angel, R. J., Murri, M., Mihailova, B., & Alvaro, M. (2019). Stress, strain and Raman shifts. *Zeitschrift Für Kristallographie - Crystalline Materials*, *234*(2), 129–140. https://doi.org/10.1515/zkri-2018-2112

Betancourt, M. (2018). *A Conceptual Introduction to Hamiltonian Monte Carlo* (arXiv:1701.02434). arXiv. https://doi.org/10.48550/arXiv.1701.02434

Bower, A. F. (2010). *Applied mechanics of solids*. CRC Press.

Carosi, R., Cortesogno, L., Gaggero, L., & Marroni, M. (1996). Geological and petrological features of the metamorphic sole from the Mirdita Nappe, northern Albania. *Ofioliti*, *21*, 21–40.

Dabrowski, M., Powell, R., & Podladchikov, Y. (2015). Viscous relaxation of grain-scale pressure variations. *Journal of Metamorphic Geology*, *33*(8), 859–868. https://doi.org/10.1111/jmg.12142

Dewey, J. F., & Casey, J. F. (2013). The sole of an ophiolite: The Ordovician Bay of Islands Complex, Newfoundland. *Journal of the Geological Society*, *170*(5), 715–722. https://doi.org/10.1144/jgs2013-017

Dragoni, M., & Magnanensi, C. (1989). Displacement and stress produced by a pressurized, spherical magma chamber, surrounded by a viscoelastic shell. *Physics of the Earth and Planetary Interiors*, *56*(3–4), 316–328. https://doi.org/10.1016/0031-9201(89)90166-0

Duretz, T., Agard, P., Yamato, P., Ducassou, C., Burov, E. B., & Gerya, T. V. (2016). Thermo-mechanical modeling of the obduction process based on the Oman Ophiolite case. *Gondwana Research*, *32*, 1–10. https://doi.org/10.1016/j.gr.2015.02.002

Enami, M., Nishiyama, T., & Mouri, T. (2007). Laser Raman microspectrometry of metamorphic quartz: A simple method for comparison of metamorphic pressures. *American Mineralogist*, *92*(8–9), 1303–1315. https://doi.org/10.2138/am.2007.2438

Fjelde, T. E., Xu, K., Widmann, D., Tarek, M., Pfiffer, C., Trapp, M., Axen, S. D., Sun, X., Hauru, M., Yong, P., Tebbutt, W., Ghahramani, Z., & Ge, H. (2025). Turing.jl: A general-purpose probabilistic programming language. *ACM Transactions on Probabilistic Machine Learning*. https://doi.org/10.1145/3711897

Garber, J. M., Rioux, M., Smye, A. J., Cruz-Uribe, A. M., Baker, P. L., Vervoort, J. D., Searle, M. P., & Feineman, M. D. (2025). Shear heating during rapid subduction initiation beneath the Samail Ophiolite. *Nature Geoscience*, *18*, 653–660. https://doi.org/10.1038/s41561-025-01711-6

Guilmette, C., Van Hinsbergen, D. J. J., Smit, M. A., Godet, A., Fournier-Roy, F., Butler, J. P., Maffione, M., Li, S., & Hodges, K. (2023). Formation of the Xigaze Metamorphic Sole under Tibetan continental lithosphere reveals generic characteristics of subduction initiation. *Communications Earth & Environment*, *4*(1), 339. https://doi.org/10.1038/s43247-023-01007-w

Hacker, B. R. (1991). The role of deformation in the formation of metamorphic gradients: Ridge subduction beneath the Oman Ophiolite. *Tectonics*, *10*(2), 455–473. https://doi.org/10.1029/90TC02779

Hacker, B. R. (1994). Rapid Emplacement of Young Oceanic Lithosphere: Argon Geochronology of the Oman Ophiolite. *Science*, *265*(5178), 1563–1565. https://doi.org/10.1126/science.265.5178.1563

Hacker, B. R., Mosenfelder, J. L., & Gnos, E. (1996). Rapid emplacement of the Oman ophiolite: Thermal and geochronologic constraints. *Tectonics*, *15*(6), 1230–1247. https://doi.org/10.1029/96TC01973

Hill, R. (1950). *The Mathematical Theory of Plasticity*. (Original work published Oxford University Press)

Ibragimov, I., Kiss, D., & Moulas, E. (2024). A thermo-mechanical model of the thermal evolution and incorporation of metamorphic soles in Tethyan ophiolites: A case study from Oman. *Austrian Journal of Earth Sciences*, *117*(1), 13–24. https://doi.org/10.17738/ajes.2024.0002

Ibragimov, I., & Moulas, E. (2024). Role of continental margin architecture in models of ophiolite emplacement. *Journal of the Geological Society*, *181*(1), jgs2023-063. https://doi.org/10.1144/jgs2023-063

Jamieson, R. A. (1980). Formation of metamorphic aureoles beneath ophiolites—Evidence from the St. Anthony Complex, Newfoundland. *Geology*, *8*(3), 150–154. https://doi.org/10.1130/0091-7613(1980)8%3C150:FORABO%3E2.0.CO;2

Jamieson, R. A. (1986). P-T paths from high temperature shear zones beneath ophiolites. *Journal of Metamorphic Geology*, *4*(1), 3–22. https://doi.org/10.1111/j.1525-1314.1986.tb00335.x

Karato, S., Wang, Z., Liu, B., & Fujino, K. (1995). Plastic deformation of garnets: Systematics and implications for the rheology of the mantle transition zone. *Earth and Planetary Science Letters*, *130*(1–4), 13–30. https://doi.org/10.1016/0012-821X(94)00255-W

Kaus, B.J.P. (2010). Factors that control the angle of shear bands in geodynamic numerical models of brittle deformation. *Tectonophysics*, *484*, 36-47. https://doi.org/10.1016/j.tecto.2009.08.042

Luisier, C., Tajčmanová, L., Yamato, P., & Duretz, T. (2023). Garnet microstructures suggest ultra-fast decompression of ultrahigh-pressure rocks. *Nature Communications*, *14*(1), 6012. https://doi.org/10.1038/s41467-023-41310-w

Moulas, E., Kostopoulos, D., Podladchikov, Y., Chatzitheodoridis, E., Schenker, F. L., Zingerman, K. M., Pomonis, P., & Tajčmanová, L. (2020). Calculating pressure with

elastic geobarometry: A comparison of different elastic solutions with application to a calc-silicate gneiss from the Rhodope Metamorphic Province. *Lithos*, *378–379*, 105803. https://doi.org/10.1016/j.lithos.2020.105803

Moutzouris, D., Moulas, E., Kostopoulos, D., Pomonis, P., Beranoaguirre, A., Chatzitheodoridis, E., & Gerdes, A. (2025). Emplacement of the Pindos ophiolite, NW Greece: P-T-t-kinematic constraints from the metamorphic sole. *Lithos*, *516–517*(108285). https://doi.org/10.1016/j.lithos.2025.108285

Moutzouris, D., Stroh, A., Schorn, S., & Moulas, E. (2026). Hamiltonian Monte Carlo applied to inverse petrological problems. *EarthArXiv*. https://doi.org/10.31223/X58V0H

Neal, R. M. (1996). *Bayesian Learning for Neural Networks*. Springer New York. https://doi.org/10.1007/978-1-4612-0745-0

Neal, R. M. (2011). *MCMC using Hamiltonian dynamics*. https://doi.org/10.1201/b10905

Pummell, B. A., & Thomas, J. B. (2024). Re-equilibration of quartz inclusions in garnet. *European Journal of Mineralogy*, *36*(4), 581–597. https://doi.org/10.5194/ejm-36-581-2024

Rioux, M., Garber, J. M., Searle, M., Crowley, J. L., Stevens, S., Schmitz, M., Kylander-Clark, A., Leal, K., Ambrose, T., & Smye, A. J. (2023). The temporal evolution of subduction initiation in the Samail ophiolite: High-precision U–Pb zircon petrochronology of the metamorphic sole. *Journal of Metamorphic Geology*, *41*(6), 817–847. https://doi.org/10.1111/jmg.12719

Rosenfeld, J. L., & Chase, A. B. (1961). *Pressure and Temperature of crystallization from elastic effects around sold inclusions in minerals? 259*, 519–541.

Searle, M., & Cox, J. (1999). Tectonic setting, origin, and obduction of the Oman ophiolite. *Geological Society of America Bulletin*, *111*(1). https://doi.org/10.1130/0016-7606(1999)111%253C0104:TSOAOO%253E2.3.CO;2

Searle, M. P., & Malpas, J. (1982). Petrochemistry and origin of sub-ophiolitic metamorphic and related rocks in the Oman Mountains. *Journal of the Geological Society*, *139*(3), 235–248. https://doi.org/10.1144/gsjgs.139.3.0235

Van Der Molen, I., & Van Roermund, H. L. M. (1986). The pressure path of solid inclusions in minerals: The retention of coesite inclusions during uplift. *Lithos*, *19*(3–4), 317–324. https://doi.org/10.1016/0024-4937(86)90030-7

Wang, Z., & Ji, S. (1999). Deformation of silicate garnets: Brittle-ductile transition and its geological implications (Pt. 525-541). *The Canadian Mineralogist*, *37*.

Whitney, D. L., Broz, M., & Cook, R. F. (2007). Hardness, toughness, and modulus of some common metamorphic minerals. *American Mineralogist*, *92*(2–3), 281–288. https://doi.org/10.2138/am.2007.2212

Xu, K., Ge, H., Tebbutt, W., Tarek, M., Trapp, M., & Ghahramani, Z. (2020). AdvancedHMC.jl: A robust, modular and efficient implementation of advanced HMC algorithms. *2nd Symposium on Advances in Approximate Bayesian Inference, Proceedings of Machine Learning Research*, *118*, 1–10.

Zhang, Y. (1998). Mechanical and phase equilibria in inclusion–host systems. *Earth and Planetary Science Letters*, *157*(3–4), 209–222. https://doi.org/10.1016/S0012-821X(98)00036-3

Zhong, X., Moulas, E., & Tajčmanová, L. (2018). Tiny timekeepers witnessing high-rate exhumation processes. *Scientific Reports*, *8*(1), 2234. https://doi.org/10.1038/s41598-018-20291-7

Zhong, X., Moulas, E., & Tajčmanová, L. (2020). Post-entrapment modification of residual inclusion pressure and its implications for Raman elastic thermobarometry. *Solid Earth*, *11*(1), 223–240. https://doi.org/10.5194/se-11-223-2020

Zhukov, V. P., & Korsakov, A. V. (2015). Evolution of host-inclusion systems: A visco-elastic model. *Journal of Metamorphic Geology*, *33*(8), 815–828. https://doi.org/10.1111/jmg.12149

Chapter 5: Thesis Conclusions

Over millions of years, rocks undergo continuous chemical and mechanical transformations. Insights into their chemical/mechanical evolution is obtained by investigating thermally-activated processes such as diffusion and viscous relaxation. These thermally-activated processes leave behind "remnants" that can help us understand the deep geodynamic processes that took place during the formation of the metamorphic rocks. This, in turn, enables a more objective interpretation of the present-day observations. An important question rises as to whether we can combine independent chemical and mechanical approaches to understand the evolution of metamorphic rocks. To address this challenge, this thesis presents a multidisciplinary approach to study the evolution of metamorphic rocks from the Pindos metamorphic sole in northwestern Greece. In particular, the study presents the following key findings:

Chapter 2: Petrographic observations combined with Fe-Mg exchange and solvus thermometry as well as phase-equilibria modeling and elastic barometry indicate that the investigated metapelitic rocks from the Pindos metamorphic sole equilibrated under upper amphibolite-facies conditions of approximately 630 ± 20 °C and 1.1 ± 0.2 GPa. Newly obtained $^{40}Ar/^{39}Ar$ geochronological data yield an apparent minimum age of 164.16 ± 0.37 Myr for syn-kinematic muscovite. In contrast hornblende from a metamorphic sole amphibolite provides an age of 165.5 ± 0.73 Myr, with a well-defined plateau, suggesting that this age closely approximates the timing of rock formation. Together, these petrological and geochronological constraints provide robust estimates of the initial equilibration conditions of the rocks and place important bounds on their retrograde evolution, indicating cooling rates ranging from ~60 to ~625 °C/Myr.

Chapter 3: In this chapter an inversion framework is proposed which combines diffusion models with a Hamiltonian Monte Carlo approach. The initial equilibration temperature, cooling rate and effective grain size of muscovite are quantified by reproducing the major-element compositional profiles of garnets but also the apparent $^{40}Ar/^{39}Ar$ cooling age of muscovite. This inversion approach revealed independently that the rocks must have cooled from an initial temperature of 637.6 ± 8.3 °C with an initial cooling rate of 241.3 ± 76.5 °C/Myr. In contrast, the effective grain size of muscovite plays a negligible role in reproducing the observed age of the mineral. The results of this chapter agree in an independent manner with the results of Chapter 2.

Chapter 4: In this chapter an inversion framework was constructed using a viscoelastic thermomechanical forward model in combination with Hamiltonian Monte Carlo that was introduced in Chapter 2. This model aimed at quantifying the initial equilibration temperature and pressure as well as the initial cooling and decompression rates that are able to reproduce the residual pressure of quartz inclusions in garnet. The inversion in Chapter 4 revealed that the rock must have started its retrograde path from an initial pressure of 627.3 ± 20.0 °C and an initial pressure of 1.2 ± 0.03 GPa with an initial cooling rate that must have exceeded 100 °C/Myr. Decompression rate showed insignificant influence on reproducing the observed data.

Based on the results presented above, a major finding of this thesis is the clear and independent agreement between petrological observations, diffusion modeling, and mechanical modeling. It is important to note that the results of one approach do not influence the results of the other approaches, yet all converge on the same conclusions. The high cooling rates recorded across all methods account for the sharp major-element compositional profiles in garnet and the preservation of high equilibration temperatures. They further indicate that the quartz-in-garnet system largely remained within the elastic deformational regime with negligible viscous relaxation. Collectively, these results point to a transient process being responsible for the formation of the metamorphic sole rocks and the subsequent rapid cooling following peak metamorphic conditions. The consistency of our data and inversion results with previous numerical and petrological studies (Duretz et al., 2016; Garber et al., 2025; Ibragimov et al., 2024; Tagliaferri et al., 2025) supports the interpretation that shear heating was the primary factor controlling the formation of the Pindos metamorphic sole.

Appendix : Use of AI tools

AI tool	Used for	Why	When
ChatGPT	Minor grammar corrections	To improve readability	Throughout the entire work
Copilot	Code-writing assistance	To improve plotting and code structure	Chapter 3

Curriculum Vitae

DIMITRIOS MOUTZOURIS

JGU Institute of Geosciences, Mainz, Germany

Email: dmoutzou@uni-mainz.de

Date of birth: 07/06/1998

Nationality: Greek

Education

- 2016-2020: Bachelor's degree, National and Kapodistrian University of Athens. Thesis: *Thermodynamics of serpentinization and carbonation reactions in ultramafic systems*. Supervisor: Dimitrios Kostopoulos
- 2020-2023: Master's degree, National and Kapodistrian University of Athens. Thesis: *The origin of amphibole in ultramafic rocks and a new amphibole-clinopyroxene Fe-Mg exchange thermometer for mantle peridotite lithologies*. Supervisor: Dimitrios Kostopoulos
- 2023-2026: PhD, Johannes Gutenberg University of Mainz. Thesis title: *A combination of petrological and joint chemical-mechanical approaches to unravel deep geodynamic processes*. Supervisor: Evangelos Moulas

Publications

- Moutzouris D., Moulas E., Kostopoulos D., Pomonis P., Beranoaguirre A., Chatzitheodoridis E., Gerdes A., 2025. Emplacement of the Pindos ophiolite, NW Greece: P-T-t-kinematic constraints from the metamorphic sole, Lithos, vol. 516-517, 108285, https://doi.org/10.1016/j.lithos.2025.108285
- Moutzouris D., Stroh A., Schorn S., Moulas E., 2026, Hamiltonian Monte Carlo applied to inverse petrological problems, EarthArXiv, 10.31223/X58V0H

Technical & Computational Skills

- Programming Languages: *Julia* and *MATLAB*
- Software (Geodynamics and Phase equilibria): *PERPLE_X, MAGEMinApp, LaMEM, SUPCRTBL*
- Numerical Modelling: *Finite-differences* and *Finite-Elements* using direct or iterative solvers for solving heat/mass transfer and stress balance.
- Sampling/Inversion methods: *Markov Chain Monte Carlo* and *Hamiltonian Monte Carlo*
- Other: *Machine-learning techniques (e.g., principal component analysis – optimization)*